Novel Nano- and Microfabricated Electromagnetic Probes for Detecting Neural Signals

by

Jax Kuzmiak Phillips

A Dissertation Submitted in Partial Fulfillment of

the Requirements for the Degree of

Doctor of Philosophy

(Biomedical Engineering)

at the

University of Wisconsin–Madison

2024

Date of Final Oral Examination: 1/11/2024
This Dissertation is Approved by the Members of the Final Oral Examination Committee:
Aviad Hai, Assistant Professor, Biomedical Engineering
Walter F. Block, Professor, Biomedical Engineering
Xinyu Zhao, Professor, Neuroscience
Kip Ludwig, Associate Professor, Biomedical Engineering
Filiz Yesilkoy, Assistant Professor, Biomedical Engineering

Dedication

To my friends, loved ones, community, and everyone else

who showed me a world worth living in.

In Memoriam

Frankie Ziyu Wang

2001-2023

Acknowledgements

This dissertation is my distillation of years of collective effort from everyone who's mentored me, collaborated with me, talked to me about my research, learned from me, and kept me sane through the last four and half years. In particular, I would like to thank my advisor, Aviad Hai, for his unwavering support since our first conversation and through thick and thin. Deepest gratitude to my Committee, Drs. Wally Block, Kip Ludwig, Xinyu Zhao, and Filiz Yesilkoy, for taking time out of their winter breaks year after year to lend me their insights into my work. Thank you to all my labmates past and present, especially Ilhan Bok, Suyash Bhatt, Xiaoxuan Ren, TShawn Zhu, Emily Blick, Jamie Sergay, Adam Vareberg, Yash Gokhale, Emily Masterson, Judy George, Jenna Eizadi, Alireza Ashtiani, and Matt Dwyer, who have taught me innumerable lessons, skills, and facts, who have intertwined their work with my own, and who make the lab feel like a family, and especially to my undergraduate mentees, Frankie Wang, Boris Kabistan, Allison McKinney, without whom my projects would have stalled countless times. Heartfelt thanks to the Biocore family, especially Anna Kowalkowski and Seth McGee, and everyone else who made me feel at home in the department. Deep thanks to John Finan, my PI before graduate school, for cultivating my love of research and setting me on this path. Thank you to my mother, father, and stepmother, for all your love and support. And of course, thank you to my partners, friends, and community, and especially the Grab-a-Crabbers, for reminding me of the inherent, joyous meaninglessness of life whenever I need it most.

Abstract

A fundamental goal of neuroscience is to record neural activity from as many cells as possible across the entirety of the brain, without major surgery or wiring through the skull. This has applications in both basic research and clinical practice from diagnostics to neuroprosthesis. However, methods for direct measurement of cellular potential are invasive and generally incompatible with whole-brain scale recording, while less invasive techniques sacrifice spatial or temporal precision and the potential for single-unit recordings. In this dissertation, I present advances in the development of purely passive modalities for hyper-local or single-cell recordings, which allow for broad spatial scope of recording sites, and when applied *in vivo*, will require minimal or no transcranial components during recording. These technologies are designed to interface with modern medical technology such as magnetic resonance imaging (MRI) or magnetoencephalography (MEG). To achieve this, I modelled, fabricated, and applied a new class of coil-based micro- and nano-fabricated probes with no onboard active components that would necessitate onboard power or wireless power transfer. These devices utilize the physical properties of their construction and electrochemical and biological interactions with active neurons to generate readable signals. I describe the modelling, fabrication, and *in vitro* usage of passive, nano-fabricated cellular-scale inductive coils which utilize a neuron's electrical potential to generate a detectable magnetic field which is stronger than the brain's native biogenic magnetism. I then describe the theory, fabrication, and characterization of passive, micro-fabricated inductor-capacitor circuits with a multi-turn planar coil and parallel plate capacitor whose resonant properties depend on the composition of the extracellular solution, where the ionic composition changes during periods of network activity, creating measurable changes in the device's response.

Table of Figures

Contents

Introduction

From diagnostic applications to interfacing the brain with computers and prosthetics, sensing neural activity is a major area of interest, but our ability to do so is constrained by the limitations of current modalities. Methods for directly sensing neural signals are invasive and limited in scope, and broader non-invasive techniques present a trade-off between spatial and temporal precision. Patch clamp is the most direct method for capturing the full transmembrane voltage of a single neuron but is very challenging to implement *in vivo* and involves an open skull window and delicate micromanipulation for each electrode. Multi-electrode arrays (MEAs) offer easier applicability and increasingly broad scope of readouts of extracellular signals, but with limited spatial coverage and adverse effects to the blood-brain barrier and neural tissue [1]. Electrocorticography (ECoG) arrays can record activity with minimal tissue damage and attenuation, and micro-ECoG (μECoG) allows for cellular-scale recording sites for insight into individual neuron activity, but as with all the above methods, these require transcranial wiring to record data that is narrow in spatial scope [2]. Non-invasive techniques are non-injurious but present their own set of limitations on recording. Electroencephalography (EEG) and magnetoencephalography (MEG) measure endogenous, population-derived electrical and magnetic signals, respectively, both of which are attenuated relative to the square of the distance from the source, and therefore arise primarily from the cortex, but EEG signals are further attenuated by the intervening tissues [3,4]. Magnetic resonance imaging (MRI) and specifically functional MRI (fMRI) offer an inherent trade-off between imaging speed and spatial resolution, and commonly do not directly sense neural activity, instead using the blood oxidation level dependent (BOLD) fMRI signal which offers an indirect measure of activity based on oxygen consumption [5,6].

Some next-generation modalities bridge the divide between direct recording and scalability to whole-brain spatial scope. Neural dust avoids the risky electromagnetic (EM) power transmission used for digital communication chips by harvesting and backscattering ultrasound energy sent from a transceiver as a function of signals applied to a field effect transistor (FET). The peripheral nervous system uses explored thus far have avoided the issue of ultrasound attenuation by the skull, but when the devices move into brains, the transceiver will likely sit above the cortex, and may require transcranial wiring [7–10]. Implantable active coil-based transducers (ImpACTs) are MRI-contrast microdevices which incorporate a miniaturized RF antenna to harvest power from an inductively coupled MRI coil. The energy is used to power a FET gated by a sensor, which provides variable resistance in response to a measured signal. This affects the quality factor (Q) of the device, a measure of the specificity of the resonant frequency – the more the FET senses, the lower the Q, and the more detuned the device is [11]. Further advances in this vein have shown that the same principle can be applied with ion-sensitive field-effect transistors (ISFETs) [12]. These devices, as described, contain an active component and are on the scale of several millimeters, but offer potential for miniaturization toward passive cell-sized devices, provided Q can be effectively modulated at smaller scales.

I first present a cellular-scale coil-based device capable of transducing cellular potentials to magnetic fields readable from outside of skull using currently available technology. These “nanocoils” consist of an 80-micron nanofabricated planar inductor with a minimum feature size of 500-1000 nm with features at its center designed to promote tight electrical coupling of single neurons to the coil. The outside of the coil terminates in a solution-facing ground pad with no adhesion features. The device is compact enough that the sensor pad and ground pad experience the same local field potential, such that the main factor responsible for a potential difference is the

attached cell. The proposed nanoscale attachment features are based on gold mushroom-shaped microelectrodes (GMμEs), which are functionalized with an engulfment-promoting peptide (EPP) and encourage cells to form synapse-like connections with the electrode for a seal resistance on the order of 100MΩ and a junctional membrane resistance of 10-100MΩ (Hai *et al.*, 2010). This device is capable of transducing a single action potential into a magnetic field capable of being detected from outside the skull using currently available technologies such as magnetic source MRI (msMRI) or MEG.

I then present a purely passive micro-scale resonator for monitoring the activity of small populations of neurons. The "microresonator" consists of a 1 millimeter microfabricated gold planar inductor coil with a planar parallel plate capacitor. This forms an inductor-capacitor resonator which is partially shorted by the extracellular solution. As the device resonates with an RF antenna such as the one used in an MRI, the interface between the device and the aqueous solution forms an electrical double layer, in which positively and negatively charged ions at the surface form a capacitive electrical interface. The solution itself partially shorts the device, modulating the quality factor (Q), which determines the strength of resonance. The extracellular concentration of potassium ($[K^+]_e$) can rise as much as 5 mM immediately around neurons, persisting for no more than 10 seconds [13–15]. The equilibrium extracellular ionic concentrations also reveal information about the overall brain state. $[K^+]_e$ rises and $[Mg^{2+}]_e$, $[Ca^{2+}]_e$, $[H^+]_e$, and extracellular volume fall during wakeful states, and vice versa during sleep or sedation [16]. The fast changes in ionic concentration around the microresonator cause changes in its resonant response, allowing for a purely passive, resonance-based metric for local neural activity with future *in vivo* and clinical applications.

Chapter 1: Enhanced magnetic transduction of neuronal activity by nanofabricated inductors quantified via finite element analysis

Jack Phillips, Mitchell Glodowski, Yash Gokhale, Matt Dwyer, Alireza Ashtiani, Aviad Hai

J Neural Eng. 2022 Jul 1;19(4):10.1088/1741-2552/ac7907. doi: 10.1088/1741-2552/ac7907.

Abstract

Objective. Methods for the detection of neural signals involve a compromise between invasiveness, spatiotemporal resolution, and the number of neurons or brain regions recorded. Electrode-based probes provide excellent response but usually require transcranial wiring and capture activity from limited neuronal populations. Noninvasive methods such as electroencephalography (EEG) and magnetoencephalography (MEG) offer fast readouts of field potentials or biomagnetic signals, respectively, but have spatial constraints that prohibit recording from single neurons. A cell-sized device that enhances neurogenic magnetic fields can be used as an *in situ* sensor for magnetic-based modalities and increase the ability to detect diverse signals across multiple brain regions. *Approach.* We designed and modelled a device capable of forming a tight electromagnetic junction with single neurons, thereby transducing changes in cellular potential to magnetic field perturbations by driving current through a nanofabricated inductor element. *Main results.* We present detailed quantification of the device performance using realistic finite element simulations with signals and geometries acquired from patch-clamped neurons *in vitro* and demonstrate the capability of the device to produce magnetic signals readable via existing modalities. We compare the magnetic output of the device to intrinsic neuronal magnetic fields

and show that the transduced magnetic field intensity from a single neuron is more than three-fold higher at its peak (1.62 nT vs 0.51 nT). Importantly, we report on a large spatial enhancement of the transduced magnetic field output within a typical voxel (40 x 40 x 10 microns) over 250 times higher than the intrinsic neuronal magnetic field strength (0.64 nT vs 2.5 pT). We use this framework to perform optimizations of device performance based on nanofabrication constraints and material choices. *Significance.* Our quantifications institute a foundation for synthesizing and applying electromagnetic sensors for detecting brain activity and can serve as a general method for quantifying recording devices at the single cell level.

Introduction

From basic neuroscience to neurology, the ability to decode neural activity with minimized invasiveness and little compromise to spatiotemporal precision has long been the goal of experimenters and clinicians[17–19]. Implantable electrodes are the most typical brain interface allowing for single-neuron electrophysiological readouts, but they are invasive, requiring long-term transcranial connections with readouts limited by the size of the device[20,21]. Techniques such as electroencephalography (EEG) and magnetoencephalography (MEG) offer an entirely noninvasive alternative, enabling remote recording of electrophysiological signals at the scalp, but do not provide readouts at single-neuron resolution[22,23]. Due to amplitude attenuation and spatial distortion of local field potentials (LFPs) through neural tissue and the skull, EEG provides a measure of LFPs originating from large aggregates of neurons within the cortex, with spatially shifted readouts and signal amplitude attenuation proportional to the square of the distance from its source[22,24]. In contrast, magnetic fields in the brain are only minutely attenuated or distorted, and can therefore be detected with higher spatial precision and improved localization using sensitive magnetometers[23,25]. MEG readouts still arise from large populations of neurons firing

synchronously, and likely reflect activity developing from neural currents within shallow areas of cortical sulci that are properly aligned to the magnetic detection devices[23]. Bridging the gap between noninvasive neuroimaging and single-neuron invasive electrophysiology can potentially open the door to a new milieu of brain readouts.

Quantifications of intrinsic neuronal magnetic fields (NMFs) arising from the excitation of single neurons, subcellular compartments, and multicellular neuronal populations, were carried out computationally by several groups and can determine possibilities for NMF detection without the need for invasive transcranial wiring at the time of recording [26–29]. These studies informed the interpretation of MEG recordings[23,30] and catalyzed the design of specialized pulse sequences, phantom measurements and distilled preparations for magnetic resonance imaging (MRI) in attempts to detect NMFs volumetrically[31–35]. To date, real-time detection of NMFs by MEG at native *in vivo* scenarios, in the presence of motion artifacts, and blood flow related electromagnetic disturbances[23,36,37] requires severe averaging of consecutive trials evoking coordinated activity of many neurons, and has not yet been demonstrated convincingly by volumetric modalities[6,31]. This points to a requirement for *in situ* agents similar to emerging contrast agents for direct neuroimaging of calcium[38–40] and neurotransmitters[41–44], that could similarly facilitate direct detection of NMFs across the brain.

Here, we present an approach for enhancing magnetic fields in response to intrinsic electrophysiological events using nanofabricated planar inductors that are interfaced with single neurons and designed to act as agents that transduce neural activity into readable magnetic signals. The interface relies on high electromagnetic coupling promoted by nanofabricated protrusions previously shown to generate a tight cleft between cells and electrodes[45,46] and to yield increased electrical response to neural activity[47–49]. Using a realistic finite element framework

with nanometer scale resolution, we quantify the ionic fluctuations induced in the neuron coupled to the device by using patch clamp recordings of mammalian cortical neurons as signal input. We quantify the voltage drop developing between the interface pad at the center of the inductor and an extended reference pad facing the extracellular solution, and then determine the amplitude and spatiotemporal characteristics of the magnetic field response resulting from membrane potential changes that drive current through the device. We use our results to perform optimizations of the geometry of the device while conforming to nanofabrication constraints and reach an optimized design that is able to transduce electrophysiological signals to a magnetic field approximately 300 times greater in magnitude perpendicular to the plane of the inductor and cell culture surface than those produced intrinsically by individual neurons when averaged across a volume. Our approach could immediately enable sensitive detection of single-neuron activity *in vitro* and pave the way for potential future designs applied with modalities such as MEG and MRI.

Methods

Device fabrication

Devices were fabricated by electron beam lithography on glass or high resistivity silicon dies. A2/A4/A6 Poly methyl-methacrylate (PMMA) 495 (Kayaku Advanced Materials Inc, MA, USA) was spin-coated on samples at 3000 RPM for 30 seconds and baked in a convection oven for 30 min. Direct write of inductor patterns was then performed by electron beam lithography (Elionix, Tokyo, Japan) followed by development of the resist using MIBK/IPA (1:2). Ti/Au (1:10) was deposited by electron beam deposition followed by PMMA lift off in ultrasonicated acetone (5 minutes) at room temperature. Silicon Oxide insulating layer was deposited by plasma-enhanced chemical vapor deposition. An additional nanolithography step was performed to define the ground pad and protruding pillars at the interface pad, followed by buffered oxide etching through the

silicon oxide layer. Au protrusions were grown by electron beam deposition PMMA was lift off. Samples were then cleaned in IPA and cultured with neurons as described below to demonstrate biocompatibility (Fig. 1.1B). The device optimization described below uses a device geometry successfully fabricated in this way as a starting point.

***In vitro* cell culture**

Primary cortical neurons were cultured on substrates following previously described protocols[50]. Glass or device surface was sterilized for 15 minutes in ethanol, then a portion of each sample was prepared with a 50 µL droplet of sterile filtered aqueous 0.1 mg/mL poly-d-lysine (PDL, Gibco A38904-01) and 4 ug/mL laminin (Gibco 23017-015). Coverslips sat for 60 minutes in incubator conditions (37°C, 5% CO_2, 95% humidity), were rinsed three times with PBS, then stored at 4°C overnight. Primary cortical rat neurons (Gibco A10840-01, Lot 2111507) were thawed from dry ice (-80°C) for two minutes without agitation in a 37°C water bath. A 15 mL conical tube and 1 mL micropipette tip were rinsed with plating media (Neurobasal Plus, Gibco A3582901; 10% FBS Gibco 10437010; 1x GlutaMAX, Gibco 35050-061), the tip was used to transfer the cell suspension from the cryotube to the conical tube, 1 mL of plating media was added dropwise for a final concentration of 500,000 cells/mL, and 300 µL of cell suspension (150,000 cells) were plated onto each sample. The cultures sat in incubator conditions for 4 hours before plating media was removed and 3 mL maintenance media (Neurobasal Plus, 1x B27 Plus Gibco A3582801, 1x GlutaMAX) were added to each 35 mm well. 1.5 mL media changes were performed every 3-4 days (Mondays and Fridays). Cells on devices were stained with 10 µg/mL Calcein AM (Invitrogen C3099) in media for 20 minutes at 37°C followed by a 20-minute rest in stain-free media at 37°C before imaging for visualization (Fig. 1.1B).

Patch Clamp Recordings

At 24 days *in vitro* (DIV) samples on glass coverslips were removed from maintenance media and placed in extracellular solution (ECS; in mM, NaCl 145, KCl 5, $MgCl_2$ 1, $CaCl_2$ 1, HEPES 5, Glucose 5, Sucrose 20, D-serine 0.01, adjusted to pH7.4 with NaOH and 315 mOsm with sucrose). All solutions were prepared with culture grade H_2O (Corning 25-055-CVC). Filamented glass pipettes (8250 Glass, A-M Systems 596800 were pulled on a P-97 pipette puller (Sutter Instruments, Novato, CA) to create 5-10 MΩ micropipettes. Pipettes were backfilled with intracellular solution (ICS; in mM, KCl 120, HEPES 10, ATP.Na 5, GTP.Na 0.2, EGTA 10, adjusted to pH 7.2 with KOH), mounted on a Sutter IPA Headstage with a Ag/AgCl coated wire driven by a Sutter Quad micromanipulator and connected to a Sutter Double IPA patch clamp amplifier for recording via SutterPatch (v. 2.04, Sutter Instruments, Novato, CA) within Igor Pro software (v. 8.04, WaveMetrics, Portland, OR) in current clamp configuration. For staining experiments, ICS included 20 μM of biocytin (Sigma B4261). Upon breaking through the plasma membrane, biocytin diffused into the cell, allowing imaging of the neuron processes for morphological registration used for simulations (Fig. 1.1A). Electrophysiology experiments were performed using Olympus BX51WIF microscope (Olympus America Inc., Waltham, MA) and ORCA-Flash4.0 V3 C13440 Digital sCMOS camera (Hamamatsu, Japan) for optical acquisition during biocytin injection.

Model neuron

Biocytin-injected neuron morphology (Fig. 1.1A) was traced to create a vector representation, which was imported into COMSOL multiphysics simulation environment (COMSOL Inc., Stockholm, Sweden). Geometry was extruded to a height of 1.1 μm (Fig. 1.1C). The membrane was modeled with exterior surface area 1450 μm^2, volume 14.39 μm^3, relative permeability ε=1,

relative permittivity μ=1, electrical conductivity σ=1e-13 S/m, surrounding the intracellular environment, surface area 1431.1 μm^2, volume 463.77 μm^3, which was modeled using the electrical properties of cerebrospinal fluid, ε = 1.09e2, μ = 1, σ = 2 S/m. Representative action potential data was extracted from voltage traces of current clamp recordings (Fig. 1.3A, sampling frequency = 6103.5 Hz, total recording time 23:51.768) and used as input for an electronic circuit simulation software (LTSPICE, Analog Devices, Norwood, MA). The cell-device interface was simulated as a 100 MΩ resistor in parallel with a 15 pF capacitor. The current was measured across this interface and downsampled to 20 key values, which were applied as inputs in COMSOL on one face of the neuron in a parametric sweep stationary study for simulations of magnetic flux density and field strength during action potentials to compare the response of the naïve model neuron to that of the modelled cell-device interface (Fig. 1.3C).

Device modelling and optimization

Simulations and optimizations of device response and device-neuron interface were performed in COMSOL. Patterns used for nanofabrication were imported and extruded along the z-axis. The electrical properties of the device were set to those of gold, ε = 1, μ = 1, σ = 1e6 S/m. This gold layer thickness was tested at 100, 500, 1000, and 1500 nm. Lateral width of the inductor conducting turns was tested at 540, 730, 940, and 1020 nm using a constant center-to-center turn distance of 1478 nm. Given a constant outer diameter (75 μm edge-to-edge, 80 μm corner-to-corner), turn width (1.0 μm edge-to-edge, 1.1 μm corner-to-corner), and turn spacing (0.46 μm edge-to-edge, 0.50 μm corner-to-corner), the number of turns was varied and represented as the percentage of the total diameter left open at its core. The open core percentage was tested at 10.9% (23 turns), 22.6% (20 turns), 34.4% (17 turns), 46.2% (14 turns), 57.9% (11 turns), and 65.8% (9 turns). All device geometries were tested using representative current input of 1 nA through the interface pad

at the center of the inductor. The optimized device geometry was used to model the magnetic response when coupled with the model neuron. The effects of various substrates were tested using the same input current by varying the material properties of a 25 x 50 x 100 μm block beneath the device between glass, ε=4.7, μ=1, σ=2.3e-21 S/m; polyimide, ε=3.8[51], μ=1, σ=6.7e-18 S/m; parylene, ε=3.1[51], μ=1, σ=1.136e-15 S/m; and silicon of various conductivities, ε=11.68, μ=1, σ=(0.01, 0.1, 1, 10, 100, 1000, 10,000, 100,000) S/m (0.001 Ω·cm to 10,000 Ω·cm). Magnetic field values were extracted from the model either linearly across a 120 μm x 1 μm x 1 μm region of interest (ROI) centered at various Y coordinates on the Z=0 plane, or volumetrically within a 40 μm x 40 μm x 10 μm ROI centered at the cell-device interface pad, in the X, Y, and Z axes. For linear scans, the mean and standard deviation of the absolute magnetic field magnitude were taken along the Y/Z axes within the ROI. Separately, absolute magnetic field amplitude was taken along a 20 μm, Y-aligned line on the Z = 0 plane, centered on the neurite 2 μm away from the input port (Supplementary Fig. S1.1) to compare the magnetic field amplitude of the neuron with and without the presence of the device. Volumetric values averaged the Z component of the magnetic field across the ROI. For optimizations of device geometry and substrate testing, the Z component of the magnetic field output was extracted at an XZ slice of the model arena at the Y coordinate corresponding to the center of the coil and used to compare the output of each model instance.

Results

Enhancement of intrinsic neuronal magnetic fields by nanofabricated coils

In order to explore the feasibility of enhancing intrinsic neuronal magnetic fields (NMFs) by nanofabricated coils (nanocoils) interfaced with single neurons, we generated a realistic finite element model of a cell coupled to device and quantified the magnetic field response to current

injected into the cell (Fig. 1.1). The model uses morphology extracted from primary cortical neurons injected with fluorescently labeled biocytin via patch micropipette electrodes (Fig. 1.1A and supplementary Fig. S1.2). Neurons grew on glass coverslips or nanofabricated devices for up to 24 DIV (Fig. 1.1B). We input a series of key current values into the model, extracted and calculated from a patch clamp recording of cells on coverslips (Fig. 1.3C), with a peak of 1.7 nA intracellular current in the model cell (Fig. 1.1C), resulting in intracellular electric fields of up to 1.2 mV/μm and extracellular electric fields up to 30 μV/mm within 2 μm of the neurite membrane (Supplementary Fig. S1.2C), and the transmembrane electric field gradient reaching 11 mV/nm as previously seen both *in vitro* and *in vivo*[52]. The absolute amplitude of the magnetic field observed near the neuron in response to current injection reached values of up to 0.51 nT and decays to <1% of peak signal within an average of 30 μm of the neuron, similarly to previous models of single-cell NMFs[27,28]. We next quantified the magnetic field amplitude at a volume surrounding the same 1.7 nA current-injected neuron coupled to a nanocoil (Fig. 1.1D). The neuronal membrane was coupled to the interface pad in the middle of the nanocoil (Fig. 1.1D, a). The magnetic field amplitude at various line scans across the X axis (Fig 1.1D, a-e) reached values of up to 1.6 nT and decayed to <1% of peak within an average of 19 μm from the outer turns of the nanocoil. In the case of line a (Fig 1.1D), which crosses the interface pad, the magnetic field decayed to <1% of peak an average of 46 μm from the interface pad. We quantified the spatial distribution of NMFs in the naïve neuron not coupled to the device within a 1 μm by 1 μm cross sectional area around various line scans across the X axis and found that across three representative somatic and neurite compartments (Fig. 1.1C, a-c, Fig. 1.1E) the full widths at half maximum (FWHM) of magnetic field magnitude were (a) 2.7 μm, (b, soma) 7.9 μm, and (c) 7.1 μm. In contrast, the spatial distribution of magnetic fields near a neuron coupled to a device across five

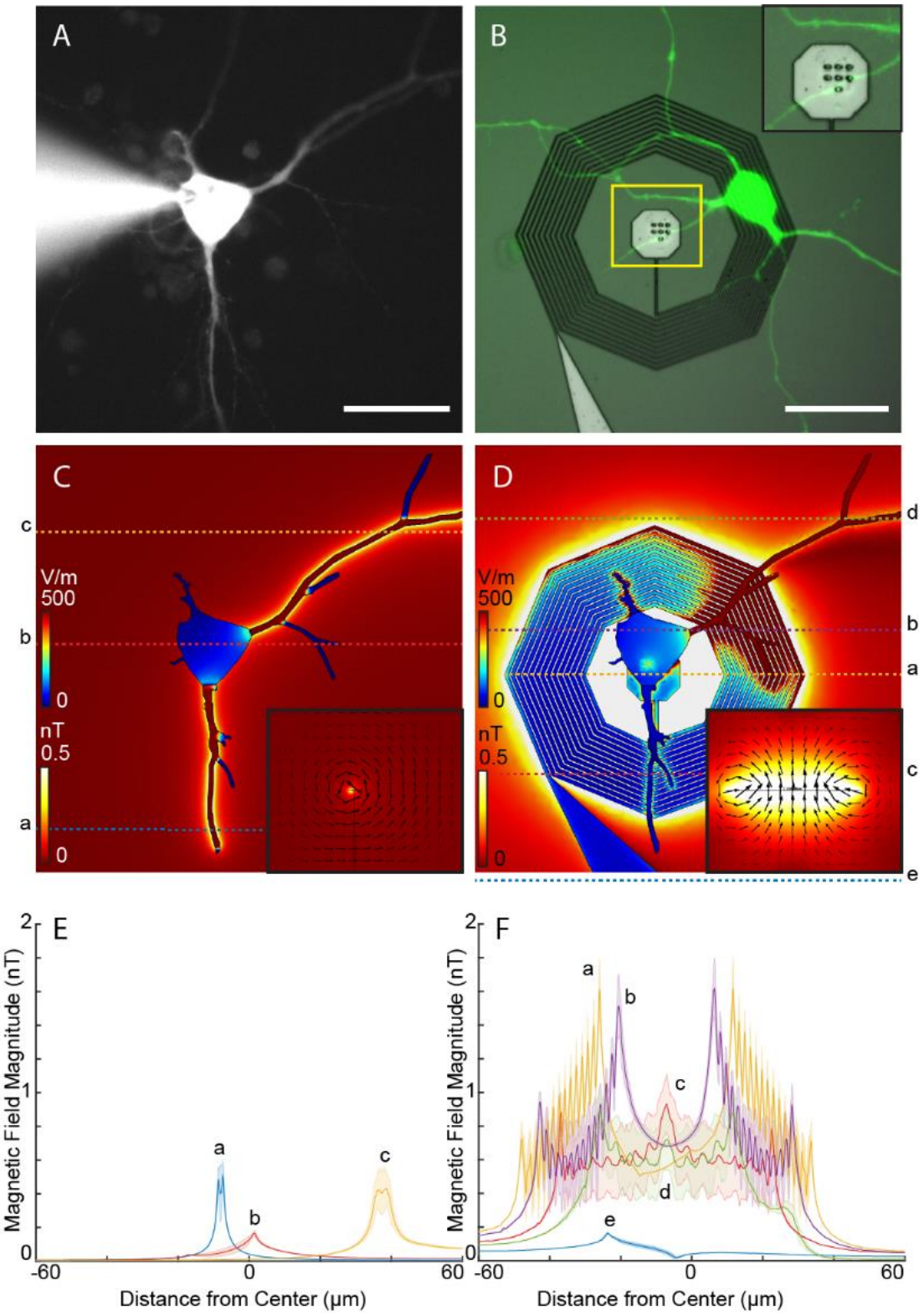

Figure 1.1: Model of single-neuron magnetic fields enhanced by nanofabricated coils. (A) A patch clamped primary cortical rat neuron microinjected with fluorescently labeled biocytin, traced digitally for use in the model. Scale bar: 30 μm. (B) Neuron growing on top of a nanofabricated

coil (green: calcein AM, grayscale: differential interference contrast). Scale bar: 30 μm. Inset: a neurite interfaced with a mushroom-shaped cell-adhesion protrusion nanofabricated at the interface pad at the center of the coil. (Scale bar: 30 μm). (C-D) top (XY) views of the model of the naïve (C) and nanocoil-enhanced (D) neuron. Surface color plot, electrical field strength. Slice color plot, magnetic field strength. Inset arrow plot, magnetic flux. Dashed colored lines correspond to (E-F), magnetic field magnitude (nT) across the X dimension. Colored bands: corresponding standard deviation.

representative regions (Fig. 1.1D, a-e, Fig. 1.1F) was spatially enhanced with FWHM of (a) 67 µm, (b) 72 µm, (c) 62 µm, (d) 46 µm, and (e, ground pad) 16 µm. The magnetic field amplitude of the neuron itself was not significantly changed when coupled to the device, reaching levels of up to 0.60 nT in the neurite of the naïve neuron and 0.25 nT in the neurite of the neuron enhanced by the device, measured 2 µm from the neurite input port (Supplementary Fig. S1.1), within the bounds of minimal magnetic interference. In summary, the magnetic field amplitude output by the device driven by cellular potentials is more than three times greater at its peak (1.6 nT vs 0.51 nT) across a 10 times wider lateral distance (72 µm from the device vs 7.1 µm from the neurite) than the intrinsic NMF. Looking at a 40x40x10 um voxel, discussed below, this results in a 250-fold spatial enhancement (640 pT vs 2.5 pT, see Fig. 1.3).

Analysis of device geometry

Based on the initial geometry used to quantify the magnetic response of a neuron-device interface, we performed optimizations of design features to explore maximal transduction while obeying nanofabrication limitations (Fig. 1.2). Three main parameters tested included the vertical thickness of the device metallization layer (Fig. 1.2A-C), the lateral width of the nanocoil turns (Fig. 1.2D-F), and the number of turns as represented by the open core percentage (Fig. 1.2G-I). For each parameter value, we compared the mean z-axis component of the magnetic flux density (B_z) within a region of interest (ROI) across a XZ slice over the center of the device, spanning 50 µm along the x axis, and 12.5 µm along the z axis. The bottom of the slice was aligned to z = 0, coplanar with the bottom plane of the device (Fig. 1.2, A-B, D-E, G-H, bottom panel).

We used the initial geometry (turn width of 334 nm, core 57.9%) and varied the vertical gold layer thickness by extruding the device to values of 100, 500, 1000, and 1500 nm (Fig. 1.2A-C), yielding average field strength B_z = 0.030 ± 0.013 nT, 0.086 ± 0.033 nT, 0.12 ± 0.04 nT, and 0.13 ± 0.05

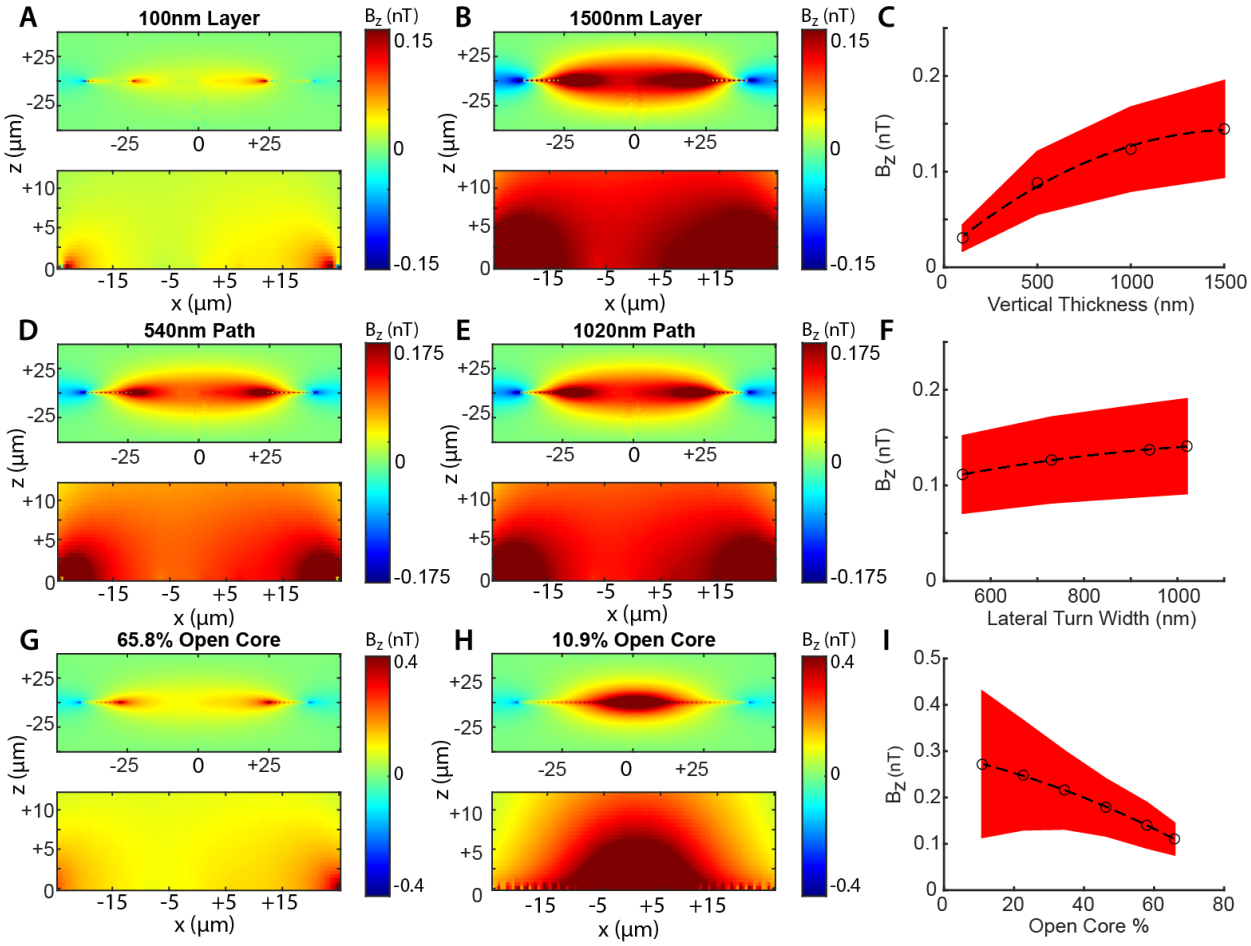

Figure 1.2: Optimizations of device geometry. Magnetic transduction was optimized based on design parameters including the thickness of the device metallization layer (A-C), turn width (D-F), and the ratio between the inner and outer diameters of the nanocoil (G-I). (A,B; D,E; G,H) XZ section views of magnetic flux density in Z for models on the extremes of each optimization. Top, full view of model geometry. Bottom, zoomed view of the region of interest (ROI) used to calculate induced field strength. (C,F,I) scatter plots of each pixel in ROI views. Large circle, mean. Red band: standard deviation. Black dashed line: polynomial fit of means.

nT, respectively. Proceeding with a 500 nm thick gold layer, we next quantified the effect of nanocoil turn width on the average magnetic field strength B_z at the device surface (Fig. 1.2D-F). Turn width was set to 540, 730, 940, and 1020 nm, yielding average field strength B_z = 0.11 ± 0.04, 0.13 ± 0.04, 0.14 ± 0.04 and 0.14 ± 0.05 nT, respectively (Fig. 1.2F). Predictably, the widest path induced the strongest magnetic field strength. We turned to testing the effect of the total number of turns, while maintaining a constant outer diameter (80 µm), neural interface pad diameter (when allowed by the core size, 14 µm), coil thickness (500 nm), turn width (1020 nm), and turn spacing (1478 nm) (Fig. 1.2G-I). We represent this as the ratio of the inner to the outer diameter, or the percentage of the outer diameter that makes up the open core of the nanocoil. We tested values 10.9% (23 turns), 22.6% (20 turns), 34.4% (17 turns), 46.2% (14 turns), 57.9% (11 turns), and 65.8% (9 turns), which yielded mean B_z = 0.27 ± 0.16, 0.25 ± 0.12, 0.22 ± 0.08, 0.18 ± 0.06, 0.14 ± 0.04 and 0.11 ± 0.03 nT, respectively (Fig. 1.2I). Predictably, smaller cores produced higher peak magnetic field strength perpendicular to the plane of the coil (peak B_z = 1.1, 0.85, 0.79, 0.73, 0.67 and 0.52) while the minimum field strength observed at the periphery of the region of interest remained stable across different conditions (min B_z = 0.057, 0.058, 0.061, 0.064, 0.060, and 0.061 nT).

Single neuron activity on optimized device

We analyzed the magnetic field developing at the neuron-device interface during a typical action potential (AP) selected from a series of spontaneously occurring spikes recorded via patch clamp (Fig. 1.3A). Modeled magnetic field was averaged across a 40 x 40 x 10 µm voxel extending 20 µm to each side of the center of the coil, and 5 µm above and below the coil (Fig. 1.3B). The same voxel dimensions were used to average the modeled magnetic output of the naïve neuron. Absolute AP amplitude was 72 mV, and the after-hyperpolarization voltage was -8.2 mV (Fig. 1.3C). The

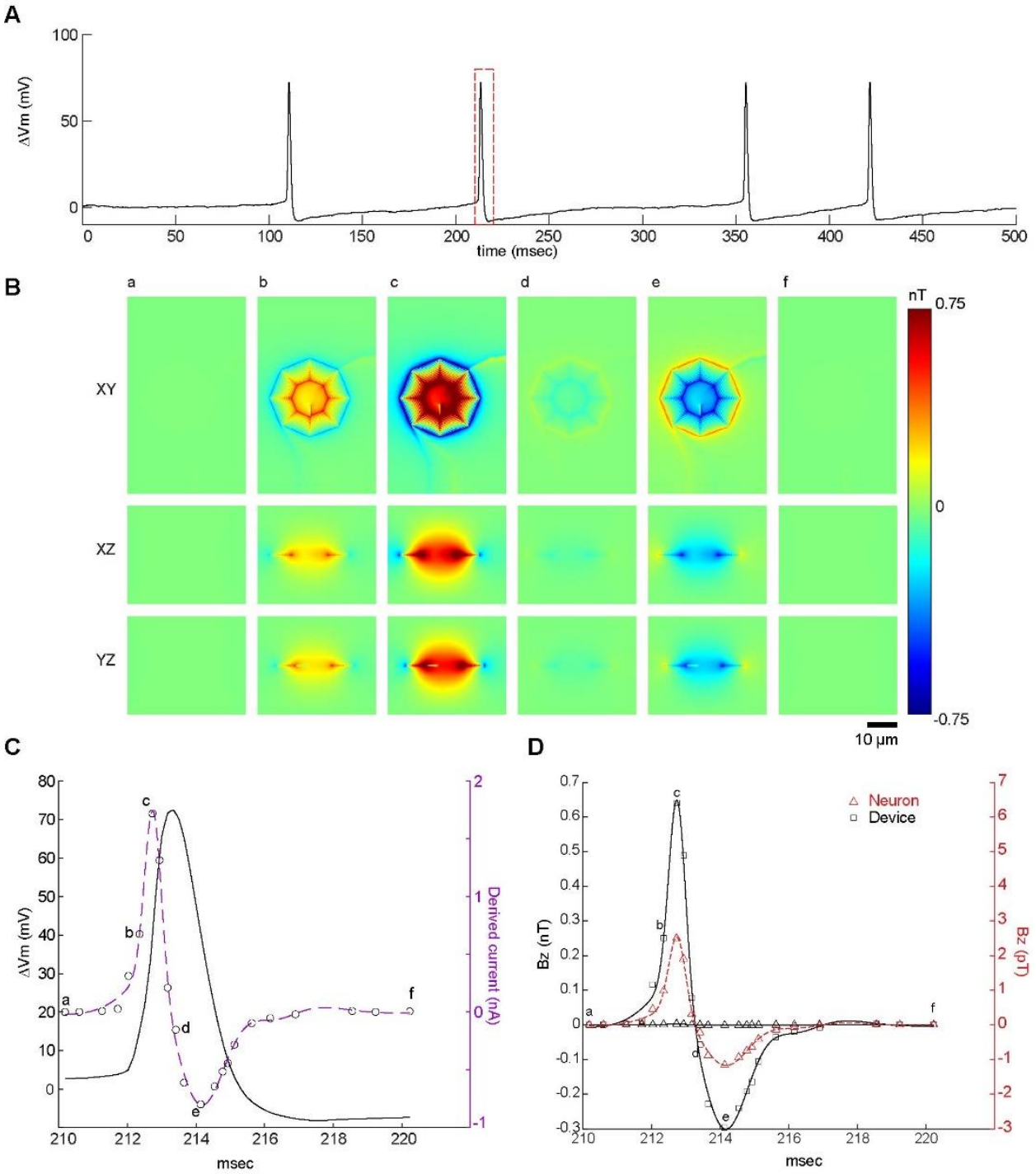

Figure 1.3: Modelling the response to a recorded action potential. (A) 500 msec trace of a spike train recorded via patch clamp of primary cortical neuron. Window used in model is highlighted by dashed box. (B) Axes planes illustrating the magnetic field induced in the coil at 6 points (a-f) along the action potential, corresponding to marked points on C and D. (C) Comparison

of voltage and current traces of action potential. Left axis, solid black line: change in membrane potential from resting potential (mV). Right axis, data points: 20 current values calculated from voltage trace. Purple dashed line, gaussian fit of current data (nA). (D) Comparison of magnetic field between device-enhanced and naïve neurons (square and triangle markers, respectively). Left axis, solid black lines: Gaussian fit of magnetic field strength in nT. Right axis, dashed red line: Gaussian fit of magnetic field strength in pT, to highlight the scale of the naïve neuron's response.

AP voltage trace was run through the equivalent circuit of a neuron to derive the current trace (Fig. 1.3C, purple). The current peaked at 1.7 nA during depolarization and had a minimum of -0.80 nA during the after-hyperpolarization stage. The magnetic field perpendicular to the plane of the neuron and nanocoil peaked at 2.5 pT for the naïve neuron, and at 640 pT for the neuron enhanced by the device. The magnetic field perpendicular to the plane of the geometry induced by the downswing current was -1.2 pT for the naïve neuron and -300 pT for the enhanced neuron. The overall spatial enhancement of the transduced magnetic field output within a voxel was 250-fold higher than the intrinsic neuronal magnetic field.

Substrate testing

To evaluate performance on substrates compatible with nanolithography that are commonly used for implantable devices, we quantified the magnetic transduction of nanocoils embedded on dielectric substrates including glass, parylene and polyimide, and on silicon with various levels of doping (Fig. 1.4). High resistivity silicon (1,000 $\Omega \cdot$ cm and 10,000 $\Omega \cdot$ cm) and all dielectric substrates displayed strong induced magnetic fields (Fig. 1.4A) with average magnetic field strength of 0.23 nT ± 0.08 nT for dielectrics, 0.22 ± 0.07 nT for 10,000 $\Omega \cdot$ cm Si, and 0.22 ± 0.07 nT for 1,000 $\Omega \cdot$ cm Si. Low resistivity silicon (0.001, 0.01, and 0.1 $\Omega \cdot$ cm) demonstrated predictable current shunting, and weak induced magnetic fields, with average field strength of $4.8 \cdot 10^{-6} \pm 3.8 \cdot 10^{-4}$ nT, $8.5 \cdot 10^{-5} \pm 2.1 \cdot 10^{-4}$ nT, and $9.7 \cdot 10^{-4} \pm 7.1 \cdot 10^{-4}$ nT, respectively). Silicon substrates with resistivities of 1, 10, and 100 showed an intermediate effect, with average field strength of 0.0080 ± 0.0048, 0.052 ± 0.022, and 0.16 ± 0.06 nT, respectively). Current density was largely in proportion to field strength, reaching maximal levels of 880 A/m^2, 2400 A/m^2, 2800 A/m^2, and 2800 A/m^2 for 1, 100, 1000 $\Omega \cdot$ cm Silicon and for Polyimide, respectively (Fig. 1.4B-E).

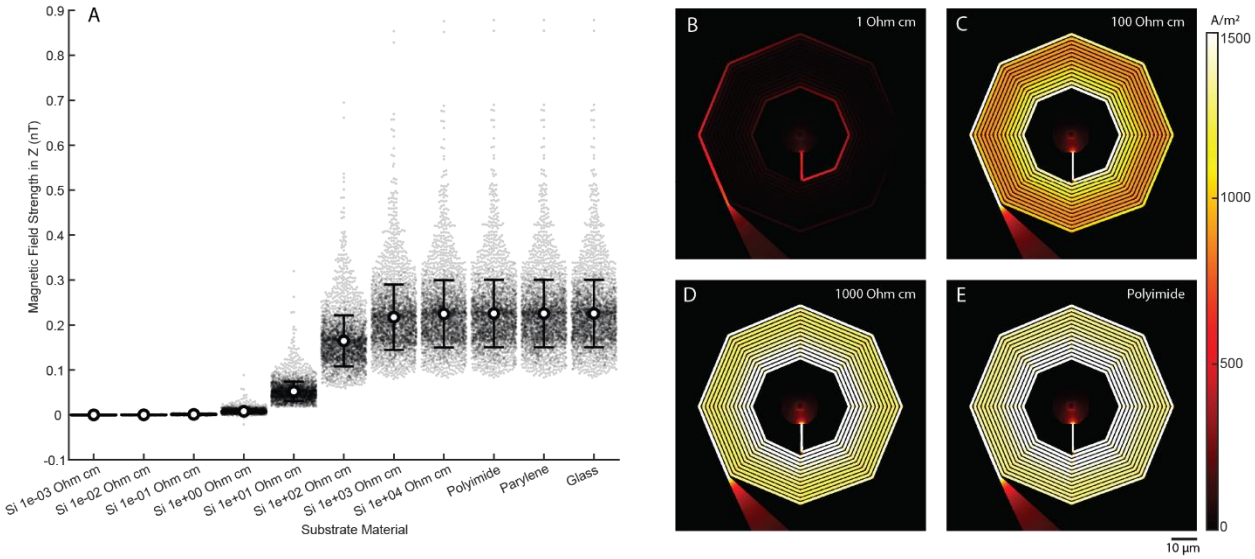

Figure 1.4: Quantification of magnetic transduction on common fabrication substrates. (A) Average magnetic field strength on polyimide, parylene, glass, and silicon substrates with a range of ion implantation doses, measured within XZ planes as in Fig. 1.2 (Error bars, standard deviation. Beeswarms, magnetic field strength at each pixel within measurement plane). (B-E) XY views of the current density on 1 Ω · cm (B), 100 Ω · cm (C), and 1000 Ω · cm (D) silicon, and polyimide (E).

Discussion

Our model validates a new principle for amplifying neurogenic magnetic fields by interfacing single neurons with nanofabricated flat spiral coils. The junction formed between cell and device relies on tight electrical coupling at the interface pad and generates magnetic fields that are enhanced both spatially and in amplitude, compared with the driving NMF. We show that the predicted magnetic field magnitude in response to neural currents surrounding the device is more than three-fold higher in peak amplitude compared to intrinsic NMF, reaching 1.6 nT in the plane of the coil. Averaging the signal over a volume of 40 x 40 x 10 μm^3 results in 640 pT compared with 2.5 pT for a naïve neuron and an overall spatial enhancement of the transduced magnetic field output of more than 250-fold. Our approach brings about immediate relevance to *in vitro* magnetometry but also has potential relevance to modalities such as MRI and MEG, whereby arrays of nanofabricated devices of sufficient density can modulate signal change in response to neuronal activation. Our approach could provide a way to overcome the theoretical limitations of spatial resolution and sensitivity of these modalities that thus far precluded detecting micrometer scale picoTesla events without transcranial wiring at the time of recording.

Effective coupling for remote electromagnetic detection depends on nanofabrication features that dictate impedance and inductance[53–55]. The geometric optimization delivered by our model provides recipes that can be applied on unique substrates for increased magnetic transduction, while adhering to the practical limitations of nanofabrication techniques. One unique avenue for application is nanofabrication of nanocoils on emerging nitrogen vacancy (NV) diamond substrates used for fluorescence-based micro-magnetometry[56,57]. This technology enables highly sensitive magnetic detection of resolved 400 pT transient magnetic events resulting from action potentials in nerve preparations[58] and single-cell superparamagnetic nanoparticle

internalization *in vitro*[59]. These studies could benefit from enhanced fields by arrays of nanocoils that can provide multiplexed single-neuron readouts of neuronal networks, and this modality is sensitive enough to capture the theoretical magnetic output of a single nanocoil device. More broadly, NV diamond magnetometry employs microwave resonance at the 2.87 GHz regime, inviting integration of capacitors into the nanocoil device for microwave resonance and high spatial resolution modulation of fluorescence by magnetic fields. Lithography of high aspect-ratio inductors offers reduced impedance and increased inductive coupling but can also present constraints due to possible structural collapse of device features[60–62]. In this study, we analyzed metallization layers ranging between 100 nm and 1.5 µm, and show a predictably high magnetic field of 0.13 nT produced at the highest thickness with a 1 nA current. We find that thickness of 500 nm with 1020 nm turn width, yielded a comparably strong magnetic field of 0.14 nT, with features that maintain 1:1 or smaller aspect ratio and are well within the capabilities of electron beam lithography and Au growth techniques. Other significant features include the interface pad at the core of the device that acts as a common electrode driving the magnetic field generation at the nanocoil. The size of the coil's open core impacts the size of the interface pad, turn density and overall magnetic field strength. A core with a diameter only 10.9 % the diameter of the nanocoil was found to produce the highest peak magnetic field, (0.27 ± 0.16 nT) but with very high standard deviation across the 12.5 x 50 µm plane tested. A core of a 46.2 %, allowed for a sufficiently large 14.4 µm interface pad, a low variability magnetic field of 0.18 ± 0.06 nT and overall optimal performance.

Our model mimics the generation of ionic currents during action potentials at sub-cellular neurite morphologies on a flat device *in vitro*. Currents propagating in neuronal compartments induce magnetic fields that rotate around the axis of neurite at specific orientations during synaptic events

and aggregate to form a typical MEG signal measured outside of the brain[23,25]. A flat spiral nanocoil interfaced with a neuron is predicted to generate magnetic fields rotating about the turns of the coil, aggregating to a large field spread over an area perpendicular to the plane of the substrate irrespective of the original NMF alignment to the detector. This offers a new repertoire of MEG measurements from untapped anatomical orientations and depths *in vivo*, assuming sufficiently dense multiple aligned coil arrays are implanted. We examined magnetic fields on commonly used implantable substrates including high resistivity silicon, glass, polyimide and parylene. We find no magnetic field loss on these substrates, leading to potential long-term implantation of nanocoils leveraging known chronic biocompatibility for these substrates. Flexible substrates are of particular importance and can facilitate MEG signal enhancements when implanted similarly to dense electrocorticography (ECoG) devices that conform to anatomical features in the brain[63,64]. Such an array of nanocoils would theoretically allow for measurement of single cell activity *in vivo* without the need for transcranial wiring. Moreover, previous MRI phantom measurements of a 30 μm wire demonstrate detectability of fields as low as 200 pT for a 2.5 x 2.5 x 6 mm voxel[65]. Given that our 80 μm device produces a 640 pT volumetric magnetic field, it is feasible that the field produced by a single nanocoil coupled to and transducing the firing of a single neuron will be detectable via MRI. In conclusion, our quantifications institute a foundation for synthesizing minimally invasive electromagnetic sensors for detecting brain activity and can serve as a broad protocol for quantifying sensitivity at the single cell level.

Acknowledgements

Funding

This work was supported by the National Institute of Neurological Disorders and Stroke and the Office of the Director's Common Fund at the National Institutes of Health (grant DP2NS122605

to AH), the National Institute of Biomedical Imaging and Bioengineering (grant K01EB027184 to AH) and the Wisconsin Alumni Research Foundation (WARF).

Author Contributions

AH, MG and JKP designed the research. JKP and MG performed the research. JKP, MG and YG analyzed the data. AA, MD and AH fabricated the device, JKP performed cell imaging and patch clamp experiments. JKP and AH wrote the manuscript.

Chapter 2: Nanofabricated high turn-density spiral coils for on-chip electro-magneto-optical conversion

Ilhan Bok, Alireza Ashtiani, Yash Gokhale, Jack Phillips, Tianxiang Zhu, Aviad Hai

In Press in Microsystems and Nanoengineering

Abstract

Circuit integrated electromagnets are fundamental building blocks for on-chip signal transduction, modulation, and tunability, with specific applications in environmental and biomedical micromagnetometry. A primary challenge for improving performance is pushing quality limitations while minimizing size and fabrication complexity and retaining spatial capabilities. Recent efforts exploit highly involved three-dimensional synthesis, advanced insulation, and exotic material compositions. Here, we present a rapid nanofabrication process that employs electron beam dose control for high turn-density diamond-embedded flat spiral coils achieving efficient on-chip electromagnetic to optical signal conversion. Our fabrication process relies on fast 12.3 sec direct write on standard Poly(methyl methacrylate) as a basis for metal lift-off process. We demonstrate 49 – 470 nm inter-turn spacing and corresponding inductance of 12.3 to 12.8 nH for prototypes with 70 micrometer overall diameter. We utilize optical micromagnetometry to demonstrate magnetic field generation at the center of the structure correlating relatively well with finite element modeling predictions. Further designs based on our process can integrate with photolithography to broadly empower optical magnetic sensing and spin-based computation.

Introduction

On-chip micro- and nano-fabricated inductors, antennas, and electromagnets extend possibilities for compartmentalizing a wide variety of technologies and research applications[66–68]. From wireless communication[69–71], high frequency signal conversion, power transfer and filtering[72–76], to environmental and biological sensing[67,77–80]—new designs are leveraging diverse geometries and material compositions to transform electromagnetic energy at a broad spatiotemporal range. Specific lab-on-chip platforms for magnetic detection and manipulation rely on patterned coils and loops for optical magnetometry[57,81], nuclear magnetic resonance (NMR) spectroscopy and imaging[62,82], magnetic particle separation[83–86], molecular magnetophoresis[87–89], and cell manipulation and labelling[90–93]. Theoretical limitations and fabrication constraints restrict performance and are closely related to quality factor, frequency bandwidth, and temporal response[94–97]. More recent innovative devices demonstrate improved properties by utilizing approaches such as three dimensional fabrication[98–101], mechanically self-assembled coils[101–104], air-core or air-suspended coils[105–107,98] and the use of alternative materials such as graphene, carbon, ZnO and others[108–112]. However, the integration of complex designs into standard fabrication processes is not trivial. Consequently, metal-based flat spiral coils remain the mainstay devices for on chip electromagnetic signal conversion owing to a relatively small number of lithography steps and higher structural and thermal stability. Spiral inductors are integrated in a myriad of recent applications including power harvesting components on flexible and bioresorbable electronic sensors[113–117], recording and stimulation devices for wireless neurological applications[79,118–122] and ingestible electroceuticals[123,124]. Additionally, they empower modalities such as nuclear magnetic resonance (NMR) and biomedical magnetic resonance imaging (MRI) by providing high spatial

resolution microprobes for spectroscopy and imaging[62,82]. While most systems employ microlithography to pattern coil structures, a small number of studies began exploring nano-scale lithography to propel spatial features while maximizing performance. These include electron beam lithography (EBL) for synthesizing meandering inductors with submicron conducting lines[125], complementary metal-oxide semiconductor (CMOS)-compatible glancing angle physical vapor deposition (GLAD) for vertically aligned nanohelices[126], and spiral patterns realized via focused ion beam fabrication (FIB)[127]. The emerging integration of these methods and other promising nanofabrication techniques[128–130] with standard CMOS processes, in particular EBL, highlights opportunities for designing novel rapid fabrication processes for high spatial resolution electromagnetic conversion. In this study we introduce a high density nanofabricated spiral coil design for on chip electromagnetic signal conversion (Fig. 2.1). Modelling predictions of this design allow for predictions of current density (Fig. 2.1a), surface potential (Fig. 2.1b), electric field (Fig. 2.1c) and magnetic flux density (Fig. 2.1d) for a given input, and inform on proper nanofabrication parameters for optimized performance. Using a simplified EBL fabrication process that relies on dose control to achieve high turn-density nanocoils, our process utilizes proximity effect in poly(methyl methacrylate) (PMMA) exposure and metal lift-off to demonstrate tightly packed coils with minimal PMMA collapse, achieving 49.7 nm turn spacing and inductance of up to 12.8 nH for 10 turn prototypes. Using diamond-based optical magnetometry in conjunction with finite element computational modeling, we demonstrate efficient magnetic field generation at the center of the structure. Further designs based on this process can integrate with photolithography to broadly empower electromagnetic circuits for magnetic sensing and modulation.

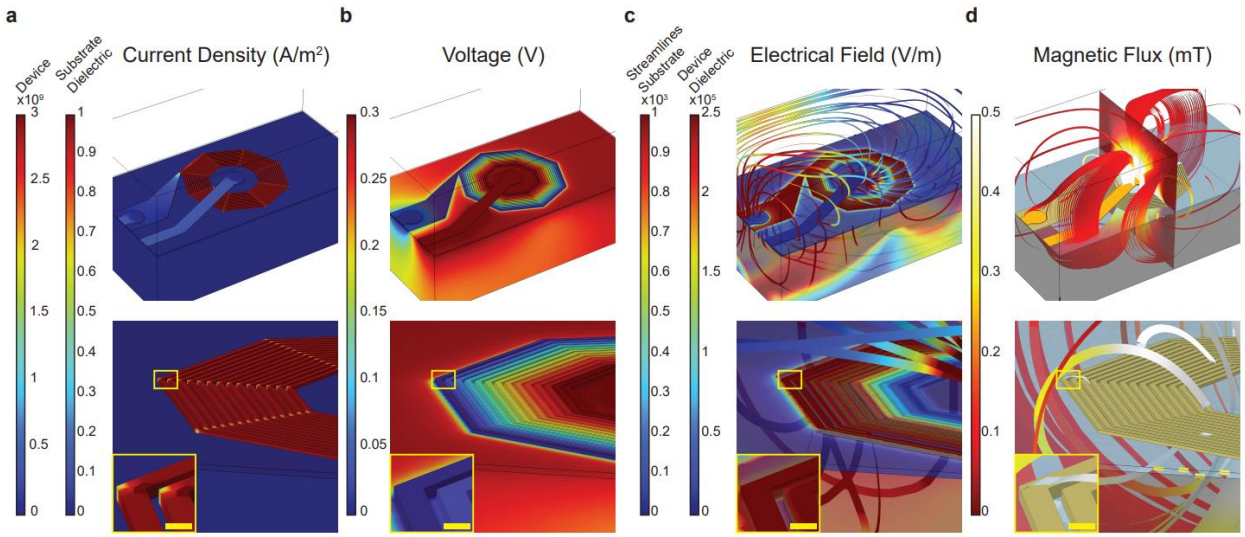

Figure 2.1. Modeled electromagnetic behavior of nanofabricated spiral coil. Nanofabricated spiral coil design and predicted performance on high resistivity substrates. Current density **(a)**, surface potential **(b)**, e-field **(c)** and magnetic flux density **(d)** are estimated in response to a given input current. Inter-turn spacing (*s*) ranging between 49 and 470 nm are demonstrated in this study.

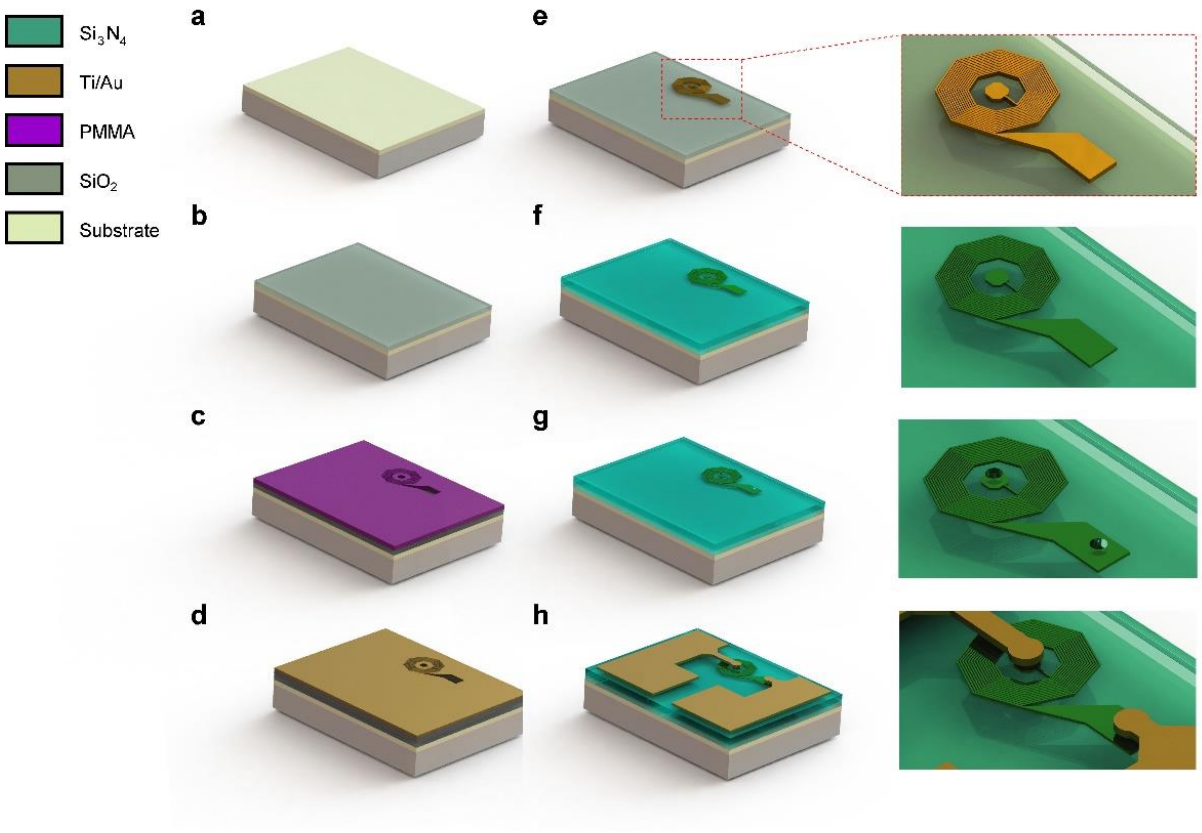

Figure 2.2. Fabrication process overview. (a) The device is fabricated on resistive glass or diamond substrates. **(b)** A 100 nm SiO_2 barrier layer is deposited on surface. **(c)** A 400 nm PMMA layer is spin coated and patterned via EBL to define nanocoil features. **(d)** A Ti/Au (6/60 nm) bi-layer is deposited with e-beam evaporation and is subsequently lifted off to create coil structure **(e)**. **(f)** An additional insulating SiO_2 layer is deposited to prepare for PL micropatterning of electrode routing. **(g)** Via holes are defined via PL and etched with a fluorine-based plasma recipe. **(h)** Finally, patterns for electrode traces are fabricated and gold electrodes are laid via evaporation and lift-off. Samples are further packaged and routed onto glass printed circuit boards for magnetometry.

Results

Following fabrication process development (Fig. 2.2), we synthesized spiral nanocoils using a broad electron beam dose matrix ranging between 320 and 1600 μC/cm^2 (Fig. 2.3). The end device (Fig. 2.3a) exhibits minimum turn spacing (*s*) of 197.8 nm for a dose of 1120 μC/cm^2 (Fig. 2.3a, inset). We utilized proximity effect of an identical pattern to control nanocoil turn width (*w*) and *s* (Fig. 2.3b) while maintaining constant turn density. Doses of 800, 1440 and 1600 μC/cm^2 are shown in Fig. 2.3b, left, middle and right subpanels, yielding a minimum of *s* = 329.6, 300.3 and 139.2 nm, respectively, and an average Ti/Au slope of 50.98 ± 1.14 degrees (1.23 ± 0.05 $nm_{(z)}/nm_{(x)}$) determined by AFM (Fig. 2.3b, insets). To predict the relationship between dose and *s*, we used finite element modeling of electron trajectories in PMMA (Fig. 2.3c-d) demonstrating good correlation (R = 0.96887) between simulated dose response (Fig. 2.3f-h) and *s* in PMMA following development (Fig. 2.3i-j). The mean predicted area for a single exposed dot at 2 nA and 100 keV for a dose of 320 μC/cm^2 (Fig. 2.3f, leftmost panel) was 6.38 nm^2 and increased linearly to 8.71 nm^2 for a dose of 1600 μC/cm^2 (Fig. 2.3f, rightmost panel). The resulting average *s* following lift off ranged between 206.7 and 389.2 nm (Fig. 2.3k-l) for doses ranging between 1440 and 640 μC/cm^2. For this range, we demonstrate an inverse linear relationship between dose and *s* (Fig. 2.3e) corresponding to a surface resistance ranging between 349.58 and 397.16 kΩ/m for the same metal film thickness across all devices.

High current amplitude range during normal device operation can result in high ohmic loss and a localized hot region with changes as small as 10 mK in ambient temperature resulting in magnetic field change of ~30 nT and reduced accuracy[131]. Dose selection can be used to mitigate such alterations in device characteristics by adapting impedance and turn density to the expected current range and maximizing coil fill factor[132]. This can be achieved by increasing the dose of electron

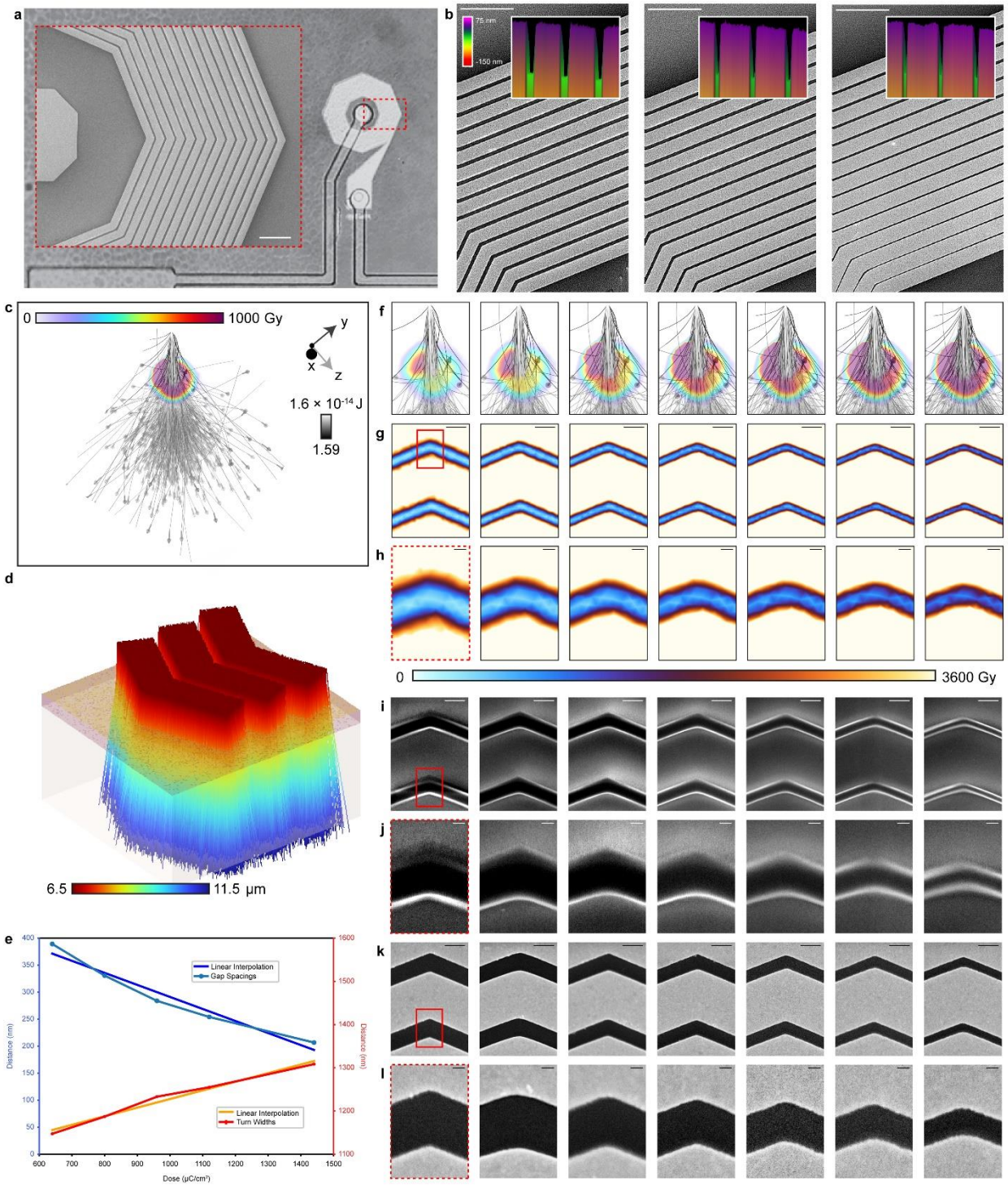

Figure 2.3. Dose dependent feature analysis of nanofabricated spiral coils. (a) A complete view of the end device. The dotted red region is portrayed as a scanning electron microscopy (SEM) image of the EBL step in the left inset, showing distinct uniformity of turns for a dose of

1120 μC/cm^2 (scale bar = 5 μm). Different doses with closest corresponding AFM traces are shown in **(b):** 960 μC/cm^2 (left), 1280 μC/cm^2 (center), and 1600 μC/cm^2 (right; scale bar = 5 μm), with corresponding 3-dimensional AFM traces color-coded by height (insets). **(c)** Single pixel Monte Carlo simulation of PMMA exposure where 1 Gy ≡ 7.366 eV/cm^3 and **(d)** corresponding triple turn simulation color-coded by particle trajectory height. Gold, magenta, and cream-colored layers correspond to gold, PMMA, and quartz, respectively. **(e)** Average turn widths and gap widths versus dose, determined using atomic force microscopy, showing a linear relationship between dose and feature size. Shown at right is a matrix comparing **(f)** single-pixel Monte Carlos, **(g)** multi-turn Monte Carlos **(h)** (with zoomed regions of interest), **(i)** PMMA pre-liftoff **(j)** (with close up ROIs), and **(k)** Ti/Au post-liftoff **(l)** (with closeup ROIs), respectively. Columns from left to right correspond to doses of 320, 480, 640, 800, 960, 1120, 1280, 1440, and 1600 μC/cm^2, respectively (scale bar = 500 nm (overview panels) or 100 nm (zoomed ROIs)).

beam exposure (Fig. 2.4). Whole-coil resistance (Fig. 2.4b), parasitic inter-turn capacitance (Fig. 2.4c), Wheeler[133] and sheet[132] spiral coil inductance estimates (Fig. 2.4d), and corresponding Q factor (Fig. 2.4e), and self-resonance (Fig. 2.4f) are plotted with respect to dose. Q factor and resonance frequency can be tuned by dose selection with lower doses suitable for improved Q factor but increased resistive heating. For the resonance frequencies shown here (Fig. 2.4g) impedance is the major contributor to higher loss whereby Q is reduced by 16.9 % from 1.76 (1.78) to 1.46 (1.47) using Wheeler (Sheet) estimates for doses of 1440 μC/cm^2 and 640 μC/cm^2 and corresponding self-capacitance of 3.3 fF and 6.3 fF and resistance of 1089.8 Ω and 960.1 Ω, respectively. In addition to performance considerations, dose control presents possibilities for frequency tuning (Fig. 2.4e and g) demonstrating average frequency shifts of 0.92 ± 0.36 GHz per 100 μC/cm^2.

A relatively constant inductance is concomitant with evenly spaced coil turns and serves as a foundation for optimizing all other parameters. Measurements of turn slope using atomic force microscopy (Fig. 2.4a, pink) and scanning electron microscopy (Fig. 2.4a, red) show asymptotic decreases in slope with increased dose, in agreement with our Monte Carlo finite element analysis model. Vertical slant has the potential to impact heat dissipation and capacitive coupling enabling further optimization of coil behavior for applications *in vivo*. Comparing the impedance in decibel ohms to linear frequency reveals a dose-dependent tuning curve (Fig. 2.4g) with varying resonant frequency and Q factor (Fig. 2.4g, inset).

To fully explore the parameter space of coil characteristics, we quantified dose-dependent power dissipation using our finite element analysis (Fig. 2.5). A full view of the nanocoil (Fig. 2.5a) corresponding to a dose of 640 μC/cm^2 with the coil surface color-coded by x-component of the Poynting vector (Po_x) and plane of coil color-coded by magnetic energy density (J/m^3) reveals

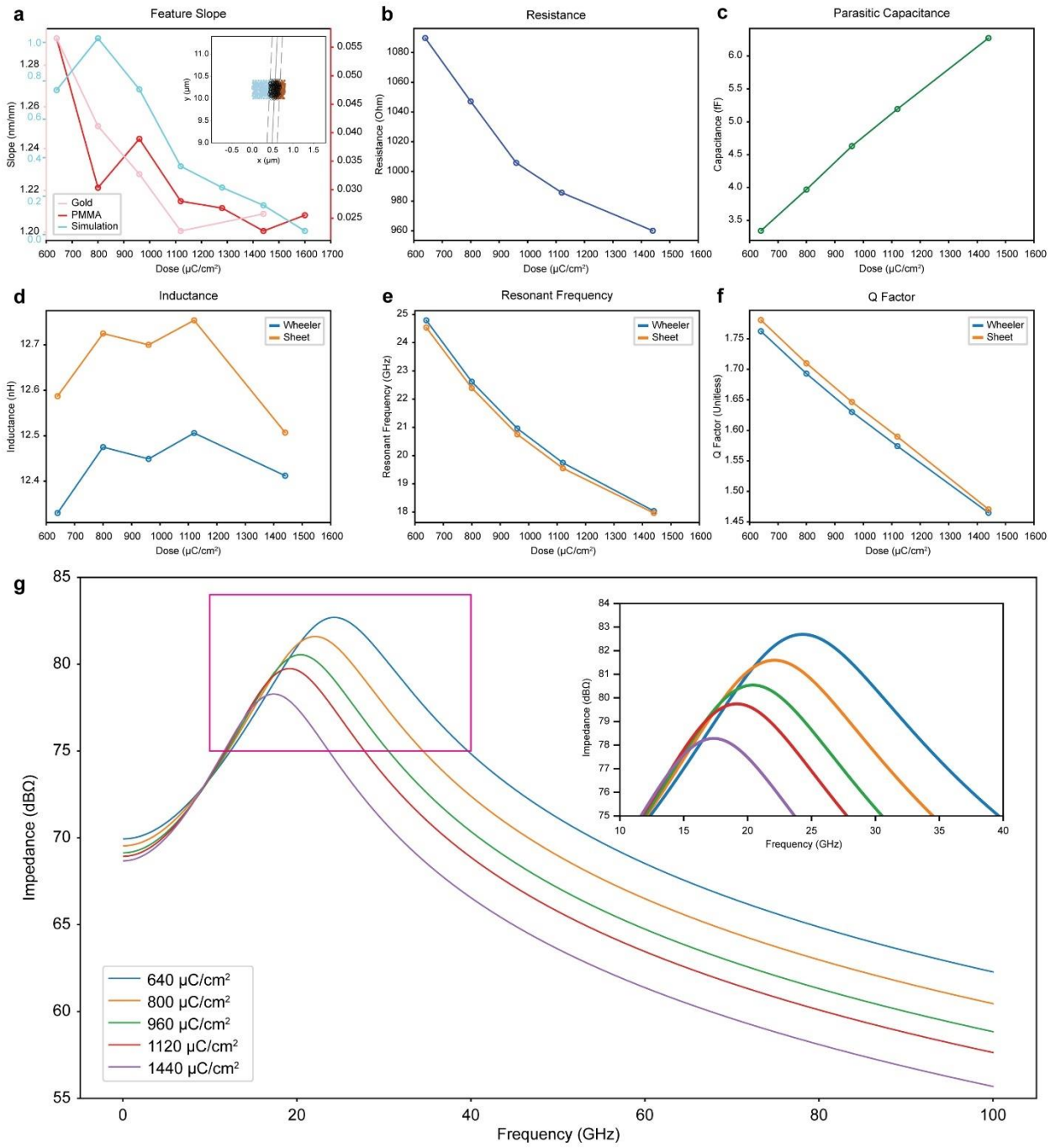

Figure 2.4. Nanocoil feature measurements and fitness calculations. (a) Finite element analysis (cyan) reveals slope trends in agreement with AFM (pink) and SEM (red) measurements. Inset shows an example support vector machine (SVM) regression of PMMA slope. Blue and orange dots represent mesh points with subthreshold and suprathreshold exposure, respectively. The solid

line and dashed lines represent the optimal hyperplane and margin, respectively. (b) Whole-coil resistance and (c) parasitic inter-turn capacitance. Wheeler method and sheet spiral inductance calculations are shown in (d), with the corresponding self-resonance (e) and Q factor (f). All quantities are plotted versus electron beam dose ranging from 640 to 1440 μC/cm^2 except for SEM data which extends to 1600 μC/cm^2. Comparing the impedance in decibel ohms to linear frequency reveals a dose-dependent tuning curve (g) with varying resonant frequency and Q factor (inset).

significant stratification within the coil and gradients outside the coil for a 3 mA applied current. The red dashed box in Fig. 2.5a corresponds to regions expanded in Fig. 2.5g and Fig. 2.5h. A subtraction histogram between high dose (1440 μC/cm^2) and low dose (640 μC/cm^2) vector count versus angle color-coded by magnitude reveals stark differences in directionality surrounding 90 degrees corresponding to the plane of the coil (Fig. 2.5a, inset). Integrating the vector magnitudes of X, Y, and Z components $|| \oiint_{coil} Po_x \, \hat{x} + \oiint_{coil} Po_y \, \hat{y} + \oiint_{coil} Po_z \, \hat{z} ||$ of dissipated power versus dose over the entire coil surface demonstrates a linear trend between electron beam dose-dependent turn width and dissipated power (Fig. 2.5b). Two-dimensional (2D) Poynting vector x (Po_x), y (Po_y) and z (Po_z) plots for 640 μC/cm^2 (Fig. 2.5c, e and g) and 1440 μC/cm^2 (Fig. 2.5d, f and h) show significant changes in power distribution with dose. Separate surface integrals of the X, Y, and Z components of the Poynting vector also affirm linear relationships between electron beam dose-dependent turn width and dissipated power (Fig. 2.5i). These results provide a basis for optimizing power characteristics for nanofabricated coils on diamond.

To quantify the B-field strength developing in the device in response to injected current and to verify conformity with our modeling predictions, we turned to using optically detected magnetic resonance (ODMR) micromagnetometry forming an electromagnetic to optical junction on-chip (Fig. 2.6). Nanocoils embedded in nitrogen vacancy (NV) diamond samples were excited at 532 nm and RF-irradiated at frequencies ranging between 2.78 and 2.96 GHz in the presence of a DC magnetic field (0.8 mT) (Fig. 2.6a). We compared two different routing configurations to account for electrode path contributions to the magnetic field (Fig. 2.6b-c, upper left panels). RF spectra were acquired in conjunction with optical collection at 637 nm with and without current injection (bottom left and bottom right panels in Fig. 2.6b and c, respectively). The mean amplitude of the magnetic B-field strength across the nanocoil was 0.18 ± 0.08 mT (Fig. 2.6b) and 0.28 ± 0.003

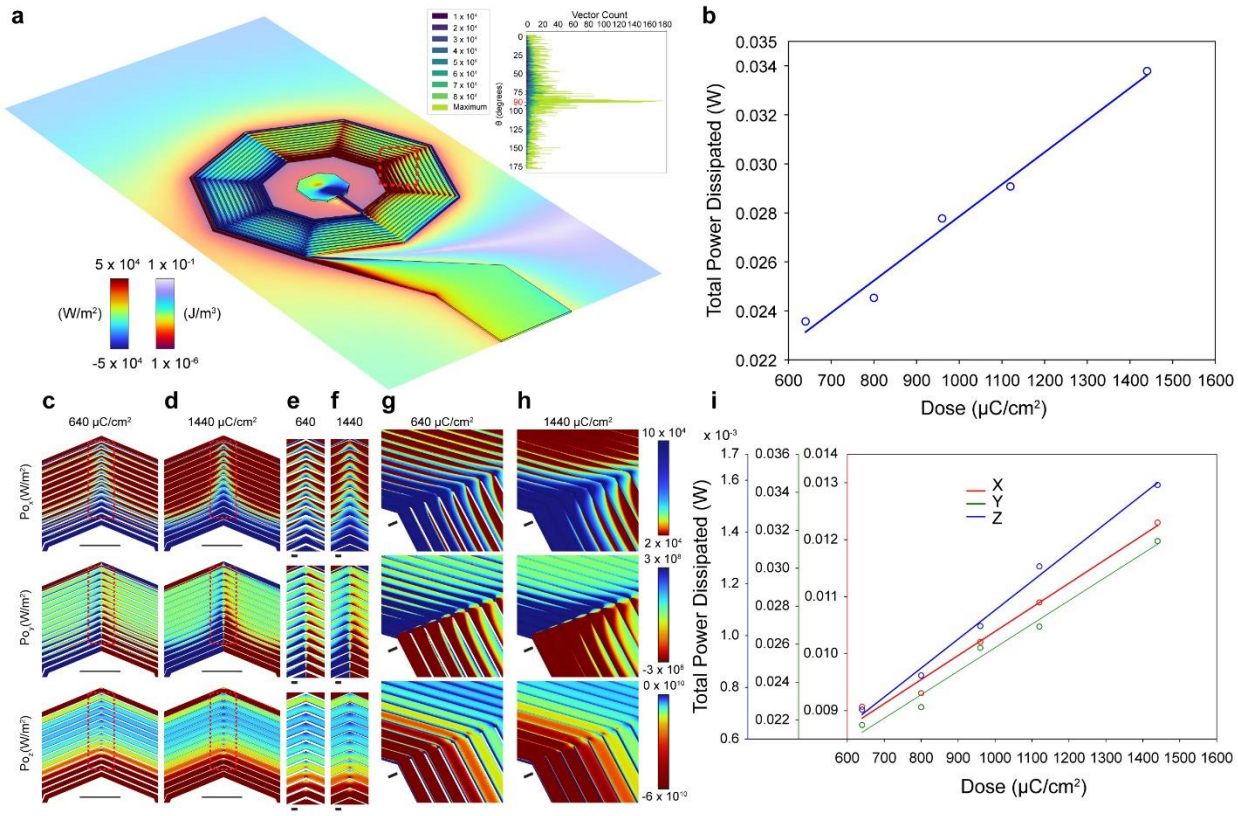

Figure 2.5. Dose-dependent power dissipation quantification and analysis. (a) Full view of the nanocoil (dose: 640 μC/cm^2) with coil surface color-coded by x-component of the Poynting vector (Po_x) and plane of coil color-coded by magnetic energy density (J/m^3). The red dashed box shows the regions expanded in (g) and (h). Inset: subtraction histogram between high dose (1440 μC/cm^2) and low dose (640 μC/cm^2) vector count versus angle color-coded by magnitude. **(b)** Vector magnitude for the integral of X, Y, and Z components $|| \oiint_{coil} Po_x \, \hat{x} + \oiint_{coil} Po_y \, \hat{y} + \oiint_{coil} Po_z \, \hat{z} \, ||$ over the entire coil surface of dissipated power versus doses examined with lines of best fit affirming a linear trend between electron beam dose-dependent turn width and dissipated power. **(c-h):** Two-dimensional (2D) Poynting vector x (Po_x), y (Po_y) and z (Po_z) plots for 640 μC/cm^2 **(c** and **e)** and 1440 μC/cm^2 **(d and f)** for dashed box in a (**c** and **d**, scale bar = 10 μm) and zoomed inset (red dashed boxes, **e** and **f**, scale bar = 1 μm). Three-dimensional (3D) plots of corresponding regions for 640 μC/cm^2 **(g**, scale bar = 1 μm**)** and 1440 μC/cm^2 **(h**,

scale bar = 1 μm**).** **(i)** Separate surface integrals of the X, Y, and Z components of the Poynting vector demonstrating linear relationships between electron beam dose-dependent turn width and dissipated power.

mT, Fig. 2.6c) for the two configurations, demonstrating no significant difference ($p = 7.06 \cdot 10^{-5}$ across 80 μm diameter field of view surrounding coil center). Respective B-field maps predicted by finite element simulations show mean B-field amplitude of 0.08 ± 0.03 mT corresponding relatively well with measurements ($R = 1.2 \cdot 10^{-2}$). To confirm sufficient magnetic field uniformity across the coil surface, we quantified magnetic field gradients (Fig. 2.6d-g) to generate corresponding uniformity maps from ODMR measurements (Fig. 2.6h-i) and compare our measurements to finite element simulation results (Fig. 2.6j). We find that uniformity within the sensing region of the coil region is within ±1.2 % with regions outside the coil experiencing slightly higher field inhomogeneity (< ±3 %) correlating well with our simulation results. Finally, we measured a maximal B-field of 0.25 ± 0.03 mT (Fig. 2.6k) and 0.38 ± 0.08 mT (Fig. 2.6l) at the center of the nanocoils for both configurations, occupying an area of $1.26 \cdot 10^3$ μm^2 and corresponding to a predicted maximal B-field of 0.47 ± 0.13 mT interpolated over 1 μm pixel size in the model.

Discussion

These results demonstrate an electromagnetic-to-optical junction mediated by nanofabricated spiral coils that present new possibilities for diamond-based optical magnetometry[57,81] and emerging optical NMR detection schemes[134,135]. Using our protocol for careful control of self-resonance in conjunction with integration of additional capacitive elements, standalone devices can in the future be specifically tuned to 2.87 GHz frequencies for efficient (on resonance) *in situ* RF irradiation of NV diamond layer embedded nanocoils. Further, the utilization of dedicated pulse sequences with modified photonic and RF temporal signatures can increase contrast and sensitivity[136,137]. Combined with tuned resonance, this type of configuration is expected to increase RF energy harvesting and greatly improve ODMR sensitivity, potentially broadly

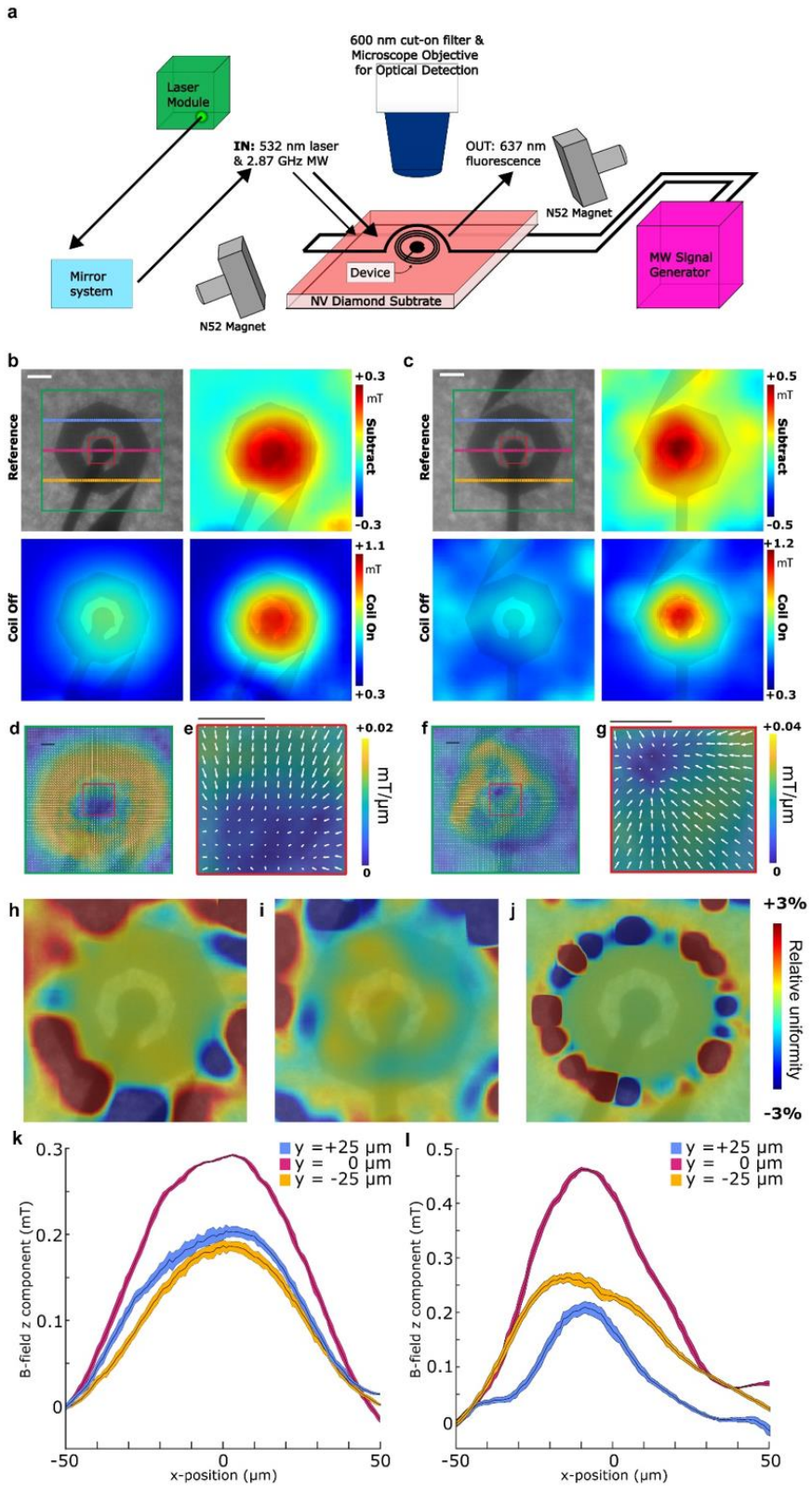

Figure 2.6. Optical magnetometry measurements of nanocoil B-field strength during current injection. (a) Experimental setup. (b)-(c) B-field maps of two different device routing

configurations. Top left: reference image with delineated line scans, bottom left: B-field amplitude (0 mA DC), bottom right: B-field amplitude (3 mA DC), top right: current OFF minus current ON subtraction; B-field z component. (d)-(g) Vector field lines of B-field gradient overlaid on B-field maps. (e) and (g) correspond to dashed boxes in (d) and (f), respectively. (h)-(i) Uniformity maps comprising vector field lines of B-field gradient overlaid on corresponding B-field gradient maps. (j) Simulation of uniformity map for comparison. (k)-(l) 100 μm line scans of B-field z component for (b) and (c) respectively taken at y = +25, 0, -25 μm from device center. Scale bars = 20 μm.

impacting quantum information storage and computing by incorporating substrate-integrated patterned nanocoil arrays to augment spin-based computational elements.

Materials and methods

Nanofabrication process development

The fabrication process consists of three main steps: (1) high fill-factor nanocoil electron beam lithography (EBL) on resistive substrates; (2) Photolithography (PL) for micro-patterning of nanocoil contacts and die routing; and (3) wire bonding and encapsulation onto glass printed circuit board for micromagnetometry measurements. We used standard lift-off (Fig. 2.2) on either glass (76.22 mm Borofloat 33, 500 µm thick wafers) or diamond (3.6 x 3.6 mm electronic-grade 400 µm thick samples, 10 µm ~3.8 ppm nitrogen vacancy layer, Element six, Santa Clara, CA). Samples were cleaned using Isopropyl alcohol (IPA) and dried with N_2 (100%) for EBL preparation (Fig. 2.2a) followed by deposition of a 100 nm SiO_2 barrier layer (Fig. 2.2b) by plasma-enhanced chemical vapor deposition (PECVD) (PlasmaTherm 73/72, Saint Petersburg, FL) with chamber temperature of 250º C, 810 standard cubic centimeters per minute (SCCM) N_2O, 440 SSCM 2% Silane, 900 mT pressure and 36 W radio frequency (RF) power, at 100 s deposition time. During process development on diamond samples, the barrier layer was etched and redeposited several times using buffered oxide etch (BOE 6:1) for 10 minutes and rinsed with deionized (DI) water, with no observed injury to nitrogen vacancy (NV) diamond layer or bulk substrate. Following deposition, samples were spin coated (Fig. 2.2c) with PMMA 950K A7 (M230002, Kayaku Advanced Materials Inc., Westborough MA) at 3600 rotations per minute (RPM) for 60 sec and then baked at 180º C for 2 min to yield typical resist thickness of 400 nm. We used EBL (Elionix ELS G-100, 100 keV, 2 nA, 2.5 nm pixel size, 0.01-0.05 µs dwell time for doses 320-1440 µs/cm^2, 500 µm field size) to test a high beam exposure matrix ranging between

320 and 1600 μC/cm^2 for over-exposing nanocoil features to widen turn width and narrow turn spacing (*s*) in the resist during development. Samples were developed with IPA:MIBK (2:1) (2 min). A dose of 800 μC/cm^2 yielded 330 nm spacing reproducibly. Based on EBL optimization and following PMMA development, samples were rinsed with IPA and DI water, and dried with N_2 prior to metal deposition and lift off (Fig. 2.2d and e, respectively). After a 10 sec oxygen plasma treatment to descum surface (YES R3 Plasma Asher, 250 W, 80 SCCM O_2) a Ti/Au (6/60 nm) metal bilayer was deposited via e-beam evaporation without breaking vacuum (Fig. 2.2d). The nanocoil was then realized by lift-off in an ultrasonic bath at medium-high vibration rate with remover (Microposit Remover 1165, Kayaku Advanced materials Inc., Westborough MA) for 10 minutes (Fig. 2.2e) followed by DI water rinse and N_2 drying. An additional 400 nm SiO_2 insulating layer (Fig. 2.2f) was deposited via PECVD (250º C, 810 SCCM N_2O, 440 SSCM 2% Silane, 900 mT pressure, 36 W RF, 100 s deposition time) as a pre-step to micropatterning of contacts by PL.

Contacts micropatterning and outside routing

Since nanofabrication is the only dimensionally critical step in our process, our protocol follows with optical microlithography for fabricating electrode contacts to connect the coil to outside circuitry. Insulated substrate was spin coated with S183 photoresist (30 s, 3000 RPM, 1.3 μm thickness) baked at 110 º C for 1 min, followed by soft contact lithography (Karl Suss MA6, 9.5 s exposure time, 10 mW/cm^2 broadband mercury lamp) to pattern via holes at the coil interface pads (Fig. 2.2g). Samples were developed in MF-321 (Kayaku Advanced Materials Inc., Westborough MA) for 60 sec, washed with DI water and dried with N_2. Holes were etched in RIE chamber with a CF4-based recipe (PlasmaTherm 790, chamber temperature 40 C, 45 SCCM CF4, 5 SCCM O2, 40 mT pressure, 100 W RF power, etch time of 360m) washed with DI water and

dried with N_2 to expose nanocoil metal contact pads (Fig. 2.2g, inset). This was followed by an additional lithography step and lift-off process to generate electrode traces for on-chip routing (Fig. 2.2h) using APOL-LO 3204 negative photoresist (KemLab Inc., Woburn, Massachusetts, USA) spin coated at 4000 RPM for 30 s and soft baked at 110º C for 1 min. Contact PL was performed with 15 s exposure time (Karl Suss MA6, 10 mW/cm^2) followed by post exposure bake at 110º C for 1 min. Finally, the sample was developed with MF321 for 2 min, rinsed with DI water and dried with N_2. To verify via walls were covered with gold and to create a reliable contact with nanocoil contact pads, a 400 nm gold was evaporated using e-beam, and lift-off was done with recipe used for PMMA/Ti/Au lift-off described above for nanocoil fabrication. Printed glass circuit boards for die wire bonding were fabricated on 3x2-inch glass substrate (Fisherbrand™ Extra-Thick Microscope Slides, 1.2 mm thick) using APOL-LO 3204 photoresist with identical recipe used for contact micropatterning described above: A Ti/Au (10/200 nm) layer was deposited using e-beam evaporation followed by lift-off procedure. To bond the die to the glass printed circuit board (PCB), we used SU-8 2002 (Kayaku Advanced Materials Inc., Westborough MA) by depositing a small (1 µl) droplet on the glass surface at the chip bonding area, followed by hot plate curing at 95º C for 5 min to homogenize SU-8 temperature. The die was then placed on the PCB on the hotplate on top of the non-crosslinked SU-8 for 5 min to let viscous SU-8 gradually reflow under the die. Subsequently, to create a permanent bond, the sample was treated with UV flood exposure and post exposure bake at 95º C for 5 min. Next, manual gold wire bonder (KS-4524, K&S, Fort Washington, PA) was used to connect electrodes to the PCB gold traces. Finally, gold traces on the PCB were connected to co-axial SubMiniature version A (SMA) adapters (#132134-10, Amphenol Connex, Wallingford, CT) with a conductive silver ink cured in room temperature for 15 minutes.

Optical Micromagnetometry

Optically detected magnetic resonance (ODMR) micromagnetometry was used to visualize magnetic field in devices utilizing a 50 mW 532 nm laser (OBIS 532-80 LS 1264453, Coherent, Santa Clara, CA) in NV diamond-embedded nanocoils. A printed microwave antenna (1 mm diameter) was used to deliver RF to the NV layer underneath the coils in conjunction with laser excitation. Microwave signals were generated using RF signal generator (SG 384, Stanford Research Systems, Sunnyvale, CA) fed through RF amplifier (Mini-circuits ZHL-16W-43-S+, Scientific Components Corp, Brooklyn, NY) connected to the antenna. A direct current (DC) bias magnetic field was applied using a 1.48 T magnet (B333-N52, KJ Magnets, Pipersville, PA) placed approximately 4 inches away from the sample. The bias field at the sample was estimated to be 0.8 mT. Fluorescence signal changes during current injection at the device were captured using an upright microscope (SM-LUX HL, Leica Biosystems, Wetzlar, Germany) mounted with a CMOS camera (CS165MU1, Thorlabs Inc. Newton, NJ) operating at 12 frames/sec and a resolution of 720 x 540 pixels with corresponding region of interest (ROI) size of 527 by 395 μm. A total of 181 frames surrounding resonance at ~2.87 GHz were acquired while sweeping between 2.78 and 2.96 GHz at 1 MHz intervals for a total of 181 data points per pixel and acquisition time of 15 minutes. Image capture and delivery of microwave and laser were directly controlled through MATLAB (MathWorks, Inc. Natick, MA, USA) interface and in-house routines. Magnetic field strength was converted from microwave stimulation frequency through:

$$\Delta E = g_L \mu_B m_j B \quad [1]$$

$$B = \frac{2\pi h\nu}{g\mu_B} \quad [2]$$

Where ΔE is the magnetic interaction energy due to the Zeeman effect, μ_B is the Bohr magneton, m_j is total angular momentum, and B is the magnetic field. Native noise level was quantified over all sweeps per measurement.

Atomic Force Microscopy

A Bruker Dimension Icon Atomic Force Microscopy (AFM) System operating in tapping mode with TESPA-V2 tips was used to scan the nanocoils. A 50 µm wide field of view (FOV) was surveyed at a scan rate of 0.1 Hz to reduce tip and sample wear and improve image quality. Scans were imported into Bruker Nanoscope Analysis 2.0, sectioned, and exported as XZ plane height maps for further processing using Python. Turn width and spacing were determined using a partition threshold of 40 nm above the previous gap minimum. Mean turn width and spacing for all 14 turns and 13 gaps were plotted for comparison.

Finite element Analysis

Simulations of electron beam dose trajectories and device magnetic response were performed in COMSOL multiphysics simulation environment (COMSOL Inc., Stockholm, Sweden). Optimized coil pattern described previously[122] and used here for nanofabrication was imported to COMSOL and extruded 500 nm along the z-axis. The dielectric layer was 900 nm thick above the substrate, providing 400 nm of separation between the device and the electrode contacts. Cylinders with a diameter of 8 µm were extruded through the dielectric over the interface pad and ground pad, and microfabricated electrode contacts were patterned above the dielectric and extruded to a thickness of 400 nm. The device had 14 turns, resulting in an open core percentage of 46.2%. The electrical properties of the device and microfabricated electrode contacts were set to those of gold, $\varepsilon = 1$, $\mu = 1$, $\sigma = 45.6 \cdot 10^6$ S/m. The electrical properties of the substrate and dielectric layer in the model were set to those of silicon dioxide (SiO_2) , ε=4.2, μ=1, σ=1e-15 S/m.

The electrical properties of the space above the device were set to those of air, $\varepsilon=1$, $\mu=1$, $\sigma=0.7$ S/m. All device geometries were tested using an input current of 3 mA. The current was input through the outside face of the microfabricated electrode contact connecting to the interface pad at the center of the inductor. The outside face of the electrode contact above the ground pad was used as the ground port.

Monte Carlo modeling of electron trajectory and sample exposure was performed using the charged particle tracing (cpt) module. A pattern consisting of three 1.02 μm wide nanocoil turns was constructed within a simulation arena defined as a $7 \times 7 \times 7$ μm^3 region of vacuum. A base layer of quartz glass 3 μm thick with $\varepsilon=4.2$, $\sigma=1e\text{-}14$ S/m, and $\rho=2210$ kg/m^3 was used as the substrate. A layer of 400 nm thick Microchem 950 PMMA resist was placed atop the substrate with $\sigma=1\cdot10^{-19}$ S/m and $\rho=1180$ kg/m^3. A titanium surface with $\varepsilon=1\cdot10^{100}$ (virtually ∞) and $\sigma=2.6e6$ S/m was assigned to the top of the PMMA. We applied an inlet boundary condition with 3056 randomly positioned particles per release with 1000 releases over a period of 32 ms. The particles had an initial kinetic energy of 100 keV. A normally distributed random velocity component normalized to 5% of the Z component velocity was applied in the X and Y directions. Electron interaction within the PMMA was modeled using particle matter interaction using a cutoff energy of 8.6 eV, with both nuclear stopping and ionization loss sub nodes. A cutoff screening angle of 0.1 degrees and an electronic stopping power of 4 (MeV cm^2)/g were used for each condition, respectively. We also applied velocity reinitialization to the PMMA, with 40% likelihood of one secondary particle having an equal speed as the primary particle but a randomly chosen direction being released. Particle matter interaction was modeled in the quartz layer using nuclear stopping with a cutoff angle of 0.1 degrees. We applied the electric currents (ec) module with the substrate initially grounded to accurately portray current discharge by grounding the bottom of the substrate.

Within this module, a 10 nm thick layer of conductive electrical shielding was used to model titanium.

Acknowledgments

This work was supported by the National Institute of Neurological Disorders and Stroke and the Office of the Director's Common Fund at the National Institutes of Health (grant DP2NS122605 to AH), the National Institute of Biomedical Imaging and Bioengineering (grant K01EB027184 to AH). This material is also based upon research supported by the US Office of Naval Research under PANTHER award numbers N00014-23-1-2006 and N00014-22-1-2371 to A.H. through Dr. Timothy Bentley. The authors thank Hunter Davis, Mikhail Shapiro, Ronald Walsworth, Matthew Turner and Shimon Kolkowitz for useful assistance with NV diamond magnetometry.

Contributions

IB, AA and AH designed the research. AA performed fabrication. YG and TZ built instrumentation, AA and YG performed magnetic measurements. IB and JKP performed modelling. IB, AA and AH wrote the manuscript.

Chapter 3: Magnetic Detection of Neural Activity Using a Nanocoil Transducer

Ilhan Bok, Jack Phillips, Eduardo A. Lima, Jennifer Lu, Elizabeth Detienne, Yingxi Lin, Benjamin P. Weiss, Alan Jasanoff, Aviad Hai

In Preparation

Abstract

Electrophysiological recordings from single brain cells are performed routinely using electrodes implanted into neural tissue, but they traditionally require a wired connection to the outside of the brain. A completely passive, cellular-scale wireless device that does not require on-board power for active transmission—but that still facilitates remote and sensitive detection—could open the door for mass-scale direct recording of action potentials and transform the way we acquire brain signals. We present a non-powered nanofabricated coil that forms an electromagnetic junction with cortical neurons. We show that this micron-scale device enables remote magnetic detection of neuronal field potentials from the center of the coil using a room temperature superconducting quantum interference device (SQUID) magnetic microscope. This strategy may permit detection of neural signals at cellular level using noninvasive readouts like magnetoencephalography and magnetic resonance imaging.

Main

Technologies for accessing the central nervous system are accelerating towards completely injectable probes that interact with noninvasive readout modalities for detection outside of the brain[120,138,41–43,139,50,140,10,141,142]. Neuronal currents are usually measured and

amplified by invasive tethered devices[20]. Quantification of neuronal magnetic field perturbations resulting from these currents, for the purposes of detection by noninvasive modalities outside of the brain, have been explored both theoretically and experimentally[27,143,34,144]. Contemporary estimates place magnetic flux density near single dendrites at 1 nT or lower, falling to zero within less than 1 μm from the plasma membrane[27]. These are considered too minute for detection based on spatiotemporal resolution, neuronal asynchrony and theoretical sensitivity considerations[31]. Arrays of superconducting quantum interference devices (SQUIDs) and more recent optically pumped magnetometers are used for magnetoencephalography (MEG) to detect fields with a magnitude of 0.1 pT or higher ~10 mm outside of the brain; but they require synchronous population activity from at least ten thousand cells in spatially constrained cortical columns tangentially aligned to the magnetic detectors[23,144].

Developing cellular-scale elements that adhere to single neurons and amplify neuronal magnetic fields *in situ*, can present a way to overcome spatial and sensitivity limitations and empower functional magnetic resonance imaging (fMRI) and MEG to directly detect deep neuronal currents with precision. Here, we present a strategy whereby nanofabricated gold electromagnetic coils (nanocoils) can be tightly interfaced with excitable cells, resulting in a neuro-electromagnetic junction that enables magnetic detection of electrophysiological currents at sub-millisecond temporal resolution. Using room temperature superconducting quantum interference device (SQUID) microscopy, we demonstrate magnetic recording of neuronal action potentials from live cortical neurons at the center of the nanocoil.

We fabricated suitable devices using nanometer-scale electron beam lithography on top of silicon-oxide on high resistivity silicon (>5,000 Ω·cm) (Fig 3.1a). A ten-turn coil pattern with 100-200 nm conducting lines interspaced by 700-800 nm (Fig 3.1b,c) was patterned using direct write

followed by deposition of Ti/Au (10/100 nm) for coil turn aspect ratio of 1:1. The prototype has an estimated DC inductance of 5.7-7.2 nH according to common models[122,132], and sheet resistance of 2.87 kΩ. For this study we used a large (30 μm wide) exposed Ti/Au (10/300 nm) ground reference pad to face the extracellular electrolyte solution, and protruding mushroom-shaped pillars at the neuronal interface pad to increase cell-device coupling[20,145] (Fig. 3.1d). This configuration is predicted to generate a relatively large differential potential (> 5 mV) between the pads in response to a single neuronal action potential (~80 mV), resulting in current amplitude > 4 nA (Fig. 3.1e). This amounts to a maximum magnetic field strength of 0.89 nT in the middle of the coil and an average field of 0.08 nT within the coil radius, based on Biot-Savart calculations.

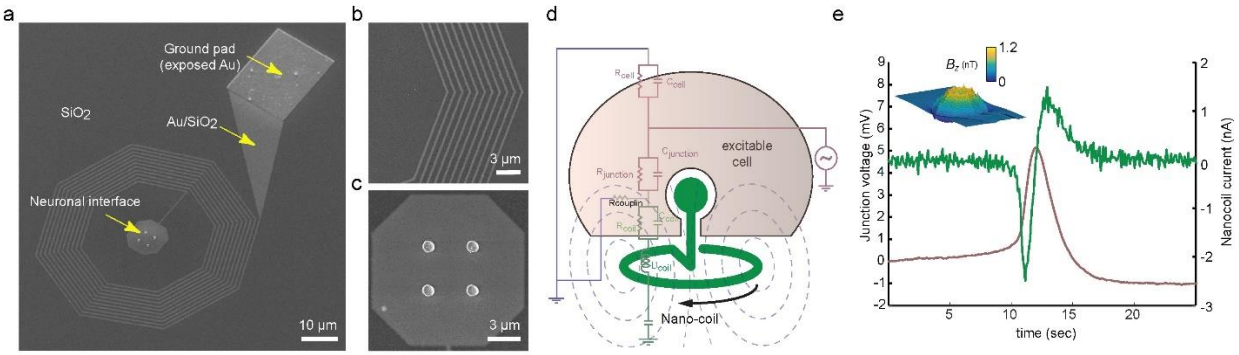

Figure 3.1. Nanocoil for magnetic sensing of neural electrical activity. **(a)** Nanofabricated coil element consists of ten-turn coil structure electrically isolated from the electrolyte by silicon oxide, a neuronal interface pad with protruding exposed gold pillars, and a large gold reference pad facing the extracellular solution. **(b)** coil structure with turn conductor width of 100-200 nm. **(c)** Example of a neuron-interface pad with four protruding elements (width/height ~300 nm). **(d)** Equivalent circuit of junction between nano-coil and excitable cell. **(e)** Circuit simulations indicate junction potential > 5 mV resulting in nanocoil current > 4 nA in response to 80 mV intracellular action potential.

We measured the strength of magnetic fields developing in the nanocoil during physiologically-relevant current injections (Fig. 3.2) using superconducting quantum interference device (SQUID) microscopy at room temperature[146,147] with spatial resolution of 5 μm and

magnetic field spectral power density $S_B^{1/2} < 1.5$ pT/Hz$^{1/2}$. Application of 1 µA (DC) current yielded field strengths ranging between 5 and 10 nT within the radius of the coil (Fig. 3.2a-b)**.** AC currents at millisecond durations and at amplitudes ranging between 500 pA and 50 nA resulted in magnetic field strength values ranging between 5 pT and 0.15 nT (Fig. 3.2c-d). Application of currents 50 pA or smaller yielded no measurable magnetic field averaged across 1,000 epochs suggesting this value to be the sensitivity limit of our system (Fig. 3.2d, bottom).

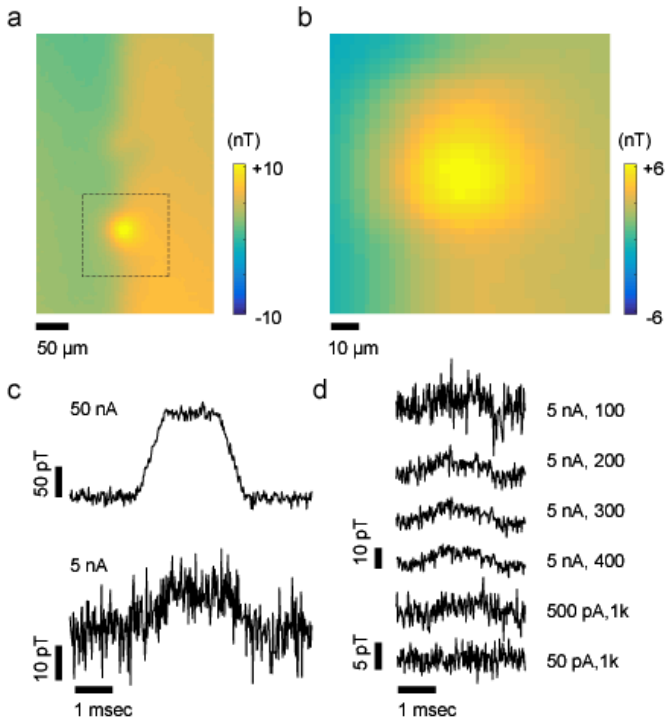

Figure 3.2. Magnetic field strength measurements of biologically relevant currents in nanofabricated coil. (a) High-resolution magnetic field map in response to large DC current (1 µA) **(b)** Close-up view of dashed square in (a). **(c)** Measurements of magnetic fields in response to 0.5 kHz, 20% duty cycle current injection. Traces shown have been averaged 50 times. **(d)** Magnetic field measurements of sub-nA currents, typical to neural activation. Device sensitivity of up to 500 pA yielding 5 pT fields has been observed. All measurements performed in phosphate buffer saline.

To verify the presence of a neuron-nanocoil junction able to transduce neural activity into a detectable magnetic field, we stimulated primary cortical neurons cultured on the device and

performed SQUID microscopy measurements of the resulting time-locked magnetic field in the center of the coil (Fig. 3.3). Prior to cell culture, devices were chemically functionalized with polyethyleneimine (PEI) to facilitate close adhesion to primary rat cortical neurons cultured on the device. The cells aggregated at protruding mushrooms of the interface pad (Fig. 3.3a, arrow). We stimulated the neurons electrically by an Ag/AgCl electrode in the bath for 1-2 msec at 1-3 mA (Fig 3.3b, red - stim). Neuronal field potential response was detected magnetically ~1 msec following sufficient stimulation (Fig. 3.3b, FP*)*. No response was detected following subthreshold stimulation pulses (Fig. 3.3b). The magnetic field amplitude recorded was ~0.05 nT 150 µm above the coil (Fig. 3.3b, rightmost trace) consistently between 8 individual stimulation sequences (Fig. 3.3c).

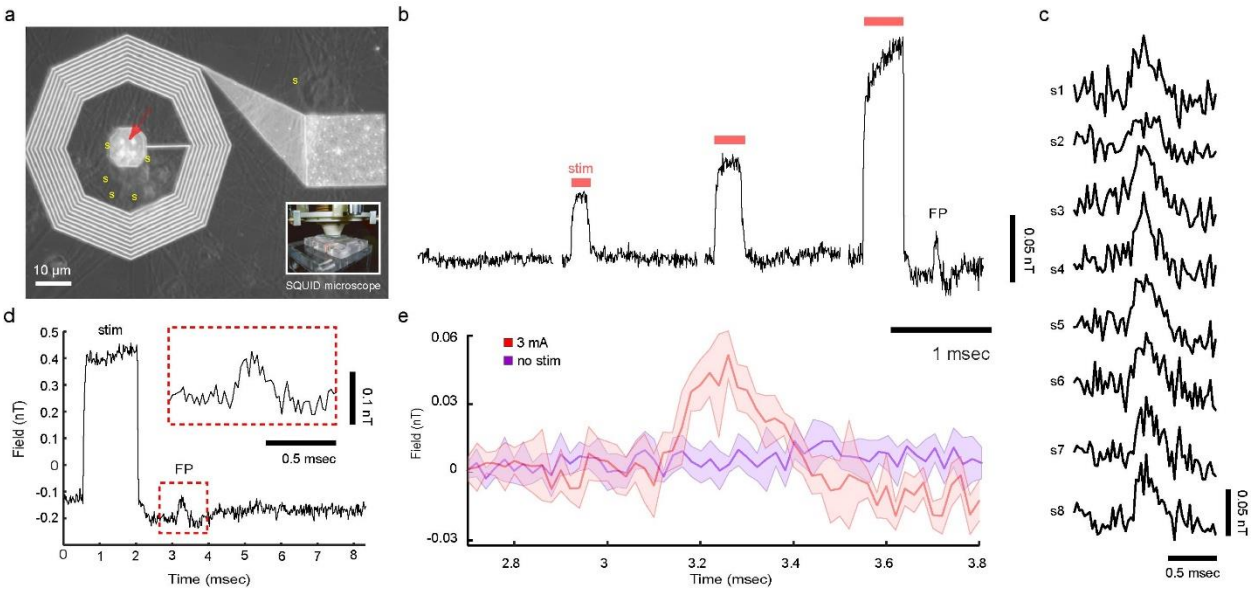

Figure 3.3. Magnetic field measurements of neural activity from several neurons cultured on nanocoil. (a) primary cortical neurons grown on nanocoil (s – somata aggregating at interface pad marked by red arrow, inset - SQUID microscope setup)). **(b)** neurons were stimulated (red) resulting in field potential (FP) detected magnetically by SQUID microscope at the center of the nanocoil. Shown are four epochs of increasing stimuli to a suprathreshold firing event (right hand side, FP). **(c)** Measurements from 8 separate stimulation trials. (**d**) FP of amplitudes up to 0.1 nT were detected. **(e)** Average responses (n=8) to stimulation (3 mA, red) vs no stim (purple).

Field potentials were detected magnetically with amplitudes of up to 0.1 nT (Fig. 3.3d). Response to 3 mA stimulation was in the form of spikes with average maximum amplitude of 0.083 ± 0.013 nT, 1.31 ± 0.06 msec following stimulus, rise time of 0.240 ± 0.100 msec, decay time of 0.180 ± 0.060 msec, and undershoot lasting 0.440 ± 0.520 msec (Fig. 3.3b-e, n=8). No spikes were recorded without stimulus, with a maximum recorded RMS amplitude of 0.038 ± 0.002 nT for each 0-10 msec epoch (Fig. 3.3b, right) similar to basal RMS noise level of 0.048 ± 0.017 nT without stimulation showing no significant difference (P=0.178).

The junction between neurons and our nanocoils operates similarly to a neuron-electrode junction but leverages the coil geometry for greatly enhancing the magnetic field induced by neuronal ionic fluctuations. Neuronal excitation manifests as mobilization of ionic charge that induces capacitive effects at the Au Helmholz double layer followed by mobilization of electrons in the electrode substrate[20]. Intrinsically minute and spatially constrained magnetic fields produced by the resulting current flow are summed cumulatively by the nanocoil design in proportion to its turn density. This prototype can be further optimized by maximizing turn density while maintaining minimal parasitic capacitance, an effort that would be limited only by the spatial resolution of current nano-scale lithography techniques relative to micro-scale diameter of living cells. Another important consequence of the nanocoil approach is the ability to redirect magnetic flux lines and enable measurements from regions that are not tangentially aligned with magnetic detectors. MEG is primarily sensitive to activity originating in cortical sulci rather than gyri, precluding comprehensive readouts[23]. Implanting dense nanocoil arrays in diverse regions and conformations can circumvent limitations inherent to MEG sensors and orientation dependency to B_1 fields inherent to MRI RF receive coils. Further, fabrication on flexible substrates[63] can

provide anatomical conformity with diverse brain structure and amplify signals that were thus far undetected.

Author contributions

AH and AJ designed the research. AH and JL performed device fabrication. AH and ED performed cortical cell cultures. AH and AL performed magnetic measurements. AH and IB analyzed the data, JP performed computational modelling. AH, IB, JP and AJ wrote the manuscript.

Acknowledgements

This research was funded by NIH grants K01 EB027184 to AH, and R01 NS76462, R01 DA038642, and U01 NS904051 to AJ.

Chapter 4: Microfabricated passive resonators as a next-generation modality for neural recording

***J. Phillips**, F. Wang, S. Bhatt, E. Masterson, A. Vareberg, I. Bok, T. Zhu, X. Ren, A. Hai;

Introduction

The previous chapters have explored the modelling, fabrication, and benchtop validation of single-cell scale nanofabricated inductors to transduce the action potentials of a single neuron into detectable magnetic signals. This chapter explores a microfabricated inductor-capacitor resonator at the radio frequency (RF) regime as a modality for revealing the coordinated activity of a small population of neurons through the ionic dynamics of neural activity. The extracellular concentration of potassium ($[K^+]_e$) can rise as much as 5 mM immediately around a population of neurons during activity, persisting for no more than 10 seconds [13–15]. The equilibrium extracellular ionic concentrations also reveal information about the overall brain state. $[K^+]_e$ rises and $[Mg^{2+}]_e$, $[Ca^{2+}]_e$, $[H^+]_e$, and extracellular volume fall during wakeful states, and vice versa during sleep or sedation [16].

The resonant frequency of an ideal inductor-capacitor (LC) resonator depends on the inductance and capacitance in the system, while the quality factor (Q) of the device depends on how freely charge can move through the resonator, determined by the resistance as well as any electrical short bypassing either of the critical components. The inductance is primarily determined by the geometry of the inductor. The capacitance of the system is determined by the geometry and dielectric of the capacitor, as well as the parasitic capacitance of the inductor, also determined by its geometry [148]. The resistance present in the system is often dominated by the parasitic series resistance of the inductor [149], but in thin film devices the sheet resistance of the metal layer can

contribute significantly. Sensors based on LC resonators commonly modulate one or more of these factors to create detectable changes in their resonance pattern.

Passive LC resonators were first proposed as biological sensors in 1967, using two flat, wound-wire inductors attached to the inside of two membranes on either side of a sealed capsule, such that changes in pressure would move the coils closer or farther apart, modulating both the stray capacitance and mutual inductance of the coils, and therefore the resonant frequency of the device [150]. This study also noted an apparent change in capacitance when implanted, which was more pronounced with thinner walls. When exposed to an aqueous ionic solution, such as saline, culture media, or cerebrospinal fluid, resonators can experience a load impedance with resistive and capacitive components, which can be used to modulate the resonant properties of the device. Martinez *et al.* [151] measured bacterial concentrations using just microfabricated inductor coils, based on the conductance of the bacteria shorting out the inductors and altering the measured inductance. Wu and Bhadra [152] proposed a planar LC resonator for measuring potassium ions specifically, connected to a planar ion-sensitive electrode in the solution being measured, with a sensing terminal coated in a potassium-selective membrane and an uncoated reference terminal. This membrane resulted in a primarily capacitive effect, modulating the resonant frequency in response to changes in potassium concentration. Bhatt *et al.* [12] utilized LC resonators for wireless interrogation and modulates their ability to resonate by shorting them using implanted ion-sensitive field-effect transistor (ISFET). This detunes the resonator- that is, lowers Q- in response to changing potassium concentrations. Hai *et al.*[11] used a similar transistor-based short to modulate Q and demonstrated that implanted resonators with transistor-based detuning can be read out using magnetic resonance imaging (MRI), where in the absence of stimulus the tuned resonator produces a halo on the reconstructed image, while a detuned resonator shorted out by its

transistor does not. The latter two cases sense neural activity purely through changes in Q, where the signals being measured do not affect the capacitance of the resonator.

We propose a method in which microfabricated LC resonators (microresonators) are in contact with the population of neurons of interest, and directly exposed to the ionic microenvironment around them. In this case, the load capacitance varies based on a property of the interaction between a polar liquid and a charged solid: the electrochemical double layer. Ions of opposite charge to the surface are attracted to it, and ions of the same charge as the surface are attracted to the first layer. This forms a dielectric layer between the surface and the ions in bulk solution, contributing to the load capacitance. Additionally, the concentration of dissolved ions determines the conductivity of the solution, and therefore the ability of the solution to short the device, which can be observed by its effect on Q. Pure water without dissolved ions insulates the device, and higher concentrations of ions increasingly short the device. Whereas Wu and Bhadra's electrode consisted of separate terminals in solution, the microresonator represents a complete circuit, meaning that in a conductive environment, for the device to short, charge must both leave and return to the device through the double layer (Fig 4.1a).

The effect of the ionic short is readily apparent in the macro scale model (Fig 4.1b). The S11 response of the stage-integrated interrogator antenna shows a decrease in the depth of the dip in normalized resonance from about -2.5 dB to -1 dB (and therefore a decrease in Q) as the concentration of PBS in the measured solution increases from pure water to 1x PBS. The resonant frequency also decreases slightly as ionic concentration increases, by about 1-2 MHz, within one measured frequency-step f. The decrease in the device's Q given an increase in [PBS] suggests that the resistive component of the load impedance has a large effect on the response of the millimeter-scale device, and the very slight shift to a lower resonant frequency implies that the

capacitive effect is also taking place. Here, we elucidate the direct interface between the microenvironment of a small population of neurons and our passive microfabricated LC resonant sensor.

Shifts in the resonant response of the microresonator quantified via the reflected power (S11) parameter by a vector network analyzer (VNA), from which we can infer shifts in Q and the capacitance of the resonator, will correlate with coordinated activity in the network of neurons cultured on the device, due to the changes in the ionic composition of the extracellular solution caused by cell activity. We have fabricated LC resonators consisting of a ten-turn, square, spiral planar inductor 1025 microns in diameter and a planar parallel-plate capacitor of varying size. The devices are microfabricated on wafers which are diced into 10 chips, each of which carries 12 devices with different capacitances, allowing us to test a wide range of designs with each experiment. While this design paves the way for wireless use, the goal of this study is to establish the feasibility of utilizing this effect to measure neural activity, and thus each resonator is connected to contact pads to connect to a VNA. The response of the devices to changing saline concentrations was characterized. Calcium-sensitive dye was used to record electrophysiological activity using a camera synchronized with the VNA, and the two modalities were compared.

Methods

Microfabrication

Patterns were made in KLayout and printed on transparencies by Fineline (10,160 DPI; Fineline Imaging, Colorado Springs, CO). 1 mm thick, 100 mm diameter Borofloat 33 wafers (University Wafer, South Boston, MA) were used as a substrate. APOL-LO 3204 negative photoresist (KemLab, Woburn, MA) was spun on using a 500 rpm, 10 second spread cycle, and 4000 rpm, 30

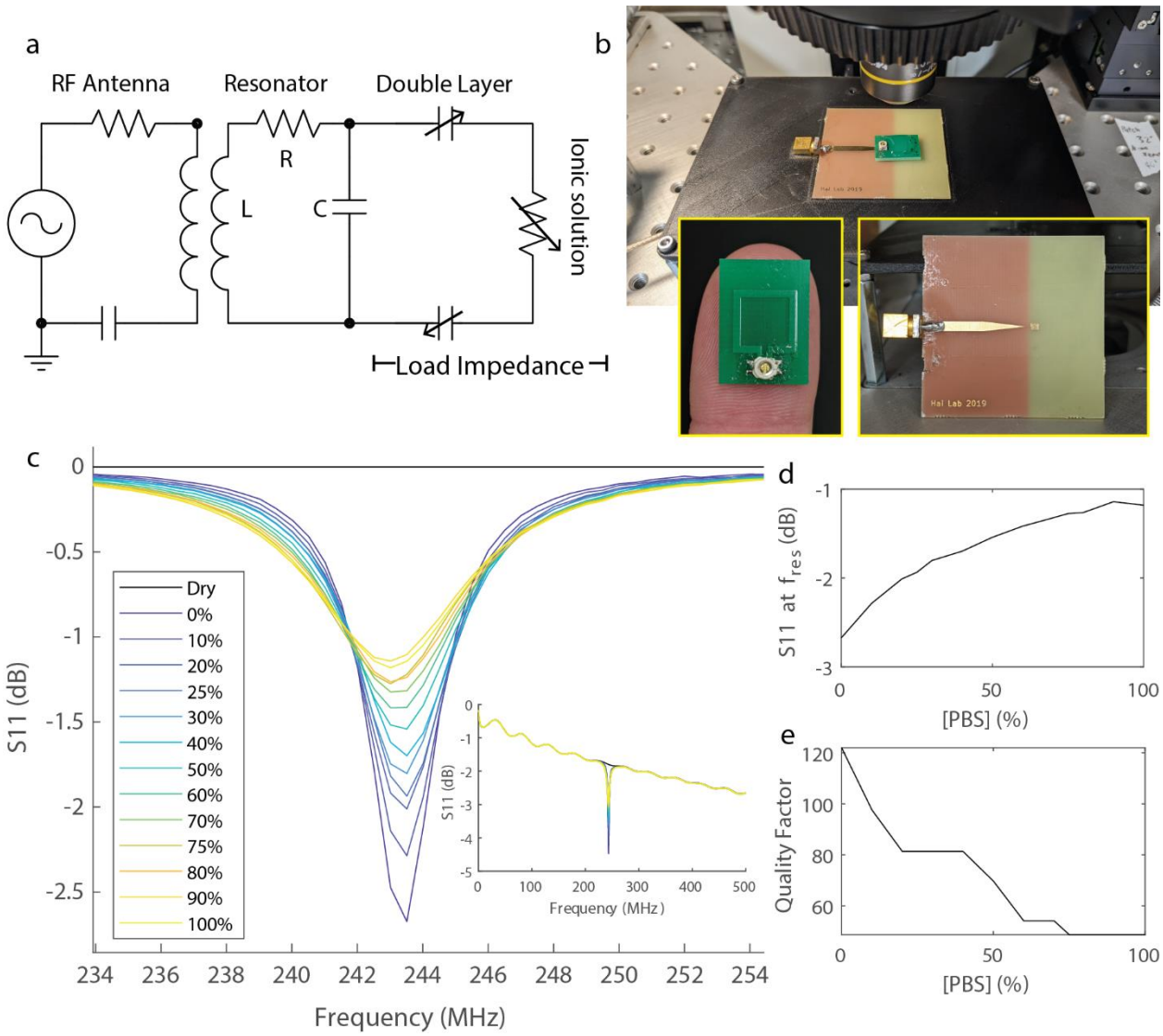

Figure 4.1: Theory and Scale Model. (a) Equivalent circuit diagram of a wireless LC resonator in ionic solution. **(b)** Microscope stage with integrated printed circuit board antenna. Left inset: Scale wireless resonator model. Right inset: Antenna stage. **(c)** Frequency response plot of scale model resonator with a droplet of ionic solution, ranging from water, or 0% 1x PBS, to 100% 1x PBS. Normalized to dry frequency response. Inset: Raw frequency responses across full frequency sweep. **(d)** S11 parameter value at resonance across all concentrations. **(e)** Quality factor of resonance dip across all concentrations.

second spin cycle followed by a 2 minute, 110°C soft bake. Patterns were transferred using a Suss MA-6 mask aligner (Süss Microtec SE, Garching, Germany) with a 15 second exposure at 10 mW/cm^2, for a total dose of 150 mJ/cm^2, followed by a post-exposure bake for 2 minutes at 110°C. Photoresist was developed by immersing in Microposit MF-321 (Kayaku Advanced Materials, Inc, Westborough, MA) for 60 seconds followed by a quench in deionized (DI) water, a rinse in DI water, and a final rise and dry in a wafer washer. The first layer of metal was deposited as 10 nm titanium, 100 nm gold, and another 10 nm titanium to facilitate adhesion with subsequent dielectric layers, using an electron beam metal evaporator (CHA-600, Telemark, Battle Ground, WA). Developed photoresist and excess metal were lifted off using Microposit Remover 1165 (Kayaku) for 10 minutes with ultrasonic pressure at power 8 (details). In the case of incomplete liftoff, the liftoff cycle was repeated until complete. After liftoff, wafers were rinsed in isopropyl alcohol (IPA) and DI water before being washed and dried in a wafer wash. Plasma-enhanced chemical vapor deposition (PECVD) was used to deposit approximately 100 nm of silicon nitride (PECVD machine, 850 mT deposition pressure, 420 Standard Cubic Centimeters per Minute N_2O [2000], 500 SCCM 2% Silane [1000], 80 SCCM 5% NH_3 [200], 26 W RF power). Photolithography was repeated as described above to pattern vias through the dielectric. Reactive ion etching (RIE) (RIE Machine; 40 mT etch pressure, 45 SCCM CF_4 [100], 5 SCCM O_2 [100], 100 W RF Power) was used to etch the vias. Complete etching was confirmed using a Tencor stylus profilometer (KLA Corporation, Milpitas, CA), and photoresist was removed as above. The final layer of metal, 10 nm titanium followed by 300 nm gold, was patterned and applied using photolithography, metal deposition, and liftoff as above. Devices were tested for electrical continuity between the ground and test pads before being diced using a Disco dicing saw (Disco Hi-Tec America, San Jose, CA). Individual chips were then bonded to 35 mm polystyrene cell

culture dishes with laser-cut holes to leave the devices exposed, using Kwik-Sil low toxicity silicone adhesive (World Precision Instruments, Sarasota, FL).

Probe and Microscopy Station

For all recordings, the VNA (R60, Copper Mountain Technologies, Indianapolis, IN) is calibrated using a calibration kit (S911T, Copper Mountain Technologies) in short, open, and load configurations. The open calibration is repeated when attached to wired contact probes before making any contact. All calibrations and measurements are made in a faraday cage containing an epifluorescent microscope. For scale model testing, VNA recordings are taken wirelessly using a custom PCB antenna placed into a custom microscope stage and connected to the VNA via an SMA cable (Fig. 4.1). For reading from microfabricated resonators, recordings are taken through wired connections on a probe station mounted around the stage of the epifluorescent microscope. Two independently moveable probes are connected to the VNA via a single SMA cable, the signal probe through the center and the ground through the shield (Fig. 4.3). For direct measurements from coils, the signal probe touches a connection pad connected to a single coil, while the ground probe connects to a common ground pad. Upon time-series acquisition, the microscope camera sends a trigger signal synchronized to image acquisition, which triggers the VNA to record a 201-point linearly spaced sweep within frequency ranges of interest. Camera and VNA are recorded for 60 seconds with a sampling rate of 10 Hz.

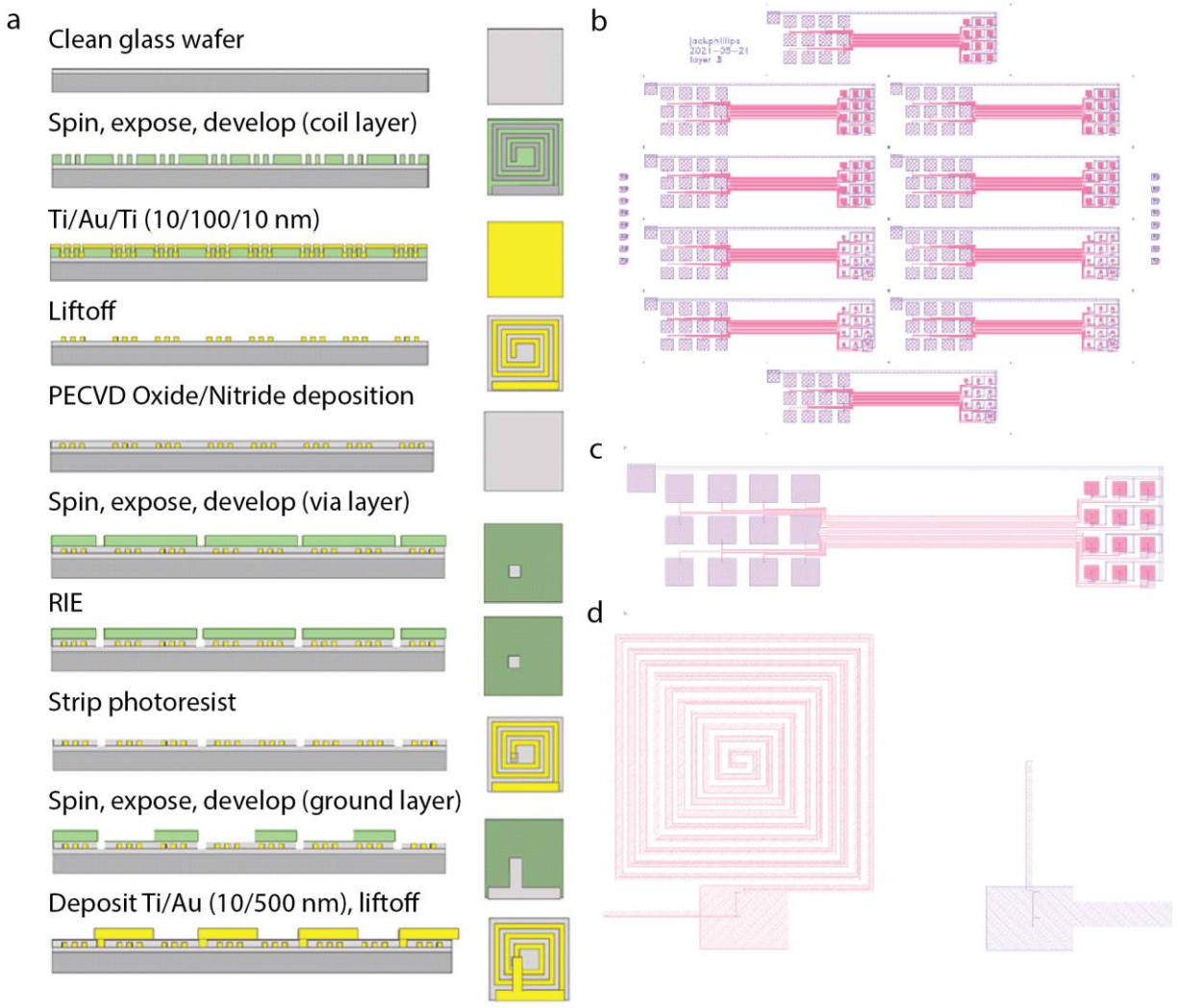

Figure 4.2: Fabrication and Layout (a) Fabrication scheme for microresonators. Note that the coil and ground layer photolithography steps are interchangeable. **(b)** Full wafer pattern, with both metal layers and the via layer. **(c)** Pattern for a single die with all three layers. **(d)** Coil and ground layers for a single resonator geometry.

Tables 4.1-4.4: Capacitor Geometries and Resulting Resonant Frequencies

Geometry	Area (mm^2)	C (pF)	Calculated F_{res} (MHz)	Approximate Measured F_{res} (MHz)
1	0.0441	7.99	256.35	205
2	0.15	27.17	139.00	105
3	0.35	63.39	91.00	60
4	0.0625	11.32	215.34	190
5	0.2	36.22	120.38	90
6	0.4	72.44	85.12	60
7	0.0875	15.85	181.99	170
8	0.25	45.28	107.67	80
9	0.45	81.50	80.25	60
10	0.125	22.64	152.27	100
11	0.3	54.33	98.29	70
12	0.6	108.66	69.50	50

5-turn	Area (mm^2)	C (pF)	Calculated F_{res} (MHz)
1	0.09	16.30	462.82
2	0.25	45.28	277.69
3	0.3025	54.78	252.45
4	0.1225	22.19	396.71
5	0.36	65.20	231.41
6	0.81	146.69	154.27
7	0.16	28.98	347.12
8	0.49	88.74	198.35
9	0.999	180.92	138.92
10	0.2025	36.67	308.55
11	0.64	115.91	173.56
12	2.1125	382.58	95.53

Dielectric Thickness (nm)	220
Dielectric Constant	4.5
Permittivity of Free Space (ε_0)	8.85E-12

Approximation	10-Turn Coil Calculated Inductance (nH)	5-Turn Coil Calculated Inductance (nH)
Modified Wheeler	47.92	7.201
Current Sheet	49.443	7.321
Monomial Fit	47.421	7.243
Average	48.26133333	7.255

Ionic Testing

A millimeter-scale resonator consisting of a single-turn PCB inductor (ID 6.9 mm, OD 9.3 mm, turn width 1.2 mm) and a 30 pF capacitor was measured wirelessly with a PCB antenna (Fig. 4.1b). Calculated inductance of this PCB coil was 17 nH [132], resulting in a calculated resonant frequency of 223 MHz and measured resonant frequency of 243 MHz. This millimeter-scale resonator was tested for its response to the presence of ionic solutions using DI water and 1x PBS (Invitrogen) mixed to PBS concentrations of 0x, 0.1x, 0.2x, 0.25x, 0.3x, 0.4x, 0.5x, 0.6x, 0.7x, 0.75x, 0.8x, 0.9x, and 1.0x (0%-100%).

Microfabricated resonators on chips bonded to culture dishes were tested using a similar decade sweep of concentrations to characterize individual coils deeply, and using a quartile sweep of concentrations (0x, 0.25x, 0.5x, 0.75x, 1.0x PBS) to characterize a coil of each geometry. To minimize motion of the device dishes relative to the probes, fluid was changed without fully draining the dish. 2 mL of either DI water or 1x PBS were added to device dishes for the first measurement, then increasing volumes were replaced with 1x PBS or DI water, respectively, for subsequent measurements. For each device, this sweep was performed with both increasing and decreasing concentrations of PBS. VNA acquisitions for ionic testing of microresonators were taken as 6- or 60-second, 10 Hz time series to enable averaging across time to reduce noise, and to capture a representative sample of noise without changes in ionic concentration.

On one chip (D4), dielectric was scraped away over the encapsulated ground-side path next to microresonators to allow for measurements without the effect of the traces across the length of the chip. Measurements were taken from device 7 on this chip, and from device 7 on another chip from the measurement pads, with 5 µL droplets of 1x PBS and DI water. The device was dried using a lens wipe between measurements.

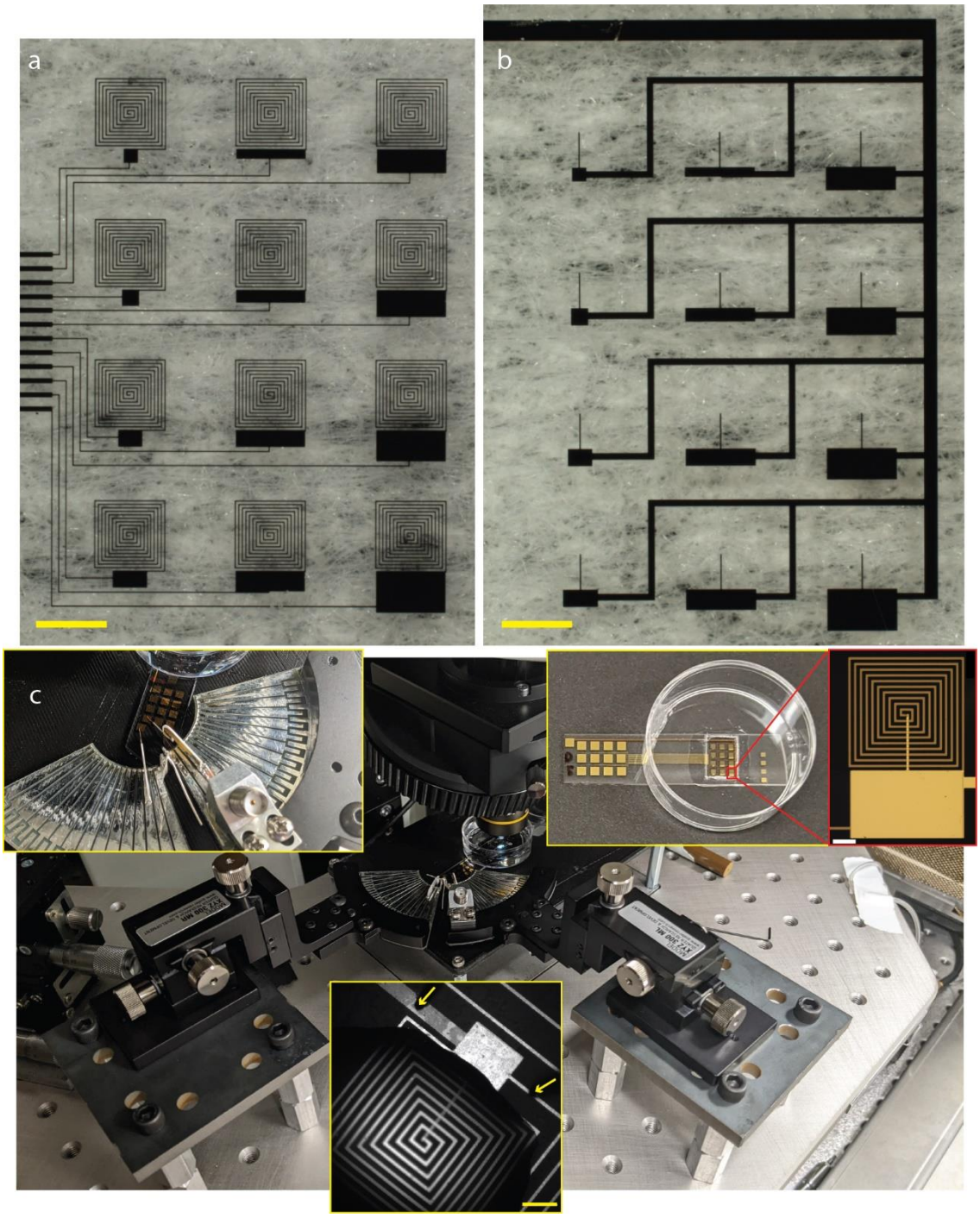

Figure 4.3: Assembly and Radio Frequency Measurement Probes. (a) Complete coil layer, fabricated as the bottom layer. SB = 1mm. **(b)** Complete ground layer, fabricated as the first layer. SB = 1mm. **(c)** Radio frequency (RF) measurement setup. Magnetic-based micromanipulators mounted on steel platforms around the microscope stage hold custom-made RF probes. Top left

inset: Probe tips are independently moveable to make contact with measurement and common ground pads. Top right inset: Completed chip attached to cell culture dish with bottom window using silicone adhesive, with micrograph of coil geometry 12 highlighted. Bottom inset: Micrograph from measuring ionic resonant response directly next to coil, with probe tips highlighted by yellow arrows. Both SB = 200 μm.

Cell Culture

Primary cortical rat neurons (Gibco, Frederick, MD, catalog A10840-01) were cultured as described in Chapter 1. Briefly, glass coverslips or assembled device dishes were sterilized with ethanol for 15 minutes, with device dish sterilization performed under UV light. Culture surfaces were prepared with a 50 µL (coverslip) or 100 µL (device) droplet of sterile filtered aqueous 0.1 mg/mL poly-d-lysine (PDL, Gibco A38904-01) and 4 ug/mL laminin (Gibco 23017-015). 100,000 cells were seeded per culture in plating media (Neurobasal Plus, Gibco A3582901; 10% FBS Gibco 10437010; 1x GlutaMAX, Gibco 35050-061), cultures were incubated for 4 hours, and media was changed to 3 mL of maintenance media (Neurobasal Plus, 1x B27 Plus Gibco A3582801, 1x GlutaMAX). Media changes were performed every 3-4 days (Mondays and Fridays), alternating between half (1.5 mL) and all (3 mL) of the volume. Between cultures, device culture surfaces were cleaned with Tergazyme enzymatic detergent (Alconox, White Plains, NY) per the manufacturer's instructions.

Calcium Imaging

Fluo-4 AM calcium sensitive dye (Invitrogen, F14201) was dissolved in 1% Pluronic F-127 surfactant (Invitrogen, P3000MP) in dimethyl sulfoxide (DMSO) at a concentration of 1 mg/mL Stock solution was added to maintenance media at a final concentration of 10 µg/mL in loading solution. Device cultures were stained with 200 µL of loading solution for 20 minutes at room temperature, loading solution was replaced with maintenance media, and cultures were left in the incubator for 20 minutes to hydrolyze the AM esters. Cultures were imaged within two hours after hydrolysis was complete at a frame rate of 10 Hz, with simultaneous VNA measurement. Seizurgenic 4-aminopyridine (4-AP) was added to cultures at a final concentration of 200 µM after initial imaging, and loaded cultures were incubated for 20 minutes before further imaging.

Analysis

Calcium imaging data was analyzed using MATLAB. Briefly, image sequences were reduced to a mean-intensity projection and segmented using a watershed algorithm [153]. Mean intensities of cell bodies are analyzed for local maxima above a threshold prominence ($1/60^{th}$ of the most prominent maximum), which are recorded on raster plots. Per-cell mean intensity is normalized to $\Delta F/F_{0,\ then}$ the normalized intensities are averaged for per-culture intensities, yielding a single time-dependent trace for comparison to the time-dependent VNA signal.

VNA data is plotted in the frequency domain to verify that data was collected as expected. Abnormal frequency responses, compared to the responses obtained in ionic testing, suggest faulty cables, bad ground contact, or other issues with recording. To test the capacitive effect on resonant frequency, shifts in the frequency at which S11 is at a minimum were tracked over time. To test the resistive effect on Q, shifts in the S11 parameter at single frequencies either above or below the resonant frequency were tracked. VNA and intensity traces are de-trended by subtracting a 6^{th}-order polynomial fit of the signal. The two signals are cross-correlated, and correlation coefficients greater than two standard errors from 0 are taken to be significant [154].

Results

Ionic Characterization

For microresonators, the decade-increment PBS experiment showed that under a certain cutoff frequency, the shifts in the frequency response vary monotonically with changing PBS concentration (Figure 4.4a-b). From approximately 0-50 MHz on the resonator tested (resonator geometry 6), traces can be clearly distinguished. We refer to this frequency range as the “region of discriminability,” where a measurement at a single frequency would theoretically allow wired measurements to reveal fine changes in ionic concentration. This appears to be an effect of Q

varying with the conductivity of the solution. Notably, the reflected power at the measured resonance frequency, in this case approximately 60 MHz, changes very little. The effect on Q primarily arises from variation in the response from frequencies below resonance. The capacitive effect is weakly present, as the measured resonant frequency shifts slightly lower with higher concentrations of PBS. There is an artifact present in all traces at approximately 120 MHz, likely due to the RF probes configuration.

Measurements of 5 µL droplets on coils with geometry 7 from the connection pads (fig. 4.4c) and from immediately next to the coil (fig. 4.4d) also show clear separation between the water and PBS measurements below 100 MHz and 200 MHz, respectively. This strengthens the conclusion that the effect observed above is due to the microresonator-solution interaction, rather than an interaction between the solution and other exposed conductive paths.

In the quartile-increment PBS experiment across all device geometries, each geometry shows a different response to changing ionic concentration (Fig 4.5). Coils 1,4, and 7, with the smallest capacitors, show notable shifts in their resonant frequency within a band above the 120 MHz artifact. As discussed above, this points to a change in load capacitance, consistent with changes in the electrical double layer. This experiment also enables us to identify the region of discriminability for each device (Fig 4.6), occupying a band from 1 MHz, the lowest frequency measured, up to the resonant frequency. Here, again, the smallest capacitor geometries show the widest ranges of discriminability. Both the capacitive effect on resonant frequency and the resistive effect on Q suggest avenues for recording neuronal activity through microresonators.

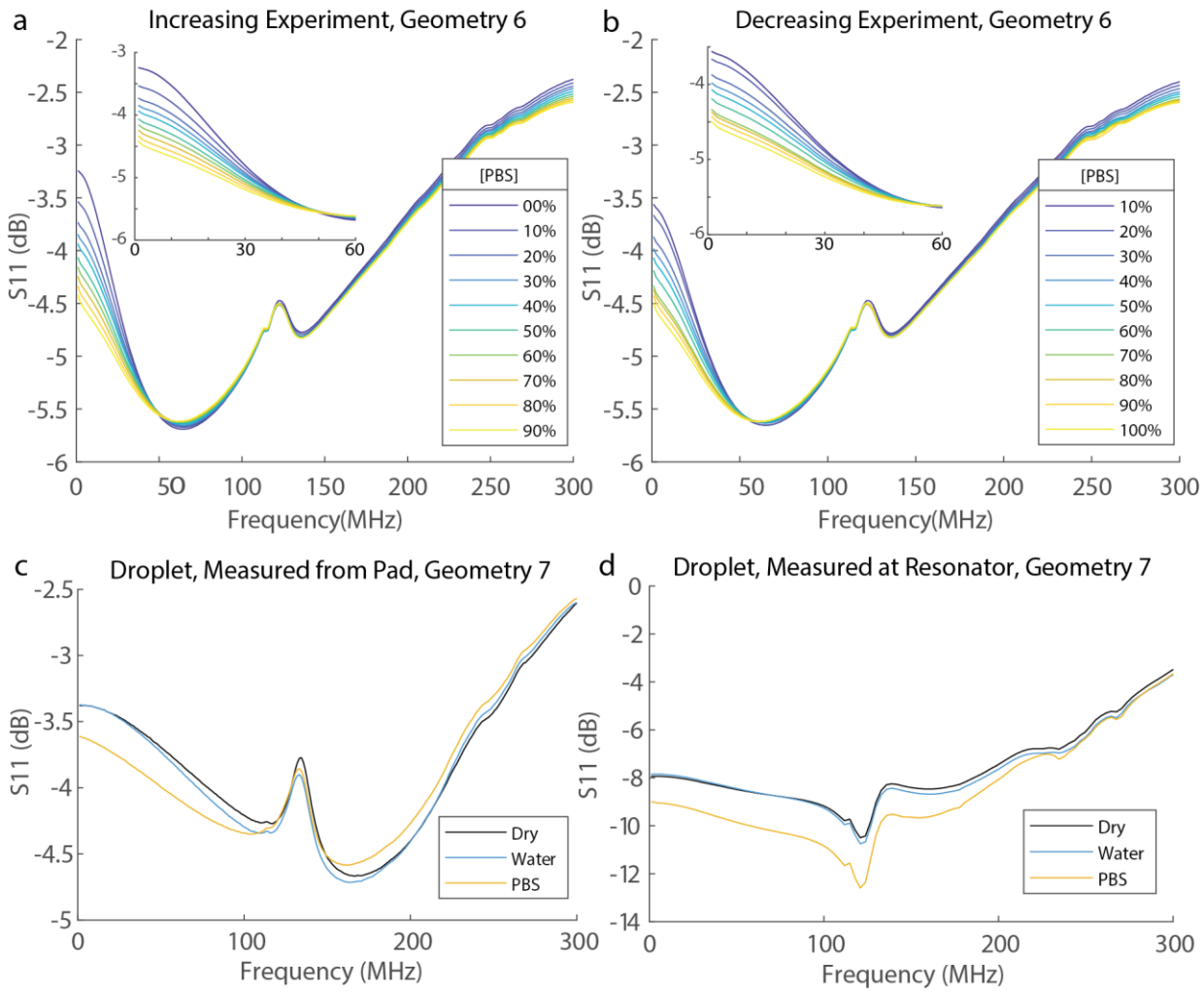

Figure 4.4: Ionic Test Results, Decade Sweep and Droplet Test. (a) Frequency response for geometry 6 with the cell culture dish filled with solution. Concentration was increased from 0% PBS (water) to 90% 1x PBS in increments of 10% without removing the full volume. Inset: Region of discriminability, at frequencies below resonance. **(b)** Frequency response from the same device, with concentration decreased from 100% to 10% 1x PBS. Inset: Region of discriminability. **(c)** Frequency response of geometry 7 with a 5 µL droplet of solution applied directly to the coil. **(d)** Frequency response of geometry 7 measured from immediately next to resonator (Fig. 4.3c) with 5 µL droplet applied directly to the coil.

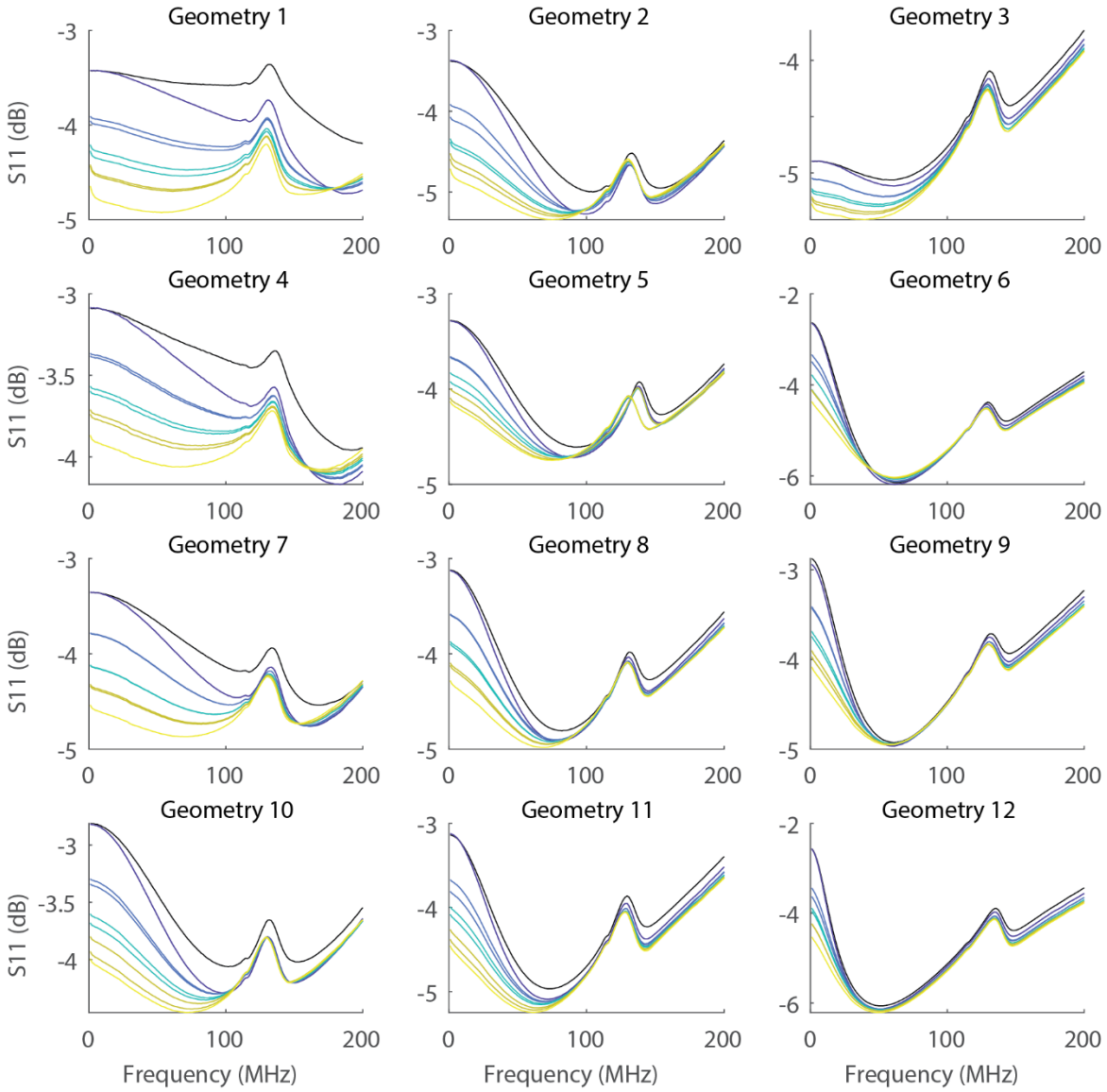

Capacitance (pF)		
7.99	27.17	63.39
11.32	36.22	72.44
15.85	45.28	81.50
22.64	54.33	108.66

Figure 4.5: Ionic Test Results, Quartile Sweep Across Chip. Frequency responses for each of the 12 geometries. Frequency band is uniform across map from 0 to 200 MHz. Calculated capacitance for each geometry is listed in table below; C increases from top to bottom and left to right, with a corresponding shift to lower resonant frequency.

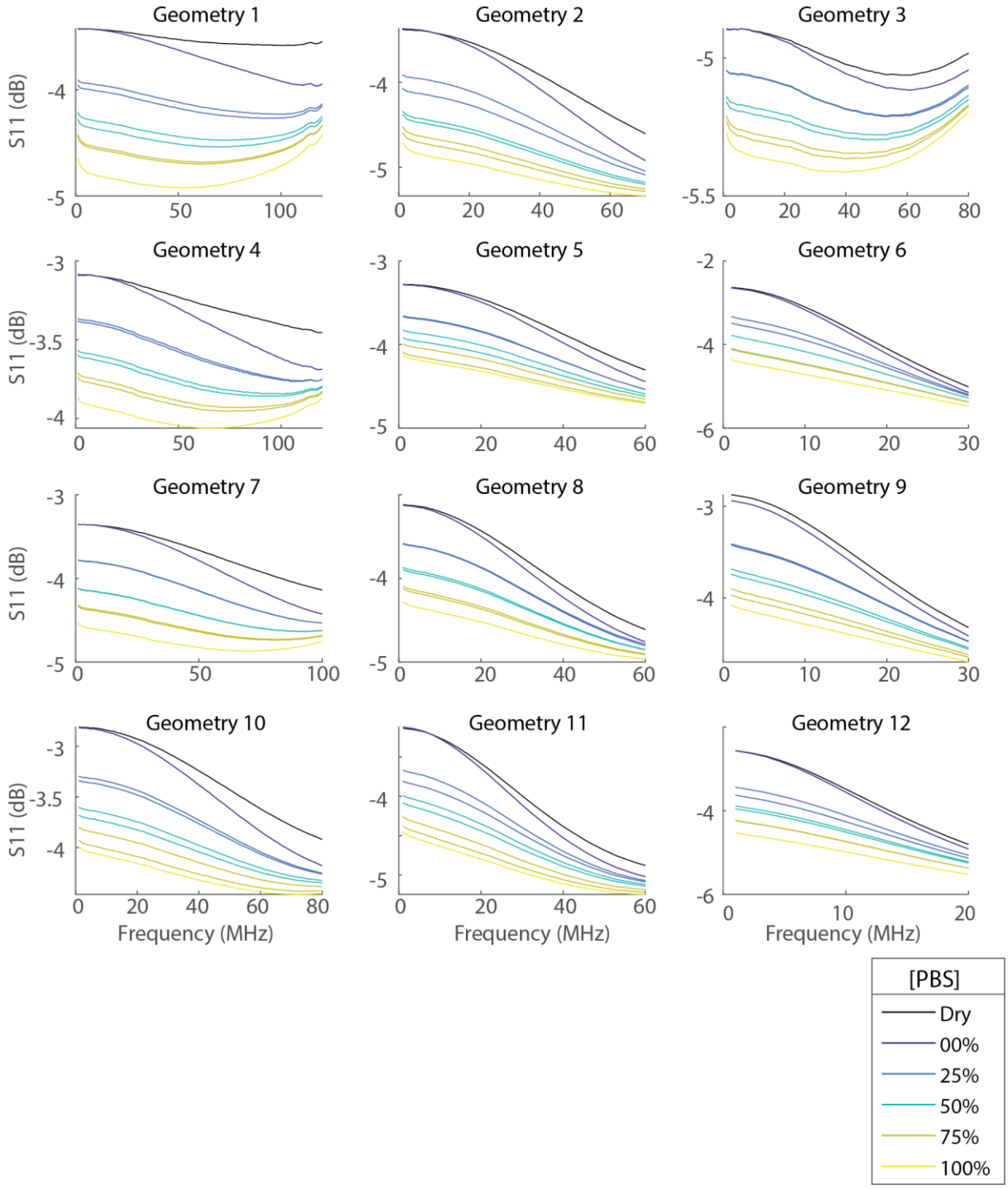

Figure 4.6: Ionic Test Results, Quartile Sweep Across Chip. Frequency responses for each of the 12 geometries. Frequency band varies across map to highlight region of discriminability, at frequencies below resonance.

Biocompatibility and Calcium Activity

Primary rat cortical neuron cultures were healthy (Fig. 4.7) and electrically active when grown on microresonators. Spontaneous coordinated network activity was noted after 14 days in vitro (DIV) via calcium imaging. The rate of network firing increased after the addition of 4-AP (Fig 4.8).

VNA Detection of Cellular Activity

VNA recordings were taken simultaneously with calcium recordings within frequency bands that encompass the range of resonant frequencies recorded for each geometry during ionic testing. Analysis was performed as described above, using four different signals extracted from VNA data. Two of these signals were chosen to test for correlations with capacitive effects: The resonant frequency over time, defined as the frequency at which the S11 parameter is at a minimum for each frame, and the ratio between the S11 parameters over time for the highest and lowest frequencies within that range of resonant frequencies. The other two were chosen to test for resistive effects: The S11 parameter over time for the highest frequency measured, and for the lowest frequency measured. The ratio of S11 at the two ends of the range of resonant frequencies had the strongest correlation between the two modalities, with a maximum correlation coefficient of 0.146 between the VNA signal and the calcium signal 1.1 seconds later. The strongest inverse correlation was -0.115 between the VNA signal and the calcium signal 6.1 seconds later. For recordings of inactive cultures, this cross-correlation has no significant lags within a +/- 10 second window, with correlation coefficients ranging from -0.029 to 0.033.

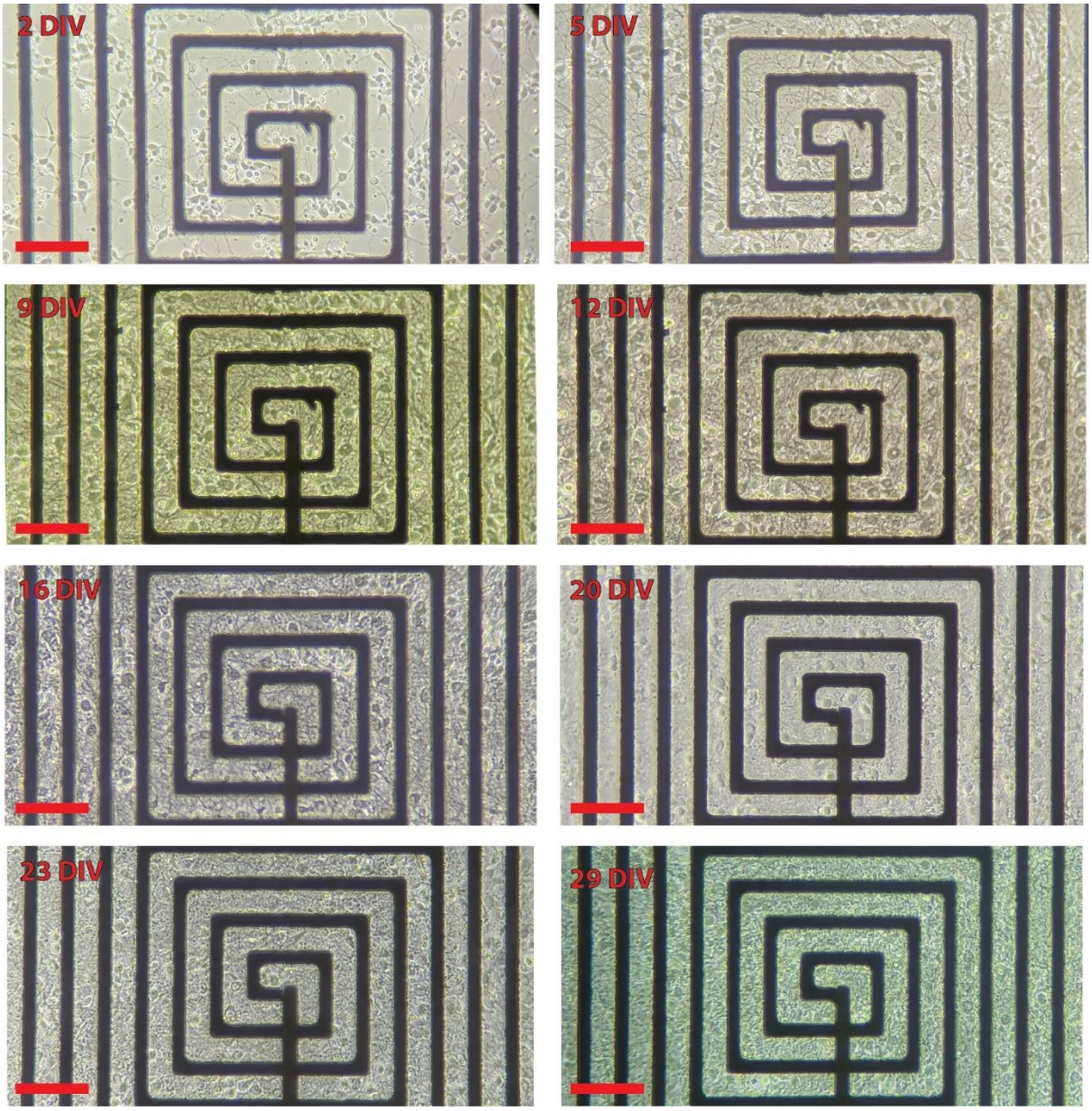

Figure 4.7: Biocompatibility. Phase-contrast micrographs showing neural culture development at 2,5,9,12,16,20,23, and 29 days in vitro (DIV). Acquired on inverted microscope, 10x or 20x objective, using Pixel 6a. All micrographs cropped to center of coil. SB = 100 μm.

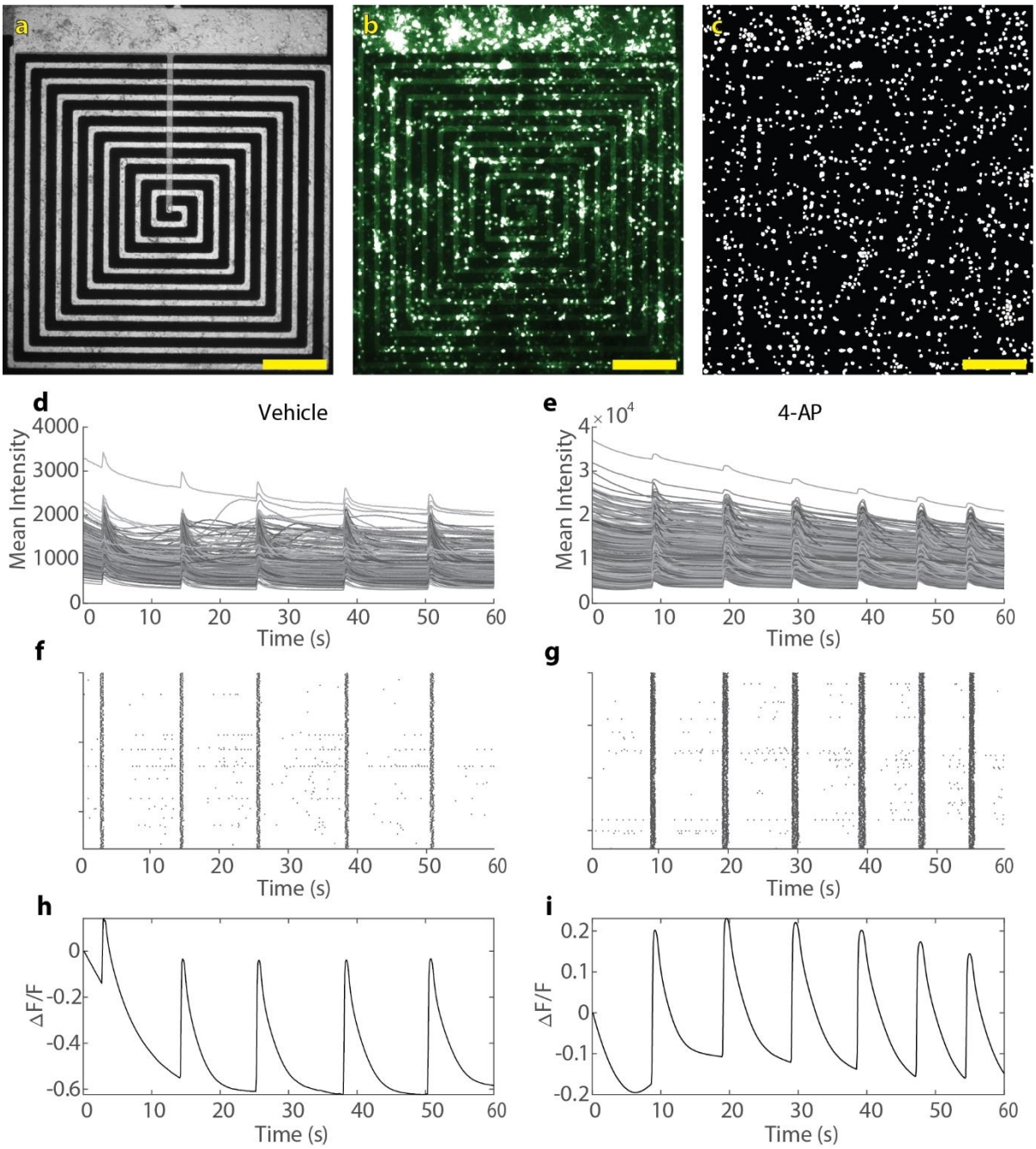

Figure 4.8: Calcium Analysis Results. (a) Differential interference contrast (DIC) micrograph of a microresonator immediately before simultaneous recording. SB = 200 μm. **(b)** Maximum intensity projection of all calcium timelapse images, used to segment individual cells. SB = 200 μm. **(c)** Binary mask of segmented cells, with each cell represented by a white region of interest (ROI). SB = 200 μm. **(d-e)** Mean intensity traces without normalization from the culture shown

above before (d) and after (e) addition of 4-AP. Each trace represents the mean intensity of a single ROI in binary mask (c). **(f-g)** Rasters of the same datasets. Each row represents a single ROI in binary mask (c), and each point represents a local maximum in the mean intensity trace. **(h-i)** Per-image normalized mean intensity traces of the same datasets, used for comparison to VNA data. Per-cell mean intensity traces are normalized to change in fluorescence over initial fluorescence ($\Delta F/F$) and then averaged together.

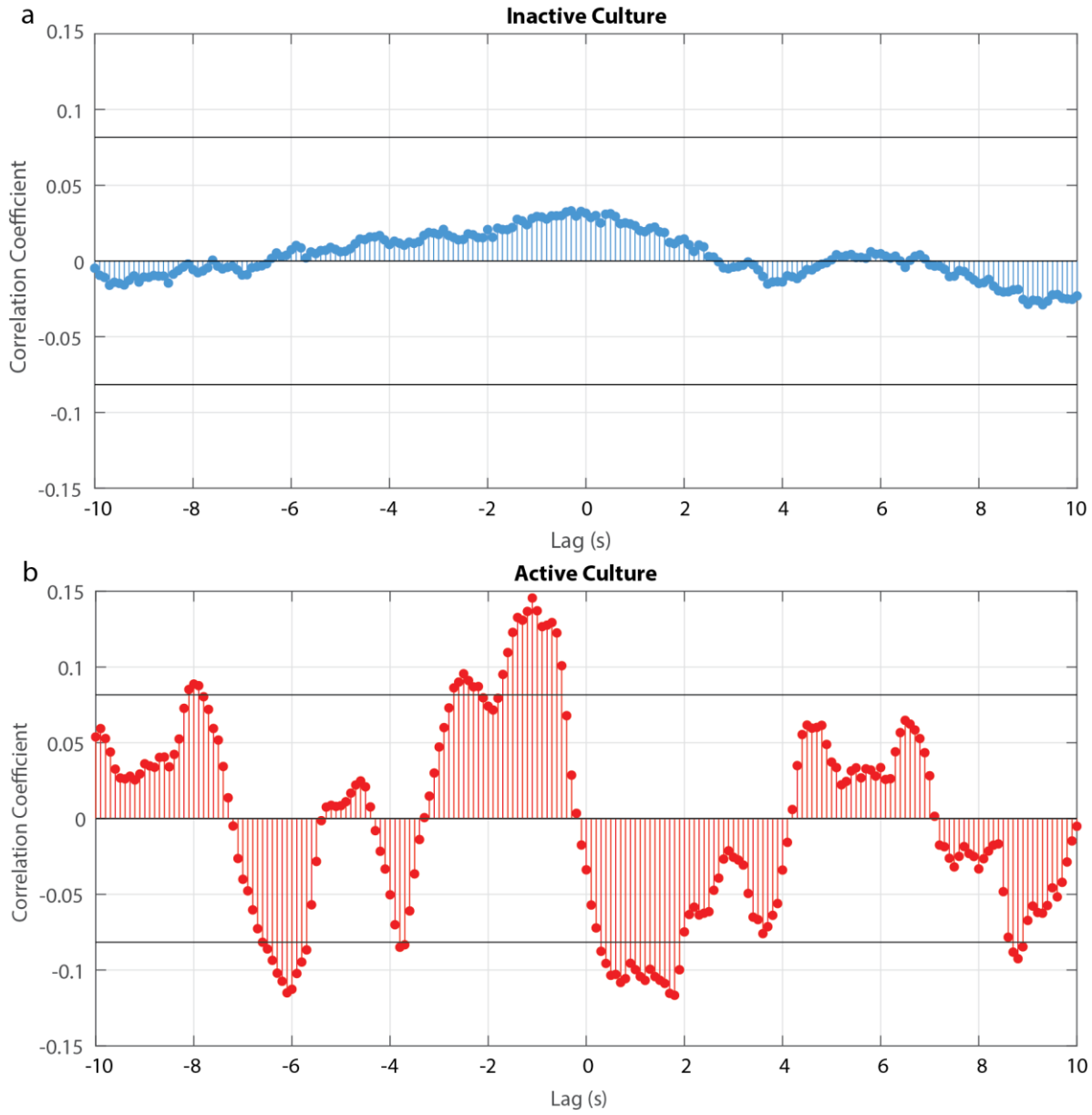

Figure 4.9: Cross-Correlations Between Calcium and VNA. Negative lags represent correlations between calcium per-image mean intensity trace and preceding VNA activity. 95% confidence interval marked with black lines, representing 2 SE of sample cross-correlation [154]. **(a)** Cross-correlation for recordings of an inactive culture, without coordinated network activity. Strongest direct and inverse correlation coefficients are .033 and -.029. **(b)** Cross-correlation for an active culture. Strongest direct correlation coefficient = 0.146 at lag = -1.1 s. Strongest inverse correlation coefficients are -0.115 at lag = -6.1 s and -0.117 at lag = +1.8 s.

Conclusion

Nanocoils

My PhD work focused on the development of novel electromagnetic methods for detecting brain activity. In this dissertation, I presented my model of the magnetic response of the nanocoil, a passive nanofabricated planar inductor which transduces the action potential of an attached neuron into a magnetic field. I found that this device outputs a volumetric magnetic signal approximately 250 times greater than that of a neural process experiencing the same current. I also optimized the geometry of the device to maximize the signal amplification and modelled the response of the device when fabricated on common substrates and found that common high-resistivity and biocompatible flexible substrates do not impede this amplification. I specifically explored the compatibility of the nanocoil design with the flexible substrates polyimide and parylene. These materials have been used in previous neural interface designs for their biocompatibility and flexibility, which allows them to conform to the surface of the cortex and reduces their mechanical effect on the brain [1,155–157]. However, these materials can face difficulties with regulatory approval and supply chains for medical-grade materials, and thus further characterization and process development using PDMS as the final substrate for *in vivo* use is an important next step in developing this technology.

I further presented the fabrication of this device using electron-beam lithography, including modelled and experimental data showing novel methods for fabricating high turn-density coils. I also presented simulated and experimental data showing the relationship between device geometry and resonant and operational properties. Finally, I presented two different methods for measuring from nanocoils, nitrogen-vacancy (NV) magnetometry and superconducting quantum interference

device (SQUID) magnetometry. The former represents the potential for *in vitro* electro-magneto-optical experiments in 2D and, with some development, 3D cultures. The latter is a common method for clinical magnetometry and represents the potential for *in vivo* applications and clinical translation. Importantly, the nanocoil produces a directed magnetic field, in contrast with those created by individual neurites, and could allow for magnetometric measurements outside of areas where dendrites are aligned and able to sum their fields.

To interface with individual neurons, the nanocoil is designed to be encapsulated in dielectric with only the attachment feature on the central pad and the entire ground pad left exposed, ensuring that the transduced signal originates from the potential difference between a tight coupling with the attached cell and the local field potential experienced by the entire device. These previously described attachment features, gold mushroom-shaped microelectrodes (GMμEs), consist of gold mushroom-shaped spines approximately 1.5 microns tall, with a 1.8 micron wide, 500 nm tall cap and an 850 nm wide, 1 micron tall stalk [47,145]. GMμEs are functionalized with integrins and RGD peptides to encourage phagocytosis of the cap, a tight junction held in place with actin rings, with accumulation of ion channels and mitochondria at the junction. This forms an electrical seal on the order of 100 MΩ with a junctional membrane resistance on the order of 10-100 MΩ [48]. Action potentials from the attached neuron represent the largest and fastest changes in voltage, and therefore the most likely electrophysiological activity to be transduced. While these are most prominent in the axon, and while the dendritic-spine-like morphology of the GMμE may select for axonal attachments, backpropagation of action potentials into any attached dendrites could also provide a signal capable of generating a magnetic response [158,159].

Microresonators

I then presented the development of novel, passive, resonant devices which respond to local changes in ionic concentration associated with coordinated neural activity. I developed the theory for these probes using a large, millimeter-scale model and wireless recordings of their response to ionic solutions of different concentrations. I then fabricated these devices with wired connections to demonstrate their passive ionic sensing capabilities *in vitro*. I characterized these devices with further ionic response experiments, and found that depending on device geometry, capacitive and resistive effects of the solution modulate the resonant frequency and quality factor, respectively. I then cultured healthy, electrically active neurons on these devices and simultaneously recorded them via custom-made RF probes and via an optical indicator of cellular calcium concentration, an ionic marker of electrical activity. I found that the two signals are correlated when cultures are electrically mature with coordinated network activity and are uncorrelated before the cultures reach electrical maturity. This represents a significant advancement in electromagnetic biological sensors and lays the groundwork for passive, wireless probes for measuring neural activity. Future iterations of these devices could be fabricated with a much thicker coil layer, significantly reducing the resistivity of the path and allowing for high-Q wireless measurements, and then implanted for use in MRI, or for use with a purpose-built antenna probing multiple frequencies.

Recording Volume

Traditional electrophysiology, utilizing electrical recordings from wired electrodes, generates a signal that is the sum of individually distinguishable single units within 50 microns of the electrode- approximately 100 neurons in the case of a point recording from a tetrode- as well as less distinguishable activity from groups of neurons within 140 microns- approximately 1000 neurons in the case of a point recording [160]. Both the nanocoil and the microresonator are

designed to respond to neurons and populations in close proximity to the sensor. The nanocoil is designed to interface with single neurons by way of its central attachment features. The microresonator responds to changes in the bulk ionic concentration, rather than changes in potential caused by the relative concentrations of positive and negative ions. Therefore, the sensing distance of the microresonator is much more localized to the population immediately adjacent to the sensor. *In vitro,* these ionic changes are less affected by the bulk culture solution due to the cell monolayer forming a rudimentary extracellular matrix, localizing concentrations between the cells and sensor and within the matrix. *In vivo,* where cells are not grown directly attached to the device, shifts in ionic concentration do not have bulk culture solution to potentially dilute the effect, and face diffusive effects from a three-dimensional volume of tissue near the sensor. The threshold of detection could be improved with the use of ion-sensitive functionalization of the device [152], a route already being explored for resonant neural sensors [12].

Because the microresonator represents a novel modality for extracting information about the activity arising in a population of neurons, we cannot necessarily rely on conventional spike-sorting techniques to characterize the response. The simultaneous calcium/RF datasets presented in chapter 4 were reduced to one-dimensional time-dependent signals to allow for correlation between the signals. However, the calcium data contains information about individual neurons with regular activity at much higher frequencies than the slow network spikes (Fig 4.8 f,g) which may also correlate with certain characteristic features in the RF recordings. Future *in vitro* work could make use of voltage-sensitive dye for additional optical-RF comparisons, or patch clamp or other electrode-based recordings to further elucidate the connection between neural activity and the microresonator response. The nanocoil response, by contrast, was predicted (Fig. 1.3 c,d) and shown (Fig 3.3 b-e) to follow the biphasic currents of an action potential closely.

In Vivo Directions

In chronic implants inserted into the cortex, the process of placing the device can provoke an inflammatory glial response, resulting in a diffusion barrier that could hinder ionic signal from reaching the device. Thus, subdural implantation without damaging the cortical tissue, much like the placement of ECoG devices, would likely provide the best access to ionic currents generated by neural processing in the upper layers of the cortex. The abundance of axons and dendrites in layer 1 [161] also provides a good target for nanocoils. In both cases, this would align the inductor of the device with the skull, allowing ease of detection.

Subdural implantation also offers the opportunity to place artificial *dura* materials [162,163] to encourage the *dura mater* to heal over the device and anchor it in place. Anchoring microresonators and nanocoils underneath the *dura* would reduce motion artifacts and implant migration, though the self-contained nature of wireless implants already provides excellent protection against motion artifacts. This is particularly true for the nanocoil, which forms a physical connection with the target neuron and does not rely on the capacitive effects of the ionic double layer. The primary benefit of these technologies, however, is that both microresonators and nanocoils are entirely passive devices, and thus have no onboard power sources which require regular replacement, no potential for encapsulation failures to expose tissue to dangerous electrical currents, and face no degradation from DC biasing. Additionally, the power dissipated by ImpACTs- a previous iteration of the microresonator utilizing a field-effect transistor- was shown to be well within FDA safety margins [139].

The response of a microresonator fabricated for wireless use *in vivo* when implanted facing the cortex, utilizing it as an fMRI contrast, should be investigated. This offers a more direct and specific measure of activity within a small population of cells than traditional BOLD fMRI. The

microresonator should also be explored as a stimulation device, using precisely-controlled RF heating of the device to induce an increase in activity. Utilizing one or more microresonators to stimulate and record could allow for stronger causal inferences than can traditionally be achieved in fMRI studies [164].

Bibliography

[1] Salatino J W, Ludwig K A, Kozai T D Y and Purcell E K 2017 Glial responses to implanted electrodes in the brain *Nat Biomed Eng* **1** 862–77

[2] Shokoueinejad M, Park D-W, Jung Y, Brodnick S, Novello J, Dingle A, Swanson K, Baek D-H, Suminski A, Lake W, Ma Z and Williams J 2019 Progress in the Field of Micro-Electrocorticography *Micromachines* **10** 62

[3] Baillet S 2017 Magnetoencephalography for brain electrophysiology and imaging *Nat Neurosci* **20** 327–39

[4] Müller-Putz G R 2020 Electroencephalography *Handbook of Clinical Neurology* vol 168 (Elsevier) pp 249–62

[5] Bandettini P A 2009 What's new in neuroimaging methods? *Ann N Y Acad Sci* **1156** 260–93

[6] Logothetis N K 2008 What we can do and what we cannot do with fMRI *Nature* **453** 869–78

[7] Neely R M, Piech D K, Santacruz S R, Maharbiz M M and Carmena J M 2018 Recent advances in neural dust: towards a neural interface platform *Current Opinion in Neurobiology* **50** 64–71

[8] Seo D, Carmena J M, Rabaey J M, Maharbiz M M and Alon E 2015 Model validation of untethered, ultrasonic neural dust motes for cortical recording *Journal of Neuroscience Methods* **244** 114–22

[9] Seo D, Neely R M, Shen K, Singhal U, Alon E, Rabaey J M, Carmena J M and Maharbiz M M 2016 Wireless Recording in the Peripheral Nervous System with Ultrasonic Neural Dust *Neuron* **91** 529–39

[10] Piech D K, Johnson B C, Shen K, Ghanbari M M, Li K Y, Neely R M, Kay J E, Carmena J M, Maharbiz M M and Muller R 2020 A wireless millimetre-scale implantable neural stimulator with ultrasonically powered bidirectional communication *Nature Biomedical Engineering* **4** 207–22

[11] Hai A, Spanoudaki V Ch, Bartelle B B and Jasanoff A 2019 Wireless resonant circuits for the minimally invasive sensing of biophysical processes in magnetic resonance imaging *Nat Biomed Eng* **3** 69–78

[12] Bhatt S, Masterson E, Zhu T, Eizadi J, George J, Graupe N, Vareberg A, Phillips J, Bok I, Dwyer M, Ashtiani A and Hai A 2023 Wireless in vivo recording of cortical activity by an ion-sensitive field effect transistor *Sensors and Actuators B: Chemical* **382** 133549

[13] Octeau J C, Faas G, Mody I and Khakh B S 2018 Making, Testing, and Using Potassium Ion Selective Microelectrodes in Tissue Slices of Adult Brain *JoVE* 57511

[14] Octeau J C, Gangwani M R, Allam S L, Tran D, Huang S, Hoang-Trong T M, Golshani P, Rumbell T H, Kozloski J R and Khakh B S 2019 Transient, Consequential Increases in Extracellular Potassium Ions Accompany Channelrhodopsin2 Excitation *Cell Reports* **27** 2249-2261.e7

[15] Sibille J, Dao Duc K, Holcman D and Rouach N 2015 The Neuroglial Potassium Cycle during Neurotransmission: Role of Kir4.1 Channels ed R Jolivet *PLoS Comput Biol* **11** e1004137

[16] Ding F, O'Donnell J, Xu Q, Kang N, Goldman N and Nedergaard M 2016 Changes in the composition of brain interstitial ions control the sleep-wake cycle *Science* **352** 550–5

[17] Lebedev M A and Nicolelis M A L 2006 Brain–machine interfaces: past, present and future *Trends in Neurosciences* **29** 536–46

[18] Homer M L, Nurmikko A V, Donoghue J P and Hochberg L R 2013 Sensors and Decoding for Intracortical Brain Computer Interfaces *Annual Review of Biomedical Engineering* **15** 383–405

[19] Chandrasekaran S, Fifer M, Bickel S, Osborn L, Herrero J, Christie B, Xu J, Murphy R K J, Singh S, Glasser M F, Collinger J L, Gaunt R, Mehta A D, Schwartz A and Bouton C E 2021 Historical perspectives, challenges, and future directions of implantable brain-computer interfaces for sensorimotor applications *Bioelectron Med* **7** 14

[20] Spira M E and Hai A 2013 Multi-electrode array technologies for neuroscience and cardiology *Nature Nanotech* **8** 83–94

[21] Frank J A, Antonini M-J and Anikeeva P 2019 Next-generation interfaces for studying neural function *Nat Biotechnol* **37** 1013–23

[22] Buzsáki G, Anastassiou C A and Koch C 2012 The origin of extracellular fields and currents — EEG, ECoG, LFP and spikes *Nature Reviews Neuroscience* **13** 407–20

[23] Baillet S 2017 Magnetoencephalography for brain electrophysiology and imaging *Nat Neurosci* **20** 327–39

[24] Müller-Putz G R 2020 Chapter 18 - Electroencephalography *Handbook of Clinical Neurology* Brain-Computer Interfaces vol 168, ed N F Ramsey and J del R Millán (Elsevier) pp 249–62

[25] Boto E, Meyer S S, Shah V, Alem O, Knappe S, Kruger P, Fromhold T M, Lim M, Glover P M, Morris P G, Bowtell R, Barnes G R and Brookes M J 2017 A new generation of magnetoencephalography: Room temperature measurements using optically-pumped magnetometers *NeuroImage* **149** 404–14

[26] Roth B J and Wikswo J P 1985 The magnetic field of a single axon. A comparison of theory and experiment *Biophysical Journal* **48** 93–109

[27] Xue Y, Gao J-H and Xiong J 2006 Direct MRI detection of neuronal magnetic fields in the brain: Theoretical modeling *NeuroImage* **31** 550–9

[28] Blagoev K B, Mihaila B, Travis B J, Alexandrov L B, Bishop A R, Ranken D, Posse S, Gasparovic C, Mayer A, Aine C J, Ulbert I, Morita M, Müller W, Connor J and Halgren E 2007 Modelling the magnetic signature of neuronal tissue *NeuroImage* **37** 137–48

[29] Isakovic J, Dobbs-Dixon I, Chaudhury D and Mitrecic D 2018 Modeling of inhomogeneous electromagnetic fields in the nervous system: a novel paradigm in understanding cell interactions, disease etiology and therapy *Sci Rep* **8** 12909

[30] Vrba J and Robinson S E 2001 Signal Processing in Magnetoencephalography *Methods* **25** 249–71

[31] Bandettini P A, Petridou N and Bodurka J 2005 Direct detection of neuronal activity with MRI: Fantasy, possibility, or reality? *Appl. Magn. Reson.* **29** 65–88

[32] Petridou N, Plenz D, Silva A C, Loew M, Bodurka J and Bandettini P A 2006 Direct magnetic resonance detection of neuronal electrical activity *PNAS* **103** 16015–20

[33] Sundaram P, Nummenmaa A, Wells W, Orbach D, Orringer D, Mulkern R and Okada Y 2016 Direct neural current imaging in an intact cerebellum with magnetic resonance imaging *NeuroImage* **132** 477–90

[34] Sadleir R J, Fu F, Falgas C, Holland S, Boggess M, Grant S C and Woo E J 2017 Direct detection of neural activity in vitro using magnetic resonance electrical impedance tomography (MREIT) *Neuroimage* **161** 104–19

[35] Sajib S Z K, Chauhan M, Kwon O I and Sadleir R J 2021 Magnetic-resonance-based measurement of electromagnetic fields and conductivity in vivo using single current administration—A machine learning approach *PLOS ONE* **16** e0254690

[36] Beisteiner R, Gomiscek G, Erdler M, Teichtmeister C, Moser E and Deecke L 1995 Comparing Localization of Conventional Functional Magnetic Resonance Imaging and Magnetoencephalography *European Journal of Neuroscience* **7** 1121–4

[37] Mackert B-M, Leistner S, Sander T, Liebert A, Wabnitz H, Burghoff M, Trahms L, Macdonald R and Curio G 2008 Dynamics of cortical neurovascular coupling analyzed by simultaneous DC-magnetoencephalography and time-resolved near-infrared spectroscopy *NeuroImage* **39** 979–86

[38] Li W, Parigi G, Fragai M, Luchinat C and Meade T J 2002 Mechanistic Studies of a Calcium-Dependent MRI Contrast Agent *Inorg. Chem.* **41** 4018–24

[39] Okada S, Bartelle B B, Li N, Breton-Provencher V, Lee J J, Rodriguez E, Melican J, Sur M and Jasanoff A 2018 Calcium-dependent molecular fMRI using a magnetic nanosensor *Nature Nanotechnology* **13** 473–7

[40] Barandov A, Bartelle B B, Williamson C G, Loucks E S, Lippard S J and Jasanoff A 2019 Sensing intracellular calcium ions using a manganese-based MRI contrast agent *Nature Communications* **10** 897

[41] Lee T, Cai L X, Lelyveld V S, Hai A and Jasanoff A 2014 Molecular-Level Functional Magnetic Resonance Imaging of Dopaminergic Signaling *Science* **344** 533–5

[42] Hai A and Jasanoff A 2015 Molecular fMRI *Brain Mapping* ed A W Toga (Waltham: Academic Press) pp 123–9

[43] Hai A, Cai L X, Lee T, Lelyveld V S and Jasanoff A 2016 Molecular fMRI of Serotonin Transport *Neuron* **92** 754–65

[44] Li N and Jasanoff A 2020 Local and global consequences of reward-evoked striatal dopamine release *Nature* **580** 239–44

[45] Hai A, Dormann A, Shappir J, Yitzchaik S, Bartic C, Borghs G, Langedijk J P M and Spira M E 2009 Spine-shaped gold protrusions improve the adherence and electrical coupling of neurons with the surface of micro-electronic devices *Journal of The Royal Society Interface* **6** 1153–65

[46] Hai A, Kamber D, Malkinson G, Erez H, Mazurski N, Shappir J and Spira M E 2009 Changing gears from chemical adhesion of cells to flat substrata toward engulfment of micro-protrusions by active mechanisms *J. Neural Eng.* **6** 066009

[47] Hai A, Shappir J and Spira M E 2010 In-cell recordings by extracellular microelectrodes *Nature Methods* **7** 200–2

[48] Hai A, Shappir J and Spira M E 2010 Long-Term, Multisite, Parallel, In-Cell Recording and Stimulation by an Array of Extracellular Microelectrodes *Journal of Neurophysiology* **104** 559–68

[49] Spira M E and Hai A 2020 Multi-Electrode Array Technologies for Neuroscience and Cardiology *Nano-Enabled Medical Applications* (Jenny Stanford Publishing)

[50] Bricault S, Barandov A, Harvey P, DeTienne E, Hai A and Jasanoff A 2020 Image-guided neural activity manipulation with a paramagnetic drug *Nat Commun* **11** 136

[51] Iba S, Sekitani T, Kato Y, Someya T, Kawaguchi H, Takamiya M, Sakurai T and Takagi S 2005 Control of threshold voltage of organic field-effect transistors with double-gate structures *Applied Physics Letters* **87** 023509

[52] Anastassiou C A, Perin R, Markram H and Koch C 2011 Ephaptic coupling of cortical neurons *Nat Neurosci* **14** 217–23

[53] Hai A, Spanoudaki V C, Bartelle B B and Jasanoff A 2019 Wireless resonant circuits for the minimally invasive sensing of biophysical processes in magnetic resonance imaging *Nature Biomedical Engineering* **3** 69–78

[54] Qian W and Qian C 2019 Frequency Modulated Parametric Oscillation for Antenna Powered Wireless Transmission of Voltage Sensing Signals *IEEE Transactions on Biomedical Circuits and Systems* **13** 1783–91

[55] Jasanoff A P, Spanoudaki V and Hai A 2020 Tunable detectors

[56] Maze J R, Stanwix P L, Hodges J S, Hong S, Taylor J M, Cappellaro P, Jiang L, Dutt M V G, Togan E, Zibrov A S, Yacoby A, Walsworth R L and Lukin M D 2008 Nanoscale magnetic sensing with an individual electronic spin in diamond *Nature* **455** 644–7

[57] Arai K, Belthangady C, Zhang H, Bar-Gill N, DeVience S J, Cappellaro P, Yacoby A and Walsworth R L 2015 Fourier magnetic imaging with nanoscale resolution and compressed sensing speed-up using electronic spins in diamond *Nature Nanotechnology* **10** 859–64

[58] Barry J F, Turner M J, Schloss J M, Glenn D R, Song Y, Lukin M D, Park H and Walsworth R L 2016 Optical magnetic detection of single-neuron action potentials using quantum defects in diamond *PNAS* **113** 14133–8

[59] Davis H C, Ramesh P, Bhatnagar A, Lee-Gosselin A, Barry J F, Glenn D R, Walsworth R L and Shapiro M G 2018 Mapping the microscale origins of magnetic resonance image contrast with subcellular diamond magnetometry *Nat Commun* **9** 131

[60] Vieu C, Carcenac F, Pépin A, Chen Y, Mejias M, Lebib A, Manin-Ferlazzo L, Couraud L and Launois H 2000 Electron beam lithography: resolution limits and applications *Applied Surface Science* **164** 111–7

[61] Noga D E, Lawson R A, Lee C-T, Tolbert L M and Henderson C L 2009 Understanding pattern collapse in high-resolution lithography: impact of feature width on critical stress *Advances in Resist Materials and Processing Technology XXVI* Advances in Resist Materials and Processing Technology XXVI vol 7273 (SPIE) pp 905–12

[62] Lee H, Sun E, Ham D and Weissleder R 2008 Chip–NMR biosensor for detection and molecular analysis of cells *Nat Med* **14** 869–74

[63] Viventi J, Kim D-H, Vigeland L, Frechette E S, Blanco J A, Kim Y-S, Avrin A E, Tiruvadi V R, Hwang S-W, Vanleer A C, Wulsin D F, Davis K, Gelber C E, Palmer L, Van der Spiegel J, Wu J, Xiao J, Huang Y, Contreras D, Rogers J A and Litt B 2011 Flexible, foldable, actively multiplexed, high-density electrode array for mapping brain activity in vivo *Nat Neurosci* **14** 1599–605

[64] Park D-W, Schendel A A, Mikael S, Brodnick S K, Richner T J, Ness J P, Hayat M R, Atry F, Frye S T, Pashaie R, Thongpang S, Ma Z and Williams J C 2014 Graphene-based carbon-layered electrode array technology for neural imaging and optogenetic applications *Nature Communications* **5** 5258

[65] Bodurka J and Bandettini P A 2002 Toward direct mapping of neuronal activity: MRI detection of ultraweak, transient magnetic field changes *Magnetic Resonance in Medicine* **47** 1052–8

[66] Burghartz J N and Rejaei B 2003 On the design of RF spiral inductors on silicon *IEEE Transactions on Electron Devices* **50** 718–29

[67] Le H T, Haque R I, Ouyang Z, Lee S W, Fried S I, Zhao D, Qiu M and Han A 2021 MEMS inductor fabrication and emerging applications in power electronics and neurotechnologies *Microsyst Nanoeng* **7** 1–22

[68] Alibakhshikenari M, Ali E M, Soruri M, Dalarsson M, Naser-Moghadasi M, Virdee B S, Stefanovic C, Pietrenko-Dabrowska A, Koziel S, Szczepanski S and Limiti E 2022 A Comprehensive Survey on Antennas On-Chip Based on Metamaterial, Metasurface, and Substrate Integrated Waveguide Principles for Millimeter-Waves and Terahertz Integrated Circuits and Systems *IEEE Access* **10** 3668–92

[69] Nguyen C T-C 1998 Microelectromechanical devices for wireless communications *Proceedings MEMS 98. IEEE. Eleventh Annual International Workshop on Micro Electro Mechanical Systems. An Investigation of Micro Structures, Sensors, Actuators, Machines and Systems (Cat. No.98CH36176* Proceedings MEMS 98. IEEE. Eleventh Annual International Workshop on Micro Electro Mechanical Systems. An Investigation of Micro Structures, Sensors, Actuators, Machines and Systems (Cat. No.98CH36176 pp 1–7

[70] O K K, Kim K, Floyd B A, Mehta J L, Yoon H, Hung C-M, Bravo D, Dickson T O, Guo X, Li R, Trichy N, Caserta J, Bomstad W R, Branch J, Yang D-J, Bohorquez J, Seok E, Gao L, Sugavanam A, Lin J-J, Chen J and Brewer J E 2005 On-chip antennas in silicon ICs and their application *IEEE Transactions on Electron Devices* **52** 1312–23

[71] Senadeera P M, Dogan N S, Xie Z, Savci H S, Kateeb I and Ketel M 2013 Recent trends in RFID transponders *2013 Proceedings of IEEE Southeastcon* 2013 Proceedings of IEEE Southeastcon pp 1–5

[72] Nguyen N M and Meyer R G 1990 Si IC-compatible inductors and LC passive filters *IEEE Journal of Solid-State Circuits* **25** 1028–31

[73] Kuhn W B, Nobbe D, Kelly D and Orsborn A W 2003 Dynamic range performance of on-chip RF bandpass filters *IEEE Transactions on Circuits and Systems II: Analog and Digital Signal Processing* **50** 685–94

[74] He X, Wang R, Wu J and Li W 2020 Nature of power electronics and integration of power conversion with communication for talkative power *Nat Commun* **11** 2479

[75] Song M, Jayathurathnage P, Zanganeh E, Krasikova M, Smirnov P, Belov P, Kapitanova P, Simovski C, Tretyakov S and Krasnok A 2021 Wireless power transfer based on novel physical concepts *Nat Electron* **4** 707–16

[76] Wang Z, Liu X, Zhang G, Cao Q, Liu D, Wang M, Zhou C and Tao F 2023 Hierarchical porous structure for superior microwave absorption in biomass-derived carbon microcoils *Ceramics International* **49** 35885–97

[77] Lee C S, Lee H and Westervelt R M 2001 Microelectromagnets for the control of magnetic nanoparticles *Appl. Phys. Lett.* **79** 3308–10

[78] Lee H, Shin T-H, Cheon J and Weissleder R 2015 Recent Developments in Magnetic Diagnostic Systems *Chem Rev* **115** 10690–724

[79] Won S M, Cai L, Gutruf P and Rogers J A 2021 Wireless and battery-free technologies for neuroengineering *Nat Biomed Eng* 1–19

[80] Bok I, Vareberg A, Gokhale Y, Bhatt S, Masterson E, Phillips J, Zhu T, Ren X and Hai A 2023 Wireless agents for brain recording and stimulation modalities *Bioelectron Med* **9** 20

[81] Zhang H, Arai K, Belthangady C, Jaskula J-C and Walsworth R L 2017 Selective addressing of solid-state spins at the nanoscale via magnetic resonance frequency encoding *npj Quantum Inf* **3** 1–8

[82] Ehrmann K, Saillen N, Vincent F, Stettler M, Jordan M, Wurm F M, Besse P-A and Popovic R 2007 Microfabricated solenoids and Helmholtz coils for NMR spectroscopy of mammalian cells *Lab Chip* **7** 373–80

[83] Smistrup K, Tang P T, Hansen O and Hansen M F 2006 Microelectromagnet for magnetic manipulation in lab-on-a-chip systems *Journal of Magnetism and Magnetic Materials* **300** 418–26

[84] Lien K-Y, Lin J-L, Liu C-Y, Lei H-Y and Lee G-B 2007 Purification and enrichment of virus samples utilizing magnetic beads on a microfluidic system *Lab Chip* **7** 868–75

[85] Fulcrand R, Bancaud A, Escriba C, He Q, Charlot S, Boukabache A and Gué A-M 2011 On chip magnetic actuator for batch-mode dynamic manipulation of magnetic particles in compact lab-on-chip *Sensors and Actuators B: Chemical* **160** 1520–8

[86] Chung Y-C, Wu C-M and Lin S-H 2016 Particles Sorting in Micro Channel Using Designed Micro Electromagnets of Magnetic Field Gradient *Journal of Magnetism and Magnetic Materials* **407** 209–17

[87] Ramadan Q, Samper V, Poenar D and Yu C 2004 On-chip micro-electromagnets for magnetic-based bio-molecules separation *Journal of Magnetism and Magnetic Materials* **281** 150–72

[88] Lefebvre O, Smadja C, Martincic E, Woytasik M and Ammar M 2017 Integration of microcoils for on-chip immunosensors based on magnetic nanoparticles capture *Sensing and Bio-Sensing Research* **13** 115–21

[89] Munaz A, Shiddiky M J A and Nguyen N-T 2018 Recent advances and current challenges in magnetophoresis based micro magnetofluidics *Biomicrofluidics* **12** 031501

[90] Lee H, Liu Y, Ham D and Westervelt R M 2007 Integrated cell manipulation system--CMOS/microfluidic hybrid *Lab Chip* **7** 331–7

[91] Song S-H, Lee H-L, Min Y H and Jung H-I 2009 Electromagnetic microfluidic cell labeling device using on-chip microelectromagnet and multi-layered channels *Sensors and Actuators B: Chemical* **141** 210–6

[92] Lim B, Reddy V, Hu X, Kim K, Jadhav M, Abedini-Nassab R, Noh Y-W, Lim Y T, Yellen B B and Kim C 2014 Magnetophoretic circuits for digital control of single particles and cells *Nat Commun* **5** 3846

[93] Zhang J and Nguyen N-T 2022 Chapter 7 - Magnetic cell separation *Magnetic Materials and Technologies for Medical Applications* Woodhead Publishing Series in Electronic and Optical Materials ed A M Tishin (Woodhead Publishing) pp 193–225

[94] Nieuwoudt A, McCorquodale M S, Borno R T and Massoud Y 2005 Efficient analytical modeling techniques for rapid integrated spiral inductor prototyping *Proceedings of the IEEE 2005 Custom Integrated Circuits Conference, 2005.* Proceedings of the IEEE 2005 Custom Integrated Circuits Conference, 2005. pp 281–4

[95] Zeng J, Wang C and Sangster A J 2007 Theoretical and Experimental Studies of Flip-Chip Assembled High- Q Suspended MEMS Inductors *IEEE Transactions on Microwave Theory and Techniques* **55** 1171–81

[96] Beyzavi A and Nguyen N-T 2008 Modeling and optimization of planar microcoils *J. Micromech. Microeng.* **18** 095018

[97] Hedayati M K, Abdipour A, Sarraf Shirazi R, Ammann M J, John M, Cetintepe C and Staszewski R B 2019 Challenges in On-Chip Antenna Design and Integration With RF Receiver Front-End Circuitry in Nanoscale CMOS for 5G Communication Systems *IEEE Access* **7** 43190–204

[98] Le H T, Mizushima I, Nour Y, Tang P T, Knott A, Ouyang Z, Jensen F and Han A 2018 Fabrication of 3D air-core MEMS inductors for very-high-frequency power conversions *Microsyst Nanoeng* **4** 1–9

[99] Gansel J K, Thiel M, Rill M S, Decker M, Bade K, Saile V, von Freymann G, Linden S and Wegener M 2009 Gold helix photonic metamaterial as broadband circular polarizer *Science* **325** 1513–5

[100] Ou J-Y, Chen S-H, Lee H-M and Wu J C 2009 Fabrication and Characterization of Microscaled On-Chip Toroidal Inductors *IEEE Transactions on Magnetics* **45** 4767–9

[101] Huang W, Zhou J, Froeter P J, Walsh K, Liu S, Kraman M D, Li M, Michaels J A, Sievers D J, Gong S and Li X 2018 Three-dimensional radio-frequency transformers based on a self-rolled-up membrane platform *Nat Electron* **1** 305–13

[102] Bell D J, Sun Y, Zhang L, Dong L X, Nelson B J and Grützmacher D 2006 Three-dimensional nanosprings for electromechanical sensors *Sensors and Actuators A: Physical* **130–131** 54–61

[103] Prakash D J, Dwyer M M, Argudo M M, Debasu M L, Dibaji H, Lagally M G, van der Weide D W and Cavallo F 2021 Self-Winding Helices as Slow-Wave Structures for Sub-Millimeter Traveling-Wave Tubes *ACS Nano* **15** 1229–39

[104] Yan Z, Zhang F, Liu F, Han M, Ou D, Liu Y, Lin Q, Guo X, Fu H, Xie Z, Gao M, Huang Y, Kim J, Qiu Y, Nan K, Kim J, Gutruf P, Luo H, Zhao A, Hwang K-C, Huang Y, Zhang Y and Rogers J A 2016 Mechanical assembly of complex, 3D mesostructures from releasable multilayers of advanced materials *Sci Adv* **2** e1601014

[105] Jiang H, Wang Y, Yeh J-L A and Tien N C 2000 On-chip spiral inductors suspended over deep copper-lined cavities *IEEE Transactions on Microwave Theory and Techniques* **48** 2415–23

[106] Yoon J-B, Choi Y-S, Kim B-I, Eo Y and Yoon E 2002 CMOS-compatible surface-micromachined suspended-spiral inductors for multi-GHz silicon RF ICs *IEEE Electron Device Letters* **23** 591–3

[107] Park D S-W, Jeong Y, Lee J-B and Jung S 2008 Chip-level integration of RF MEMS on-chip inductors using UV-LIGA technique *Microsyst Technol* **14** 1429–38

[108] Kong X Y and Wang Z L 2003 Spontaneous Polarization-Induced Nanohelixes, Nanosprings, and Nanorings of Piezoelectric Nanobelts *Nano Lett.* **3** 1625–31

[109] Hokushin S, Pan L, Konishi Y, Tanaka H and Nakayama Y 2007 Field Emission Properties and Structural Changes of a Stand-Alone Carbon Nanocoil *Jpn. J. Appl. Phys.* **46** L565

[110] Zhang L, Abbott J J, Dong L, Kratochvil B E, Bell D and Nelson B J 2009 Artificial bacterial flagella: Fabrication and magnetic control *Appl. Phys. Lett.* **94** 064107

[111] Kang J, Matsumoto Y, Li X, Jiang J, Xie X, Kawamoto K, Kenmoku M, Chu J H, Liu W, Mao J, Ueno K and Banerjee K 2018 On-chip intercalated-graphene inductors for next-generation radio frequency electronics *Nat Electron* **1** 46–51

[112] Wu J, Sun Y-M, Wu Z, Li X, Wang N, Tao K and Wang G P 2019 Carbon Nanocoil-Based Fast-Response and Flexible Humidity Sensor for Multifunctional Applications *ACS Appl. Mater. Interfaces* **11** 4242–51

[113] Hwang S-W, Huang X, Seo J-H, Song J-K, Kim S, Hage-Ali S, Chung H-J, Tao H, Omenetto F G, Ma Z and Rogers J A 2013 Materials for bioresorbable radio frequency electronics *Adv Mater* **25** 3526–31

[114] Kim J, Salvatore G A, Araki H, Chiarelli A M, Xie Z, Banks A, Sheng X, Liu Y, Lee J W, Jang K-I, Heo S Y, Cho K, Luo H, Zimmerman B, Kim J, Yan L, Feng X, Xu S, Fabiani M, Gratton G, Huang Y, Paik U and Rogers J A 2016 Battery-free, stretchable optoelectronic systems for wireless optical characterization of the skin *Sci Adv* **2** e1600418

[115] Kim J, Banks A, Xie Z, Heo S Y, Gutruf P, Lee J W, Xu S, Jang K-I, Liu F, Brown G, Choi J, Kim J H, Feng X, Huang Y, Paik U and Rogers J A 2015 Miniaturized Flexible Electronic Systems with Wireless Power and Near-Field Communication Capabilities *Advanced Functional Materials* **25** 4761–7

[116] Liu Y, Pharr M and Salvatore G A 2017 Lab-on-Skin: A Review of Flexible and Stretchable Electronics for Wearable Health Monitoring *ACS Nano* **11** 9614–35

[117] Xie Z, Avila R, Huang Y and Rogers J A 2020 Flexible and Stretchable Antennas for Biointegrated Electronics *Adv Mater* **32** e1902767

[118] Bonmassar G, Lee S W, Freeman D K, Polasek M, Fried S I and Gale J T 2012 Microscopic magnetic stimulation of neural tissue *Nat Commun* **3** 921

[119] Lee S W, Fallegger F, Casse B D F and Fried S I 2016 Implantable microcoils for intracortical magnetic stimulation *Science Advances* **2** e1600889

[120] Gutruf P, Krishnamurthi V, Vázquez-Guardado A, Xie Z, Banks A, Su C-J, Xu Y, Haney C R, Waters E A, Kandela I, Krishnan S R, Ray T, Leshock J P, Huang Y, Chanda D and Rogers J A 2018 Fully implantable optoelectronic systems for battery-free, multimodal operation in neuroscience research *Nature Electronics* **1** 652–60

[121] Vázquez-Guardado A, Yang Y, Bandodkar A J and Rogers J A 2020 Recent advances in neurotechnologies with broad potential for neuroscience research *Nat Neurosci* **23** 1522–36

[122] Phillips J, Glodowski M, Gokhale Y, Dwyer M, Ashtiani A and Hai A 2022 Enhanced magnetic transduction of neuronal activity by nanofabricated inductors quantified via finite element analysis *J Neural Eng* **19**

[123] Bettinger C J 2015 Materials Advances for Next-Generation Ingestible Electronic Medical Devices *Trends in Biotechnology* **33** 575–85

[124] Steiger C, Abramson A, Nadeau P, Chandrakasan A P, Langer R and Traverso G 2019 Ingestible electronics for diagnostics and therapy *Nat Rev Mater* **4** 83–98

[125] Stojanovic G, Ljikar T and Sordan R 2006 Scaling Meander Inductors from Micro to Nano *2006 International Semiconductor Conference* 2006 International Semiconductor Conference vol 1 pp 93–6

[126] Seilis A, Moghadas H, Moez K and Daneshmand M 2015 Integrated Magnetic Nanoinductors *IEEE Transactions on Components, Packaging and Manufacturing Technology* **5** 675–84

[127] Khorasani S A 2018 Electromechanics of suspended spiral capacitors and inductors *Appl. Phys. Lett.* **112** 031906

[128] Zheng L, Zywietz U, Birr T, Duderstadt M, Overmeyer L, Roth B and Reinhardt C 2021 UV-LED projection photolithography for high-resolution functional photonic components *Microsyst Nanoeng* **7** 1–11

[129] Maksimovic J, Hu J, Ng S H, Katkus T, Seniutinas G, Rivera T P, Stuiber M, Nishijima Y, John S and Juodkazis S 2022 Beyond Lambertian light trapping for large-area silicon solar cells: fabrication methods *OEA* **5** 210086–12

[130] Lin Z, Liu K, Cao T and Hong M 2023 Microsphere femtosecond laser sub-50 nm structuring in far field via non-linear absorption *OEA* **6** 230029–10

[131] Rondin L, Tetienne J-P, Hingant T, Roch J-F, Maletinsky P and Jacques V 2014 Magnetometry with nitrogen-vacancy defects in diamond *Rep Prog Phys* **77** 056503

[132] Mohan S S, del Mar Hershenson M, Boyd S P and Lee T H 1999 Simple accurate expressions for planar spiral inductances *IEEE Journal of Solid-State Circuits* **34** 1419–24

[133] Wheeler H A 1928 Simple Inductance Formulas for Radio Coils *Proceedings of the Institute of Radio Engineers* **16** 1398–400

[134] Glenn D R, Bucher D B, Lee J, Lukin M D, Park H and Walsworth R L 2018 High-resolution magnetic resonance spectroscopy using a solid-state spin sensor *Nature* **555** 351–4

[135] Arunkumar N, Bucher D B, Turner M J, TomHon P, Glenn D, Lehmkuhl S, Lukin M D, Park H, Rosen M S, Theis T and Walsworth R L 2021 Micron-Scale NV-NMR Spectroscopy with Signal Amplification by Reversible Exchange *PRX Quantum* **2** 010305

[136] Levine E V, Turner M J, Kehayias P, Hart C A, Langellier N, Trubko R, Glenn D R, Fu R R and Walsworth R L 2019 Principles and techniques of the quantum diamond microscope *Nanophotonics* **8** 1945–73

[137] Morishita H, Kobayashi S, Fujiwara M, Kato H, Makino T, Yamasaki S and Mizuochi N 2020 Room Temperature Electrically Detected Nuclear Spin Coherence of NV Centres in Diamond *Sci Rep* **10** 792

[138] Trevathan J K, Baumgart I W, Nicolai E N, Gosink B A, Asp A J, Settell M L, Polaconda S R, Malerick K D, Brodnick S K, Zeng W, Knudsen B E, McConico A L, Sanger Z, Lee J H, Aho J M, Suminski A J, Ross E K, Lujan J L, Weber D J, Williams J C, Franke M, Ludwig K A and Shoffstall A J 2019 An Injectable Neural Stimulation Electrode Made from an In-Body Curing Polymer/Metal Composite *Advanced Healthcare Materials* **8** 1900892

[139] Hai A, Spanoudaki V C, Bartelle B B and Jasanoff A 2019 Wireless resonant circuits for the minimally invasive sensing of biophysical processes in magnetic resonance imaging *Nat Biomed Eng* **3** 69–78

[140] Seo D, Neely R M, Shen K, Singhal U, Alon E, Rabaey J M, Carmena J M and Maharbiz M M 2016 Wireless Recording in the Peripheral Nervous System with Ultrasonic Neural Dust *Neuron* **91** 529–39

[141] Szablowski J O, Lee-Gosselin A, Lue B, Malounda D and Shapiro M G 2018 Acoustically targeted chemogenetics for the non-invasive control of neural circuits *Nature Biomedical Engineering* **2** 475–84

[142] Bok I, Haber I, Qu X and Hai A 2022 In silico assessment of electrophysiological neuronal recordings mediated by magnetoelectric nanoparticles *Sci Rep* **12** 8386

[143] Caruso L, Wunderle T, Lewis C M, Valadeiro J, Trauchessec V, Trejo Rosillo J, Amaral J P, Ni J, Jendritza P, Fermon C, Cardoso S, Freitas P P, Fries P and Pannetier-Lecoeur M 2017 In Vivo Magnetic Recording of Neuronal Activity *Neuron* **95** 1283-1291.e4

[144] Boto E, Holmes N, Leggett J, Roberts G, Shah V, Meyer S S, Muñoz L D, Mullinger K J, Tierney T M, Bestmann S, Barnes G R, Bowtell R and Brookes M J 2018 Moving magnetoencephalography towards real-world applications with a wearable system *Nature* **555** 657–61

[145] Hai A 2014 In-Cell Recording and Stimulation by Engulfment Mechanisms *Nanotechnology and Neuroscience: Nano-electronic, Photonic and Mechanical Neuronal Interfacing* ed M De Vittorio, L Martiradonna and J Assad (New York, NY: Springer) pp 45–70

[146] Fong L E, Holzer J R, McBride K, Lima E A, Baudenbacher F and Radparvar M 2004 High-resolution imaging of cardiac biomagnetic fields using a low-transition-temperature superconducting quantum interference device microscope *Appl. Phys. Lett.* **84** 3190–2

[147] Weiss B P, Lima E A, Fong L E and Baudenbacher F J 2007 Paleomagnetic analysis using SQUID microscopy *Journal of Geophysical Research: Solid Earth* **112**

[148] Bok I, Ashtiani A, Gokhale Y, Phillips J, Zhu T and Hai A In Press Nanofabricated high turn-density spiral coils for on-chip electro-magneto-optical conversion *Microsystems & Nanoengineering*

[149] Huang Q-A, Dong L and Wang L-F 2016 LC Passive Wireless Sensors Toward a Wireless Sensing Platform: Status, Prospects, and Challenges *J. Microelectromech. Syst.* **25** 822–41

[150] Collins C C 1967 Miniature Passive Pressure Transensor for Implanting in the Eye *IEEE Trans. Biomed. Eng.* **BME-14** 74–83

[151] Martinez S, Pascual F and Baldrich E 2010 Inductive microcoils for the fast and simple detection of bacterial presence *Sensors and Actuators B: Chemical* **147** 304–9

[152] Wu T and Bhadra S 2022 A Printed LC Resonator-Based Flexible RFID for Remote Potassium Ion Detection *IEEE Journal on Flexible Electronics* **1** 47–57

[153] Meyer F 1994 Topographic distance and watershed lines *Signal Processing* **38** 113–25

[154] Box G E P, Jenkins G M and Rainsel G C 1994 *Time Series Analysis: Forecasting and Control* (Englewood Cliffs, NJ: Prentice Hall)

[155] Rubehn B and Stieglitz T 2010 In vitro evaluation of the long-term stability of polyimide as a material for neural implants *Biomaterials* **31** 3449–58

[156] Hassler C, von Metzen R P, Ruther P and Stieglitz T 2010 Characterization of parylene C as an encapsulation material for implanted neural prostheses *Journal of Biomedical Materials Research Part B: Applied Biomaterials* **93B** 266–74

[157] Thongpang S, Richner T J, Brodnick S K, Schendel A, Kim J, Wilson J A, Hippensteel J, Krugner-Higby L, Moran D, Ahmed A S, Neimann D, Sillay K and Williams J C 2011 A Micro-Electrocorticography Platform and Deployment Strategies for Chronic BCI Applications *Clin EEG Neurosci* **42** 259–65

[158] Buzsáki G and Kandel A 1998 Somadendritic Backpropagation of Action Potentials in Cortical Pyramidal Cells of the Awake Rat *Journal of Neurophysiology* **79** 1587–91

[159] Waters J, Schaefer A and Sakmann B 2005 Backpropagating action potentials in neurones: measurement, mechanisms and potential functions *Progress in Biophysics and Molecular Biology* **87** 145–70

[160] Buzsáki G 2004 Large-scale recording of neuronal ensembles *Nature Neuroscience* **7** 446–51

[161] Ledderose J M T, Zolnik T A, Toumazou M, Trimbuch T, Rosenmund C, Eickholt B J, Jaeger D, Larkum M E and Sachdev R N S 2023 Layer 1 of somatosensory cortex: an important site for input to a tiny cortical compartment *Cereb Cortex* **33** 11354–72

[162] Zerris V A, James K S, Roberts J B, Bell E and Heilman C B 2007 Repair of the dura mater with processed collagen devices *J Biomed Mater Res B Appl Biomater* **83** 580–8

[163] Chen P, Li F, Wang G, Ying B, Chen C, Tian Y, Chen M, Lee K J, Ying W B and Zhu J 2023 Toward Highly Matching the Dura Mater: A Polyurethane Integrating Biocompatible, Leak-Proof, and Self-Healing Properties *Macromolecular Bioscience* **23** 2300111

[164] Siddiqi S H, Kording K P, Parvizi J and Fox M D 2022 Causal mapping of human brain function *Nat Rev Neurosci* **23** 361–75

Appendix 1: Supplemental Figures

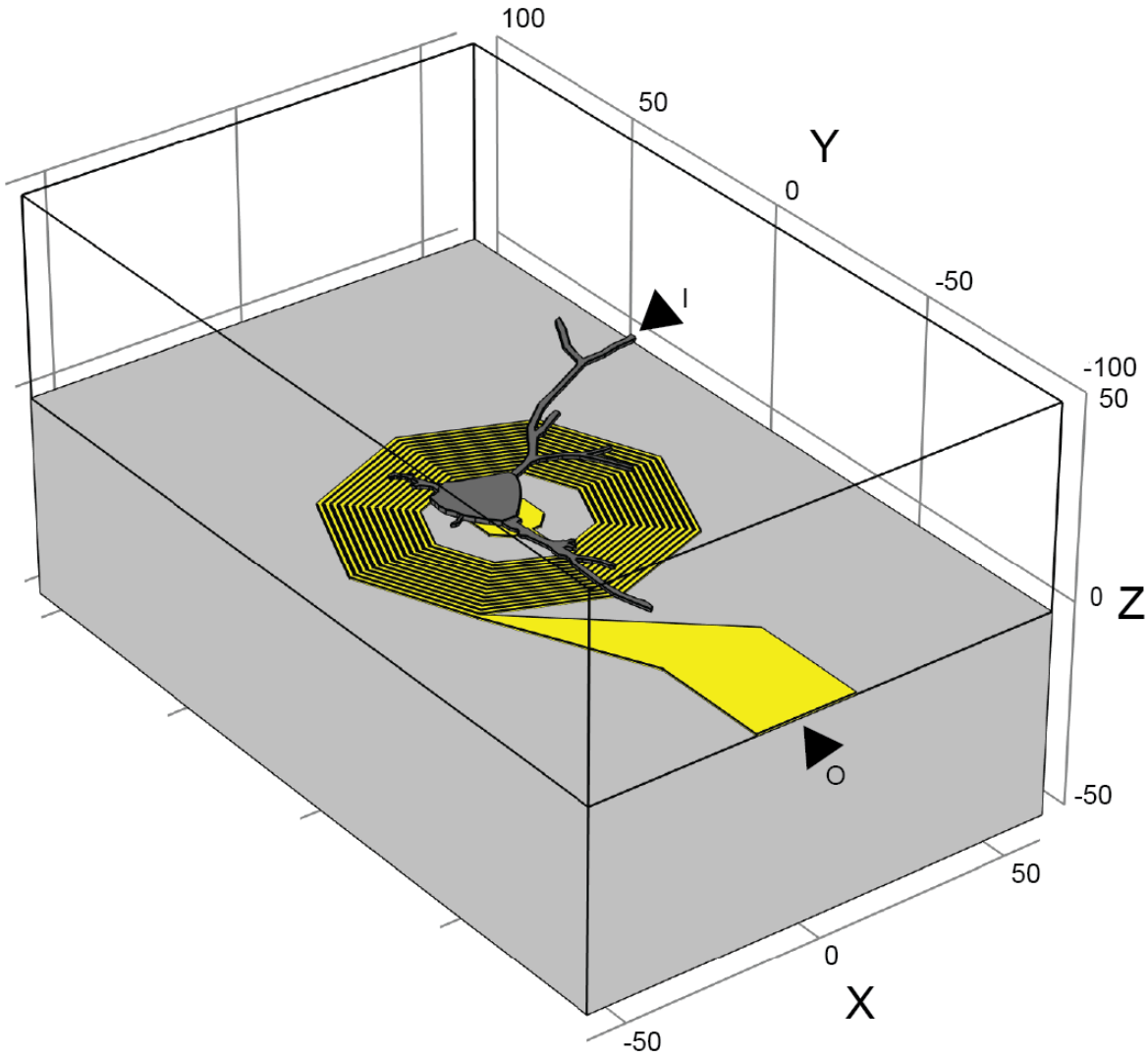

Figure S1.1: Neuron-on-nanocoil model with substrate. Grid lines marked in microns. Yellow: Nanocoil (Ti/Au). Dark grey: Neuron. Light grey: Substrate, modeled variably as silicon, glass, parylene, and polyimide in this study. Port I: current input port. Port O: ground port. Model neuron is attached to and electrically continuous with nanocoil at center pad, under cell body.

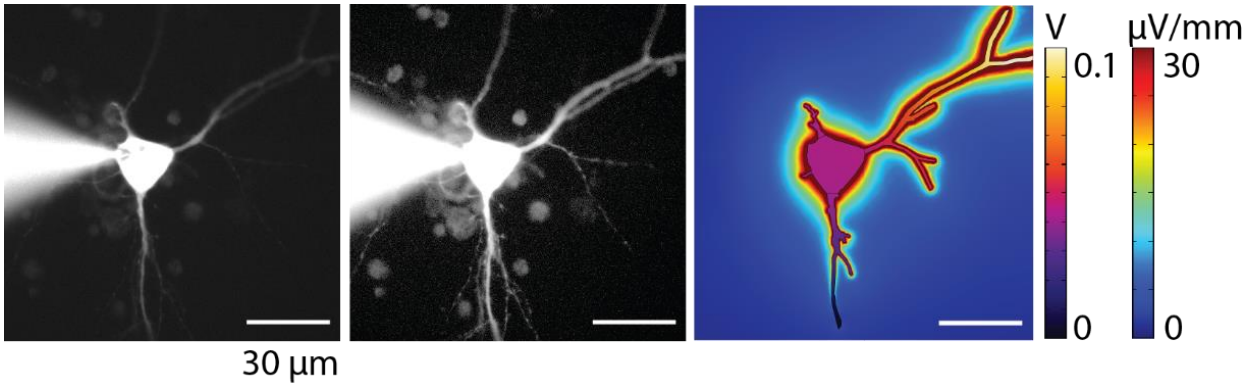

Figure S1.2: Traced Neuron. Left, image of neuron injected with fluorescently labelled biocytin with simple, linear image lookup table (LUT) enhancements. Middle, the same image with contrast enhanced to show fine processes. Right, the model of a neuron made by tracing over this image. Surface color plot, intracellular voltage. Slice plot, electrical field strength. Scale bars, 30 μm.

Appendix 2: Calcium Imaging Analysis

CalciumProcessing.m

```
% This scripts requires the following additional functions:
% blackNWhite.m (included)
% rasterAspects.m (included)
% saveOutput.m (included)
%                   plotSpikeRaster.m                   (available                   at
https://www.mathworks.com/matlabcentral/fileexchange/45671-flexible-and-fast-spike-
raster-plotting?s_tid=mwa_osa_a)

clc; clear; close all
res = 2048;

%Single input folder
pathName = 'Z:\Images\20231216_Ca-VNA\Input';
outPath = 'Z:\Personal\Jax\Calcium-VNA-Microresonators\20231216_Ca-VNA';
    if isempty(pathName)
    pathName = uigetdir(path, 'Please Select Folder');
    end

    pathStruct = dir(pathName);

    pathStruct = pathStruct(~ismember({pathStruct.name}, {'.', '..'}));

    sprintf(['Started ',datestr(now)])

    for k = 1:numel(pathStruct)

        subFolderName = fullfile(pathName,pathStruct(k).name);
        fileStruct = dir(fullfile(subFolderName,'*.tif'));
        numberOfFiles = length(fileStruct);
        ace = pathStruct(k).name;
        images = zeros(res, res, numberOfFiles, 'uint16');

            for i = 1:numberOfFiles
                  file = fileStruct(i).name;
                  fileName = fullfile(subFolderName,file);
                  images(:,:,i) = imread(fileName);
            end
        baseImage = max(images,[], 3);

        bwImage = blackNWhite(baseImage);
        [dataPLM,raster,intensity,centroids]                                    =
rasterAspects(images,numberOfFiles,bwImage,ace);
        [outputFolder]                                                          =
saveOutput(ace,baseImage,bwImage,dataPLM,raster,intensity,outPath);
        clear baseImage bwImage dataPLM raster intensity;
    end

sprintf(['Finished ',datestr(now)])
```

blackNWhite.m

```
function [bwimg] = blackNWhite(image)
gsImage = mat2gray(image);
bw     =     imbinarize(gsImage,     'adaptive',     'ForegroundPolarity',     'bright',
'Sensitivity',.5);
se_1 = strel('disk',6);
bwopen = imopen(bw, se_1);
bw4 = bwareaopen(bwopen, 100);

bwopen_big = bwareaopen(bw4, 700);
bw_small = bw4-bwopen_big;


baseSRA = imsharpen(image, 'Radius', 3, 'Amount', 7);
bwSRA    =    imbinarize(baseSRA,    'adaptive',    'ForegroundPolarity',    'bright',
'Sensitivity',.5);
bwopenSRA = imopen(bwSRA, strel('disk', 6));
bw4SRA = bwareaopen(bwopenSRA, 100);

bw_broken = and(bw4SRA, bwopen_big);
bw_merge = or(bw_broken, bw_small);

D = -bwdist(~bw_merge);

mask = imextendedmin(D,2);

D2 = imimposemin(D,mask);
Ld2 = watershed(D2);
bwimg = bw_merge;
bwimg(Ld2 == 0) = 0;
end
```

rasterAspects.m

```
function [dataPLM,raster,intensity,centroids] = rasterAspects(images,numberOfFiles,bw4,ace)
addpath('./plotSpikeRaster_v1.2/') %https://www.mathworks.com/matlabcentral/fileexchange/45671-flexible-and-fast-spike-raster-plotting?s_tid=mwa_osa_a
fs = 10;
meanIntensity = [];
s = regionprops(bw4, 'centroid');
ace = insertBefore(string(ace),'_','\');
centroids = cat(1,s.Centroid);
    for k = 1 : numberOfFiles
        re = regionprops(bw4, images(:,:,k), 'MeanIntensity'); %Add other measures of interest here
        temp = cat(1, re.MeanIntensity); % "Why cat? Concatinates each element of the struct into a new matrix(n,1)."
        %temps for measures of interest here
        meanIntensity = [meanIntensity, temp];
        %Append other things of interest here
    end

relen = length(re);
%%

locs = cell(1, relen);
ps = cell(1, relen);
    for i = 1:1:relen
        [~, ~,~,ps{i}] = findpeaks(meanIntensity(i,:));

    end
% Take largest prominance, /60, pass it as the threshold in minpeakprominecne
maxPeakVal = max(cell2mat(ps))/60;
    for i = 1:1:relen
        [~,   locs{i},~,~]   =   findpeaks(meanIntensity(i,:),   'MinPeakProminence', maxPeakVal);
    end

dataPLM = {ps,locs,meanIntensity};

fs = 10;
raster = figure('visible','off');
title(['Raster', ace])
%title([date, ' ', compounds(compound, :), ' Raster']);
plotSpikeRaster(locs, 'PlotType', 'scatter', 'TimePerBin', 1/fs);%'ColorData', ps,

%plot individual cells vs mean intensity
time = 1/fs:1/fs:numberOfFiles/fs;
cmap = 0.5 .* rand(relen,1) + 0.2;
%cmap = linspace(.8, 1, relen);
cmap = [cmap cmap cmap];

intensity = figure('visible','off');
%set(f, 'CreateFcn', 'set(gcbo,''Visible'',''on'')');
```

```
title(['Intensity vs Time', ace])%title([date, ' ', compounds(compound, :), '
Intensity']);
xlabel('Time (s)')
ylabel('Mean Intensity')

hold on
    for i = 1:1:relen
        plot(time, meanIntensity(i,:),'Color', cmap(i,:))
    end
    hold off

end
```

saveOutput.m

```
function[outputFolder]=saveOutput(ace,baseImage,bwFinal,dataPLM,raster,intensity,path
Name)
    if  isempty(pathName)
        savePath = uigetdir(pathName,'Please Select Save Destination');

    else
        savePath = pathName;
    end

    if ~exist(savePath)
        mkdir(savePath);
    end
OGPath = cd;
cd(savePath)

outputFolder = ['output_', datestr(now,'yyyymmdd')];
saveFolder = fullfile(savePath,outputFolder);

    if exist(saveFolder)== 0
        mkdir (savePath,outputFolder)
        cd (outputFolder)
    else
        cd (outputFolder)
    end


imwrite(baseImage, [ace, date, ' baseimage.tif'])
imwrite(bwFinal, [ace, date,' bw.tif'])
save([ace, date, 'data.mat'], 'dataPLM')
savefig(raster,[ace,'raster','.fig'])
savefig(intensity,[ace,'intensity','.fig'])
%PNG option
imwrite(baseImage, [ace, date, ' baseimage.png'],'png')
imwrite(bwFinal, [ace, date,' bw.png'],'png')
saveas(raster,[ace,'raster','.png'])
saveas(intensity,[ace,'intensity','.png'])
cd(OGPath)
end
```